AC electrokinetic immobilization of influenza viruses and antibodies on nanoelectrode arrays for on-chip immunoassays

DISSERTATION

zur Erlangung des akademischen Grades

“doctor rerum naturalium“

(Dr. rer. nat.)

in der Wissenschaftsdisziplin „Bioanalytik“

eingereicht an der Mathematisch-Naturwissenschaftlichen Fakultät

Institut für Biochemie und Biologie

der Universität Potsdam

angefertigt am Fraunhofer Institut IZI-BB

AG Biomolekulare Nanostrukturen und Messtechnik

Sandra Stanke

Disputation 30.11.2023

This work was conducted under the supervision of Prof. Dr. Frank F. Bier from the University of Potsdam and PD Dr. Ralph Hölzel from the Fraunhofer IZI-BB (Institute for Cell Therapy and Immunology, Bioanalytics and Bioprocesses Division) in the research group *Biomolecular Nanostructures and Measurement Technology* from the department of *Biosystem Integration and Process Automation.*

Reviewer: **Prof. Dr. Frank F. Bier**
University of Potsdam
Institute of Biochemistry and Biology
Group Molecular Bioanalytics and Bioelectronics

PD Dr. Ralph Hölzel
(A) Fraunhofer IZI-BB, Potsdam
Department of Biosystem Integration and Process Automation
Group Biomolecular Nanostructures and Measurement Technology
(B) Freie Universität Berlin
Institute of Biology

Stuart Ibsen, Ph.D.
Oregon Health and Science University, Portland, USA
School of Medicine
Department of Biomedical Engineering

Published online on the
Publication Server of the University of Potsdam:
https://doi.org/10.25932/publishup-61716
https://nbn-resolving.org/urn:nbn:de:kobv:517-opus4-617165

Abstract

In the present thesis, AC electrokinetic forces, like dielectrophoresis and AC electroosmosis, were demonstrated as a simple and fast method to functionalize the surface of nanoelectrodes with submicrometer sized biological objects. These nanoelectrodes have a cylindrical shape with a diameter of 500 nm arranged in an array of 6256 electrodes. Due to its medical relevance influenza virus as well as anti-influenza antibodies were chosen as a model organism. Common methods to bring antibodies or proteins to biosensor surfaces are complex and time-consuming. In the present work, it was demonstrated that by applying AC electric fields influenza viruses and antibodies can be immobilized onto the nanoelectrodes within seconds without any prior chemical modification of neither the surface nor the immobilized biological object. The distribution of these immobilized objects is not uniform over the entire array, it exhibits a decreasing gradient from the outer row to the inner ones. Different causes for this gradient have been discussed, such as the vortex-shaped fluid motion above the nanoelectrodes generated by, among others, electrothermal fluid flow. It was demonstrated that parts of the accumulated material are permanently immobilized to the electrodes. This is a unique characteristic of the presented system since in the literature the AC electrokinetic immobilization is almost entirely presented as a method just for temporary immobilization. The spatial distribution of the immobilized viral material or the anti-influenza antibodies at the electrodes was observed by either the combination of fluorescence microscopy and deconvolution or by super-resolution microscopy (STED). On-chip immunoassays were performed to examine the suitability of the functionalized electrodes as a potential affinity-based biosensor. Two approaches were pursued: A) the influenza virus as the bio-receptor or B) the influenza virus as the analyte. Different sources of error were eliminated by ELISA and passivation experiments. Hence, the activity of the immobilized object was inspected by incubation with the analyte. This resulted in the successful detection of anti-influenza antibodies by the immobilized viral material. On the other hand, a detection of influenza virus particles by the immobilized anti-influenza antibodies was not possible. The latter might be due to lost activity or wrong orientation of the antibodies. Thus, further examinations on the activity of by AC electric fields immobilized antibodies should follow. When combined with microfluidics and an electrical read-out system, the functionalized chips possess the potential to serve as a rapid, portable, and cost-effective point-of-care (POC) device. This device can be utilized as a basis for diverse applications in diagnosing and treating influenza, as well as various other pathogens.

Zusammenfassung

In der vorliegenden Arbeit wurden AC elektrokinetische Kräfte, wie die Dielektrophorese und die AC Elektroosmose, als einfache und schnelle Methode zur Funktionalisierung der Oberfläche von Nanoelektroden mit biologischen Objekten in Submikrometergröße demonstriert. Diese Nanoelektroden haben eine zylindrische Form mit einem Durchmesser von 500 nm und sind in einem Array aus 6256 Elektroden angeordnet. Aufgrund ihrer medizinischen Relevanz wurden Influenzaviren sowie anti-Influenza Antikörper als Modellorganismus ausgewählt. Gängige Methoden, um Antikörper oder Proteine auf Biosensoroberflächen zu bringen, sind komplex und zeitaufwändig. In der vorliegenden Arbeit wurde gezeigt, dass durch die Anwendung elektrischer Wechselfelder Influenzaviren und Antikörper innerhalb von Sekunden auf den Nanoelektroden immobilisiert werden können, ohne dass zuvor eine chemische Modifikation der Oberfläche noch des immobilisierten biologischen Objekts erforderlich ist. Die Verteilung dieser immobilisierten Objekte ist über das gesamte Array ungleichmäßig. Es kommt zur Ausbildung eines Gradienten, welcher von der äußeren zur den inneren Reihen hin abnimmt. Verschiedene Ursachen für diesen Gradienten wurden diskutiert, beispielsweise der Vortex-förmige Flüssigkeitsstrom über den Nanoelektroden, der unter anderem durch elektrothermische Flüssigkeitsbewegung erzeugt wird. Es wurde gezeigt, dass Teile des akkumulierten Materials dauerhaft an den Elektroden immobilisiert sind. Dies ist ein Alleinstellungsmerkmal des vorgestellten Systems, da in der Literatur die AC elektrokinetische Immobilisierung fast ausschließlich als Methode nur zur temporären Immobilisierung dargestellt wird. Die räumliche Verteilung des immobilisierten Virusmaterials bzw. der anti-Influenza Antikörper an den Elektroden wurde entweder durch die Kombination aus Fluoreszenzmikroskopie und Dekonvolution oder durch super-resolution Mikroskopie (STED) betrachtet. Es wurden On-Chip-Immunoassays durchgeführt, um die Eignung der funktionalisierten Elektroden für einen potenziellen affinitätsbasierten Biosensor zu untersuchen. Dabei wurden zwei Ansätze verfolgt: A) Influenzaviren als Biorezeptor oder B) Influenzavirus als Analyt. Verschiedene Fehlerquellen wurden mittels ELISA und Passivierungsexperimente eliminiert. Infolgedessen wurde die Aktivität der immobilisierten Objekte durch Inkubation mit dem Analyten überprüft. Dies führte zum erfolgreichen Nachweis von anti-Influenza Antikörpern mittels immobilisiertem Virusmaterial. Andererseits war ein Nachweis von Influenzaviruspartikeln durch die immobilisierten anti-Influenza Antikörper nicht möglich. Letzteres könnte auf einen Aktivitätsverlust oder eine falsche Ausrichtung der Antikörper zurückzuführen sein. Daher sollten weitere Untersuchungen zur Aktivität von durch elektrische Wechselfelder immobilisierte Antikörper folgen. In Kombination mit Mikrofluidik und einem elektrischen Auslesesystem besitzen die funktionalisierten Chips das Potenzial, als schnelle, tragbare und kostengünstige Point-of-Care-Einheit (POC) zu dienen. Dieses Einheit kann als Grundlage für vielfältige Anwendungen bei der Diagnose und Behandlung von Influenza und verschiedenen anderen Krankheitserregern genutzt werden.

Publications, presentations and awards

The data presented in this thesis was partially published in peer-reviewed journals and conference proceedings. Some of the results were further presented as posters or talks at national and international conferences.

Publications

- M. Prüfer, **S. Stanke**, F. F. Bier, R. Hölzel. *Catalytic activity of glucose oxidase after dielectrophoretic immobilization on nanoelectrodes*. Electrophoresis. 2023. DOI: 10.1002/elps.202300010.
- **S. Stanke**, C. Wenger, F. F. Bier, R. Hölzel. *AC electrokinetic immobilization of influenza virus*. Electrophoresis. 2022; 43:1309–1321. DOI: 10.1002/elps.202100324.

Conference presentations – posters

The italicized person has presented the poster.

- **S. Stanke**, C. Wenger, F. F. Bier, *R. Hölzel. AC field assisted deposition of influenza viruses on nanoelectrode*s. 4th European Biosensor Symposium 2023, August 27-30, Aachen.
- ***S. Stanke***, C. Wenger, F. F. Bier, R. Hölzel. *AC field assisted deposition of influenza viruses on nanoelectrodes.* DEP 2020.1 (2021), July 26 – 28, Flagstaff, Arizona, USA and online.
- *R. Hölzel*, X. Knigge, E.-M. Laux, M. Noffke, **S. Stanke**, C. Wenger, F. F. Bier. *AC electrokinetics on the nanoscale: immobilisation of nanoparticles and molecules*. 3rd European Biosensor Symposium 2021, March 09-12, online.
- ***S. Stanke***, C. Wenger, F. F. Bier, R. Hölzel. *AC field assisted deposition of influenza viruses on nanoelectrodes*. 3rd European Biosensor Symposium 2021, March 09-12, online.
- *R. Hölzel*, X. Knigge, E.-M. Laux, M. Noffke, **S. Stanke**, C. Wenger, F. F. Bier. *AC electrokinetics on the nanoscale: immobilisation of nanoparticles and molecules*. European Biosensor Symposium 2021, March 09-12, online.
- *R. Hölzel*, X. Knigge, E.-M. Laux, **S. Stanke**, C. Wenger, F. Bier. *AC electrokinetic immobilisation of nanoparticles and proteins*. 2nd European Biosensor Symposium 2019, February 18-21, Florence, Italy.
- *M. Kruse*, **S. Stanke**, C. Warmt, H. Müller-Landau, R. Hölzel, U. Rant, F.F. Bier. *Measuring multivalent interactions between Influenza A and Peptides using electronically switchable DNA nanolevers*. 2nd European Biosensor Symposium 2019, February 18-21, Florence, Italy.
- ***S. Stanke***, C. Wenger, F.F. Bier, R. Hölzl. *Biosensor surface functionalization based on AC electrokinetic forces*. DEP 2018, July 23 - 25, University of Surrey, Guildford, England.
- ***S. Stanke***, C. Wenger, F.F. Bier, R. Hölzel. *AC field assisted deposition of antibodies for virus detection*. DPG Frühjahrstagung 2018, March 11-16, Berlin, Germany.
- ***S. Stanke***, C. Wenger, F. F. Bier, R. Hölzel. *Dielectrophoretic functionalization of nanoelectrode arrays for the detection of influenza viruses*. Bioelectronics Workshop 2017, November 30th, Berlin, Germany.

- *R. Hölzel*, X. Knigge, E.-M. Laux, **S. Stanke**, C. Wenger, F.F. Bier. *AC elektrokinetic immobilization of nanoparticles and proteins*. ELKIN 2017, September 10-12, Dresden, Germany.
- ***S. Stanke***, C. Wenger, F.F. Bier, R. Hölzel. *AC electrical functionalization of nanoelectrode arrays for influenza virus detection*. ELKIN 2017, September 10-12, Dresden, Germany.
- ***S. Stanke***, C. Wenger, F.F. Bier, R. Hölzel. *Dielectrophoretic functionalization of nanoelectrode arrays for the detection of influenza viruses*. Eur Biophys J 46 (Suppl1) S337. IUPAB/EBSA 2017, July 16-20. Edinburgh, Scotland.
- ***S. Stanke***, C. Wenger, F.F. Bier, R. Hölzel. *AC electrically functionalized sensor array for influenza virus detection*. Science Day 2017, June 22nd, Leipzig, Germany.
- ***S. Stanke***, C. Wenger, F. F. Bier, R. Hölzel. *AC electrically functionalized sensor array for influenza virus detection*. 10. Deutsches BioSensor-Symposium und 1. Europäisches BioSensor-Symposium 2017, March 20-23, Potsdam, Germany.

Conference presentations – talks

The italicized person has given the talk.

- *R. Hölzel*, X. Knigge, E-M. Laux, M. Noffke, **S. Stanke**, C. Wenger, F. F. Bier. *AC electrokinetics for the immobilisation of nanoparticles and molecules*. DEP 2020.1 (2021), July 26 – 28, Flagstaff, Arizona, USA and online.
- *R. Hölzel*, X. Knigge, E.-M. Laux, M. Noffke, **S. Stanke**, F. F. Bier. Nanoelektroden-Arrays für die Oberflächen-Funktionalisierung. Meeting „Analysieren, Kultivieren, Desinfizieren – Ein Anwenderblick auf neue Polymere und Oberflächen in der Biotechnologie".2019, September 11th, Potsdam, Germany.
- *R. Hölzel*, X. Knigge, E-M. Laux, M. Noffke, **S. Stanke**, C. Wenger, F. F. Bier. *AC electrokinetic manipulation of nanoparticles and proteins*. Single-Molecule Sensors and NanoSystems International Conference (S3IC), 2019, 3rd-5th April, Munich, Germany.
- X. Knigge, E.-M. Laux, **S. Stanke**, C. Wenger, F F Bier, *R. Hölzel. Spatial manipulation of nanoparticles and molecules by AC electrokinetics*. DEP 2018, July 23 - 25, University of Surrey, Guildford, England.
- E.-M. Laux, X. Knigge, C. Wenger, **S. Stanke**, F.F. Bier, *R. Hölzel. AC electrokinetic manipulation of nanoparticles and molecules*. DPG Frühjahrstagung 2018, March 11-16, Berlin, Germany.
- *R. Hölzel*, X. Knigge, E.-M. Laux, **S. Stanke**, C. Wenger, F. F. Bier. *AC electrokinetic manipulation of nanoparticles and molecules*. Bioelectronics Workshop 2017, November 30th, Berlin, Germany.
- ***S. Stanke***. *AC electrically functionalized sensor array for influenza virus detection*. Klausurseminar 2017, November 27th, Luckenwalde, Germany.

Awards

- Doctoral scholarship by the Studienstiftung des deutschen Volkes (German Academic Scholarship Foundation) – from 03/2020 to 06/2023
- Fraunhofer *TALENTA start* – funding and development programme for female scientists; from 10/2017 to 09/2019

Table of content

Index of abbreviations

Abbreviation	Meaning
Ab	Antibody
ACEK	AC electrokinetics
ACEO	AC electroosmosis
AFM	Atomic force microscope
Ag	Antigen
AM	Arithmetic mean
BCA	Bicinchoninic acid
BG	Background
BSA	Bovine serum albumin
BPL	β-propio-lactone
CCD	Charge-coupled device
CM	Clausius-Mossotti factor
CMOS	Complementary metal-oxide-semiconductor
CMP	Chemical mechanical polishing
DEP	Dielectrophoresis
DTT	Dithiothreitol
EHT	Electron high tension; acceleration voltage
FFT	Fast Fourier transformation
FLISA	Fluorescence-linked immunosorbent assay
H3	Hemagglutinin 3
HA	Hemagglutinin
HA0	Precursor of Hemagglutinin
HA1	Hemagglutinin subunit 1
HA2	Hemagglutinin subunit 2
IDE	Interdigitated electrode
IHP	Leibniz Institute for High Performance Microelectronics
I Probe	Probe current
ITO	Indium tin oxide
LW	Landweber
M1	Matrix protein 1
M2	Matrix protein 2; ion channel
MP	Milk powder

MW	Molecular weight
N2	Neuraminidase 2
NA	Neuraminidase
NC	Negative control
nDEP	Negative dielectrophoresis
NIF	Naive inverse filtering
NP	Nucleoprotein
PA	Polymerase acidic protein
PB1	RNA-directed RNA polymerase catalytic subunit
PB2	Polymerase basic protein 2
PBS	Phosphate-buffered saline
pDEP	Positive dielectrophoresis
PEG	Polyethylenglycol
PIV	Particle image velocimetry
PSF	Point spread function
R_f	Relative migration distance
RIDT	Rapid influenza diagnostic test
RIE	Reactive ion etching
RIF	Regularized inverse filtering
RKI	Robert Koch-Institute
RL	Richardson-Lucy
ROI	Region of interest
RT	Room temperature
RT-PCR	Reverse transcription PCR
SA	Sialic acid
SAM	Self-assembled monolayer
SD	Standard deviation
SDS	Sodium dodecyl sulfate
SEM	Scanning electron microscope
STED	Stimulated emission depletion
TM	Tikhonov-Miller
TMB	Tretramethylbenzidin
TR	Tikhonov regularization
TRIS	Tris(hydroxymethyl)aminomethane
V_{rms}	Root mean square voltage
WD	Working distance
X-31	Influenza X-31

List of figures

List of tables

1 Introduction

1.1 Motivation and objectives

Respiratory viruses are a significant threat to public health, leading to a high incidence of diseases worldwide. Every year, this large group of pathogens is responsible for many deaths and economic losses. One of these viruses is the influenza virus, causing about 3 to 5 million cases of severe illness and 290,000 to 650,000 deaths each year globally [1]. Furthermore, due to the transmission by respiratory droplets and aerosols, this type of virus has the potential to spread fast and uncontrollable.

In the event of an infection with the influenza virus the incubation period is short and lasts about 2 days [2]. Specific therapy with antiviral drugs like Oseltamivir (neuraminidase inhibitor) or Amantadine (M2 inhibitor) is most effective when started as early as possible, meaning within 48 hours after the onset of the first symptoms [3]. Thus, the time frame for an in-time diagnosis and subsequent treatment is very short. Furthermore, when it comes to respiratory outbreaks in hospitals or retirement or nursing homes a fast pathogen identification is needed for patient management like isolating patients to reduce the spread of infection and for the surveillance of influenza. Thus, the Robert Koch-Institute recommends to test within 48 hours if influenza is suspected [4]. Since many other respiratory pathogens, such as rhinoviruses and coronavirus, can cause clinical symptoms that are very similar to seasonal influenza, a reliable differentiation can only be made using laboratory diagnostics. Common laboratory methods are time-consuming, complex or expensive. Thus, the viral growth in cell culture can take up to 10 days. The detection of the viral nucleic acid by PCR is faster and offers a high sensitivity and specificity but is prone to contamination, it is a complex process, expensive and requires special instruments and trained staff. Time is also required for sample collection, transport and preparation. Rapid influenza diagnostic tests do a nearly instant diagnosis, are inexpensive and portable. The majority of these tests on the market are lateral flow assays. They usually have a high specificity of above 99% but show a sensitivity of only 54% compared to RT-PCR [5]. Thus the rate of false-negative diagnosis is so high that results are inconclusive until confirmed by, e.g., PCR. Additionally, only a general detection of influenza A or B is possible, but no subtyping.

There is the need for a less complex, sensitive, less laboratory-intensive, portable and cost-effective diagnostic method for the detection of influenza. Thanks to the miniaturization in semiconductor technology, and new methods for manufacturing them, the development in biosensing and their medical applications has gained interest in recent years. The immobilization of biomolecules on the surface of a sensor is one key step in sensor development. For affinity-based biosensors these biomolecules, known as bio-receptors, transmit the interaction with the analyte to the transducer. Standard procedures for immobilizing biomolecules use chemical and physicochemical couplings, usually resulting in a statistical distribution and orientation of the immobilized molecules. This immobilization procedure can be quite complex, time-consuming and challenging involving various preparation steps such as surface cleaning, surface modification and sometimes even modifications of the bio-receptor itself. It often requires long incubation times, working with high temperatures and harsh chemicals.

The present thesis demonstrates the use of AC electrokinetic forces, like dielectrophoresis and AC electroosmosis, as a method to functionalize the surface of nanoelectrode arrays in a single step. These forces have been extensively exploited and explored for the spatial manipulation of cells. Here, these forces are now to be applied to the much less explored manipulation of submicrometer objects. This poses a greater challenge due to the smaller object size, the increasing competition with side effects such as Brownian motion and the more complex electrode structure needed. To this end, strong electric field strengths or field gradients, respectively, are necessary. The generation of these strong electric fields requires down to nanometer-sized geometries which has been fulfilled by the unique nanoelectrode arrays used in the present thesis. Because of the medical relevance mentioned, influenza viruses and anti-influenza antibodies were immobilized and their function as a bio-receptor for a potential biosensor was tested. The AC electrokinetic immobilization was carried out without prior chemical modification, neither of the electrode surface nor of the bio-receptor. Thus it is simpler and faster compared to established immobilization methods. Furthermore, due to the directed attraction to the electrodes the sample can be concentrated from small volumes demonstrating the minimal consumption of reagents this method. In by far most applications of AC electrokinetics the attraction and immobilization has been accomplished only temporary. A special feature of the system presented here is the fact that viruses as well as antibodies can be permanently immobilized. This simplifies the subsequent handling and the preparation of sensing elements for bioanalysis. It has been demonstrated before

that proteins can be orientated within the electric field [6]. This is particularly interesting for the antibody immobilization, since such a controlled orientation can be exploited to further increase the sensitivity. Finally, the presented functionalized nanoelectrodes have the prospect of a simple, inexpensive, lab-free, portable biosensor for point-of-care applications. While the focus of the present thesis was about the detection of influenza antigen or anti-influenza antibodies, the system's design is so universal that it can be transferred also to other pathogens as well as other applications outside medical diagnostics.

1.2 Model system – Influenza

The influenza virus, belonging to the family of *Orthomyxoviridae*, is an enveloped virus. Based on its genetic and antigenic differences it can be classified in the three types A, B and C. Of these, especially type A and B are of clinical relevance for humans. Its genome consists of linear negative-sense single-stranded RNA encapsulated in nucleocapsid. RNA-polymerase complexes, consisting of the proteins PB1, PB2, and PA, are located at the ends of the nucleocapsid [7]. With regard to their surface proteins hemagglutinin (HA) and neuraminidase (NA) influenza A viruses are subdivided into several subtypes or serotypes. So far, 18 different HA subtypes and 11 NA subtypes are known [8]. There are no subtypes of influenza B, but two genetically different lineages have been circulating worldwide for years: B/Yamagata and B/Victoria. HA is a homotrimer, its monomers are made of the polypeptide chains HA1 and HA2 linked together by disulfide bridges. Hemagglutinin makes up to 80% of all surface proteins with a mutual distance of about 11 nm and protrude from the membrane by about 14 nm [9, 10].

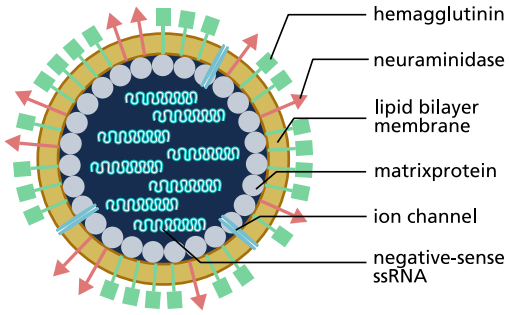

Figure 1-1 Schematic illustration of the influenza virus. It is a spherical, enveloped virus. Its genome comprises eight negative-sense, single-stranded RNA segments encapsulated in nucleoprotein. Based on the two surface proteins, hemagglutinin and neuraminidase, influenza viruses are divided into subtypes. [11]

Influenza viruses are characterized by a permanent antigenic drift. Because the RNA polymerase complex has no proofreading activity point mutations occur in the replicated viral genome with high probability. If such mutations accumulate in the genes for HA and NA this can change the amino acid sequence and thus the antigen structure, leading to an evasion of the host antibody response [12, 13]. Another, more drastic, change is the antigenic shift. If a host is getting

infected by two different influenza strains (coinfection) a reassortment of the RNA segments might occur. A novel influenza strain can emerge, that can even cause pandemics [13].

Some of the worst influenza pandemics were the Spanish flu (H1N1) in 1918/19 which led to ~50 million deaths worldwide, the Asian flu (H2N2) in 1957 killed around 1-4 million people, the Hong Kong flu (H3N2) in 1968 costed around 1-4 million human lives and the Mexican flu (H1N1) claimed up to 575,000 lives in 2009 [14, 15]. The flu season is the period when influenza viruses mainly circulate. In the northern hemisphere, this is usually between the 40th calendar and the 20th calendar week. During the flu season 2019/20 about 188,000 influenza infections and 547 number of deaths were registered in Germany [16]. Due to the Covid-19 pandemic and the associated prevention and hygiene measures, these numbers have fallen sharply. There was a worldwide absence of the flu epidemic in the 2020/21 season. So, just 564 infections and 16 deaths were registered in Germany [17]. Since April 2022 and due to lifting the COVID measures, numbers are raising again. Thus the 2021/22 season showed 21,038 infections and 39 cases of death [18], while the 2022/23 season had 292,825 registered infections and 1,028 deaths [19]. These are just the registered cases in Germany. The estimated number of unknown cases is higher. Globally, seasonal flu is estimated to cause 3 to 5 million cases of severe illness and 290,000 to 650,000 deaths each year [1].

Influenza is an airborne virus. Here, transmission occurs due to the contact between expiratory droplets and mucosa. Transmission is also possible through direct contact with contaminated surfaces and subsequent mucosal contact. [20] Sudden outbreak of symptoms like headache, cough, fever, muscle pain, sore throat and running nose can occur. There is an overlap of symptoms between the common cold, influenza (the flu) and COVID-19. Infections range from being asymptomatic, to mild symptoms, to severe courses with pulmonary complications or even multiple organ failure. The incubation period – the time between infection and the appearance of first symptoms - is short and lasts 1-4 days with a central tendency of 2 days [2]. Infected people are contagious from the day prior to symptoms up to 5-7 days after the symptoms have started. It can be longer for young children and immunocompromised people. [21]

For the treatment of influenza different classes of antiviral drugs exist. These drugs are most effective when given within 48 h of the onset of symptoms. They can lead to a reduction in viral shedding and decrease the duration of symptoms. Meta-analyses show that antiviral drugs can shorten the duration of the disease by 0.5 – 1.5 days [3]. Most antiviral drugs against influenza fall

into three categories: (I) NA inhibitor, (II) M2 inhibitor and (III) endonuclease inhibitor. (I) NA inhibitors, like Oseltamivir and Zanamivir, suppress the viral enzyme NA's active site. This causes viral aggregation at the infected host cell surface and prevents the release of viruses from the infected cell. (II) M2 inhibitors, like Amantadine, attach to the transmembrane region of the M2 protein and sterically block the channel. This hinders viral uncoating and thus viral replication. (III) Endonuclease inhibitors, like Baloxavir marboxil, inhibit the endonuclease activity of the PA subunit of influenza RNA polymerase, which is required for the transcription of the viral RNA. It is a new class of anti-influenza drugs that was first approved 2018 in Japan and 2021 in Europe. [3, 22, 23]

Influenza is a contagious, rapidly spreading disease. Its symptoms are comparable to those of other respiratory viruses and bacteria. As a result, distinguishing influenza from other infections based on the patient's symptoms is often challenging. Early detection of influenza virus infections is crucial for the fast beginning of antiviral therapy in order to reduce influenza-related morbidity and mortality. Diagnostic examinations are also important for surveillance, epidemiological studies and studies of vaccine analysis, e.g. of its effectiveness. Several methods for diagnosing influenza are currently available.

The viral detection can be performed by cell culture methods. A culture of mammalian cells is inoculated with clinical samples, propagated for up to 10 days. Virus infection and thus the existence of viral antigen can be monitored, among others, by the development of the cytopathic effect and direct or indirect immunofluorescence [24]. These cell culture methods are very time consuming and can be difficult to interpret [25]. Serological tests measure the presence of influenza-specific antibodies following infection and vaccination, like hemagglutination inhibition assay (HIA), virus neutralization assay (VN) and enzyme immunoassay (EIA).

The most common immunoassay method for influenza detection is the so called enzyme-linked immunosorbent assay (ELISA). Although faster than cell culture, it still requires a couple of hours to be performed. ELISA can be classified in different types: direct, indirect, sandwich and competitive [26]. In direct ELISA the antigen is immobilized on the surface of, for example, a microtiter plate. A labeled primary antibody binds the antigen and gets directly detected. On the other hand, in indirect ELISA the primary antibody is not labeled and is detected by a labelled secondary antibody. In sandwich ELISA the antigen is sandwiched between two specific antibodies. The capture antibody is coated on a microplate and an antigen-containing sample is

added. A conjugated-detection antibody is then added, binds to an additional epitope and enables the antigen-antibody detection. Competitive ELISA has different configurations. In one arrangement the sample antigen competes for the reporter antibody with the reference antigen, which is coated onto the microtiter plate. ELISA is applied for influenza antigen detection [27], as well as for the detection of anti-influenza antibodies for example to examine the effectiveness of a vaccination or to confirm immune response of post-viral infections [28, 29].

Rapid influenza diagnostic tests (RIDT) based on lateral flow assays are easy to handle, do not need expensive equipment or trained staff and are cost efficient. It is an immunoassay that uses monoclonal antibodies to bind the nucleoprotein of influenza A and B. If an infected sample is present, a color change will indicate this within 30 minutes. Some tests distinguish between influenza A or B viruses while others do not. Besides the advantages, there are also some disadvantages, e.g. no such test is able to distinguish between different influenza A subtypes. Results are of only qualitative nature. Despite its high specificity above 99% these RIDTs only have a sensitivity of about 54% compared to RT-PCR [5]. Thus the rate of false-negative results is high.

Nucleic acid-based tests (NATs) amplify and detect viral RNA. These tests are more sensitive as compared to antigen- or antibody-based tests, but they are expensive and time consuming. Above that specialized equipment and trained staff are required. A variety of NATs exist like: reverse transcription PCR (RT-PCR), ligase chain reaction (LCR), next-generation sequencing (NGS) and loop-mediated isothermal amplification (LAMP). [30]

1.3 Affinity-based biosensors

When it comes to affinity-based biosensors the sensing element is a bio-receptor that can be, among others, antibodies, other proteins or nucleic acid (Figure 1-2A). The bio-receptor binds the analyte from the sample to be tested and defines the selectivity and sensitivity of the sensor. The interface is an intermedium layer that connects the bio-receptor to the sensor surface. The transducer transforms the interaction between the bio-receptor and the analyte into a signal, which can be of optical, electrical, electrochemical, acoustic or calorimetric nature. [31]

The interface is a vital part in biosensor design. Its creation can be quite complex, time consuming and challenging as it involves multiple preparation steps like surface cleaning, surface modification (e.g. self-assembled monolayer, silanization, with or without protein A) and sometimes even modifications of the bio-receptor itself. Long incubation times, working with high temperatures and harsh chemicals are common.

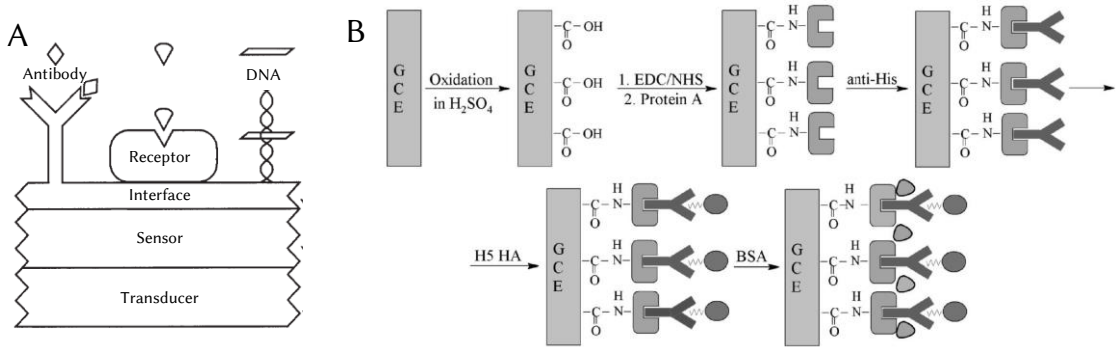

Figure 1-2 Biosensors. (A) Schematic representation of an affinity-based biosensor. Modified from [31]. (B) Preparation steps for the modification of a glassy carbon electrode for the detection of anti-H5 antibodies. At first electrodes are pre-treated with H_2SO_4 to create carboxylic groups. Protein A gets coupled by an EDC/NHS coupling reaction. Monoclonal anti-His antibodies bind to protein A and immobilize recombinant His-tagged HA which serves as the bio-receptor. Finally the modified electrodes are blocked by BSA. [32]

The following studies comprise biosensors for the detection of anti-influenza antibodies or influenza antigens. It is a selection to demonstrate the variety of different surface types, the complexity of different surface modification techniques, as well as the need of modified or non-modified bio-receptors.

In their study Horiguchi *et al.* used different sialic acid (SA) receptors immobilized on gold electrodes for the label-free detection of whole influenza H1N1 viruses [33]. As an interface a self-assembled monolayer (SAM) was used. An SAM consists of long chain molecules with a head group, typically thiol-groups, binding to the surface and a functional group protruding into the volume. Here aminooxyundecyl disulfide (AOUD) was used as SAM. Its synthesis is rather complex and took at least two days [33]. At first electrodes were cleaned, then incubated with AOUD for 24 h, and finally SA was bonded to the SAM at 60°C for 240 min. The detection of influenza was done by quartz crystal microbalance and electrically.

The interface in the study of Jarocka *et al.* is even more complex (Figure 1-2B). Here, monoclonal anti-His antibodies where bound to protein A, which itself was covalently bound by an EDC/NHS coupling to the –COOH groups of the glassy carbon electrode substrate [32]. Therefore, the glassy carbon electrodes were electrochemically pre-treated with 0.5 M H_2SO_4 to generate carboxylic groups. Subsequently, the electrodes where incubated in a mix of EDC and NHS for 1 h and protein A was covalently bound by another 1 h-incubation. Protein A was covered with anti-His antibodies by deposition for 1 h. The bio-receptor bound to that interface is a recombinant His-tagged HA to detect anti-H5 antibodies from chicken sera. Finally, the incubation with the bio-receptor and the blocking of the modified electrodes took 1 h each.

Cheng *et al.* modified the surface of aluminum interdigitated electrodes of a surface acoustic wave (SAW) chip by silanization [34]. Therefore the IDEs were washed with acetone, isopropyl alcohol and deionized water. As an interface between electrode and bio-receptor 3-aminopropyltriethoxysilane (APTES) was used. Therefore, the electrodes were incubated in APTES for 15 min and then baked for 30 min at 125 °C. While cooling down, the electrodes were immersed in glutaraldehyde and subsequently rested at room temperature for 1 h. Anti-influenza antibodies were bound to the silanized surface and the chip is getting blocked for 30 min. Finally, the interaction between anti-influenza antibodies and commercially influenza virus as well as influenza viruses from nasal swab samples are measured by the change of the interfacial capacitance [34].

1.4 Forces on suspensions in electric fields

When a non-uniform AC electric field is introduced to a suspension of polarizable particles, it causes movement of both the particles and the surrounding fluid in various directions. As a result, there are two types of forces that come into play: those that affect the particles directly, and those that affect the fluid causing the fluid to stream, which then indirectly affects the particles through the development of drag forces. The following subchapters illustrate those forces with a focus on AC electrokinetic forces (ACEK) like dielectrophoresis (DEP), AC electroosmosis (ACEO) and electrothermal fluid flow.

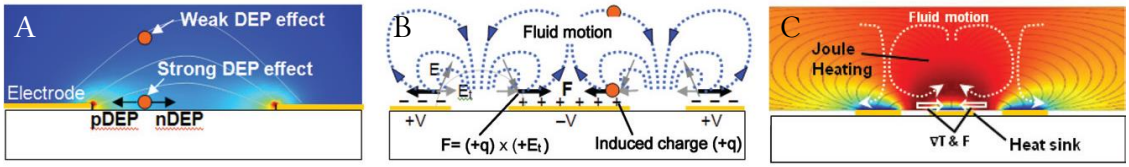

Figure 1-3 Forces on polarizable particles in non-uniform AC electric fields. (A) Dielectrophoresis (DEP). (B) AC electroosmosis (ACEO). (C) Electrothermal fluid flow. (modified from [35])

1.4.1 Forces acting on particles

When a particle is suspended in a fluid the force of gravity acts on it. This force is proportional to the strength of the gravitational field and the mass of the particle. The buoyancy force is the upward force that a fluid exerts on an object, counteracting the gravitational force. This force is proportional to the fluid density, the object's volume and the gravitational acceleration. If the particle is denser than the fluid, the gravitational force is greater than the buoyancy force, causing the particle to sink. If the particle is less dense than the fluid, the buoyancy force is greater than the gravitational force, and the particle floats to the surface. When the particle has the same density as the fluid, it remains suspended in the fluid at a constant level, neither sinking nor floating. [36, 37]

The random movement of particles suspended in a fluid is referred to as Brownian motion, which occurs due to the collisions between the fluid molecules and the particles. This phenomenon was first observed by Robert Brown in 1827 when studying the movement of pollen grains in water [38]. The motion of the particles is a consequence of the thermal energy present in the fluid, causing the particles to move in a non-directed pattern. The mathematical model for Brownian motion relates the displacement of a particle to the elapsed time and the diffusion coefficient of the particle. The degree of randomness in particle displacement is more pronounced in a less viscous liquid, for smaller particle size and at higher temperature.

Dielectrophoresis (DEP) is the motion of a polarizable particle in response to a non-uniform electric field, caused by the interaction between the electric field and the induced dipole moment of the particle. It was first described by Herbert Pohl in 1951 [39] and found its first biological application 15 years later for the separation of living and dead cells [40].

The time-averaged dielectrophoretic force on a spherical particle is given by

$$F_{DEP} = 2\pi\varepsilon_0\varepsilon_m r^3 Re[K(\omega)]\nabla|E|^2 \quad (1)$$

where ε_m is the relative permittivity of the medium, r is the radius of the particle, $Re[K(\omega)]$ is the real part of the Clausius-Mossotti (CM) factor and $|E|$ is the electric field strength. The CM factor is defined as

$$K(\omega) = \frac{\left(\varepsilon_p^* - \varepsilon_m^*\right)}{\left(\varepsilon_p^* + 2\varepsilon_m^*\right)} \quad (2)$$

where ε_p^* and ε_m^* are the complex permittivities of the particle and the medium, respectively. These in turn are defined by

$$\varepsilon_{p,m}^*(\omega) = \varepsilon_{p,m} - i\frac{\sigma_{p,m}}{\omega} \quad (3)$$

where ω is the frequency of the applied field and $\sigma_{p,m}$ is the conductivity of the particle and the medium. So, as described in equation (2) and (3) the real part of the CM factor depends on the applied frequency and the permittivity and conductivity of the particle and the medium. Depending on the values of ε_p^* and ε_m^* the CM factor can range between +1 for $\varepsilon_p^* \gg \varepsilon_m^*$ and -0.5 for $\varepsilon_p^* \ll \varepsilon_m^*$.

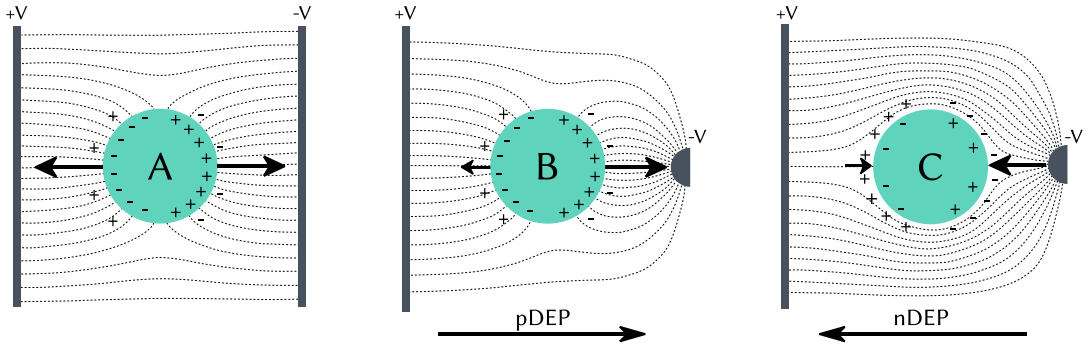

Figure 1-4 Dielectrophoresis. The figure shows a spherical, polarizable particle in a uniform (A) and a non-uniform (B and C) AC electric field. The electric field lines, represented by dashed lines, are deformed by the induced dipole. If the particle's polarizability exceeds that of the surrounding medium, the electric field lines are drawn towards the particle (A, B). Conversely, if the particle's polarizability is lower, the electric field lines are bent around the particle. In a uniform electric field, the particle experiences no net force and thus it does not move. In a non-uniform electric field the force either points in the direction of the high electric field strength (B), called pDEP or in the direction of low electric field strength (C), called nDEP. For all three cases, one-half of the AC period is depicted. Dashed lines: electric field lines; pDEP: positive dielectrophoresis; nDEP: negative dielectrophoresis. (modified from [41])

If the polarizability of the particle is greater than the polarizability of its surrounding medium, more charges accumulate at the inside of the interface between particle and medium compared to the outside. A difference in charge density occurs, causing the induced dipole to align with the electric field. Here, the electric field lines are bent touching the particle's surface in a 90° angle (Figure 1-4A and B). Conversely, if the particle has a lower polarizability than the medium, more charges accumulate on the surface of the particle, resulting in a net dipole that aligns opposite to the electric field. Here, the electric field lines are bent around the particle (Figure 1-4C). In a uniform AC electric field, the electric field strength as well as the gradient of the electric field are equal on both sides of the particle. Consequently, there is no net force and the particle does not move. On the other hand, in a non-uniform AC electric field, the electric field strength as well as the gradient of the electric field are different at both sides of the particle. This leads to three possible scenarios, depending on the electrical properties of the particle and the surrounding medium as well as the applied frequency: (I) if the particle's polarizability is higher than that of the surrounding medium, the force points towards the region with high electric field strength, causing the particle to be attracted towards this region. This is referred to as positive DEP (pDEP) with $Re[K_{(\omega)}] > 0$. (II) If the particle's polarizability is lower than that of the surrounding medium, the force points towards the region with low electric field strength, causing the particle to be repelled

from this region. This is referred to as negative DEP (nDEP) with $Re\left[K_{(\omega)}\right] < 0$. (III) Last but not least, if the particle's polarizability is equal to that of the surrounding medium, the force is zero, meaning there is no movement. This is referred to as crossover frequency with $Re\left[K_{(\omega)}\right] = 0$. All in all, the strength of the DEP force depends on multiple factors, including the particle volume, the frequency of the applied electric field, the polarizability of both the particle and the surrounding medium, and the electric field gradient. The strength of the gradient, in turn, depends on the applied voltage as well as the geometry and sharpness of the electrodes. [42–44]

1.4.2 Forces acting on the fluid

AC electroosmosis (ACEO) is a phenomenon that occurs at frequencies below 100 kHz [41, 45, 46]. When an alternating electric field is applied, the fluid experiences a resultant net motion. This motion arises from the interaction between the electric field and the electric double layer at the fluid-solid interface. The electric double layer is formed when charged particles, like ions, are present in the fluid close to the charged surface. It consists of two regions: the Stern layer and the diffuse layer. The Stern layer is in direct contact with the solid surface and comprises ions tightly bound to the surface [47]. The diffuse layer comprises mobile ions distributed within the fluid. Applying an electric field changes the charge distribution and some of the potential is getting dropped across the double layer, an effect called electrode polarization [48, 49]. The tangential component E_t of the AC electric field E exerts a force F_q on these ions in the fluid, causing them to move towards the center of the electrodes surface. During each cycle of the AC field, the potential sign alternates, which in turn swaps the distribution of the induced ions as well as the direction of the tangential electrical force. This leads to a constant the force vector direction, hence the direction of fluid flow remains constant. If the applied frequency is low the ACEO flow tends to zero. If the applied frequency is very high, the ACEO flow tends to zero as well, because the charges do not have enough time to form a double layer [50]. The authors measured and analyzed the streaming pattern in detail by particle image velocimetry (PIV) [51–53]. ACEO was used to concentrate microorganisms such as bacteria and yeast cells, as well as spores, DNA and latex beads in a controlled manner towards the center of electrode surfaces [46, 54, 55].

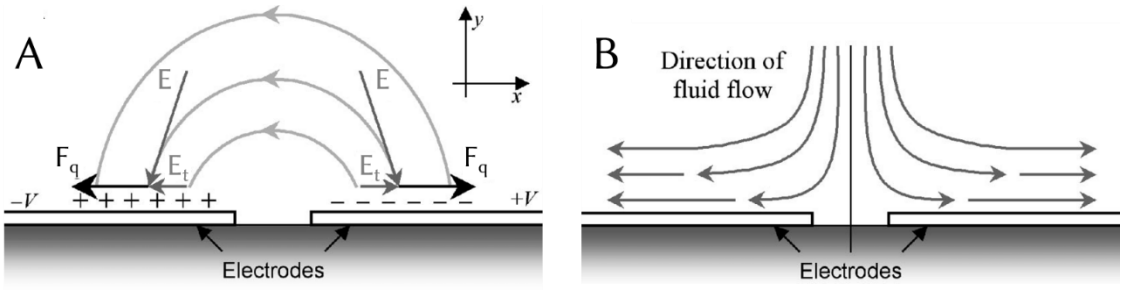

Figure 1-5 Schematic illustration of ACEO at IDEs. (A) If an AC electric field E is applied charges accumulate at the surface of the electrodes forming an electric double layer. The tangential part E_t produces a force F_q on the charges at the electrode surface. (B) Based on this force, the charges move across the electrodes creating an overall fluid stream. IDE: interdigitated electrode. (modified from [51])

Electrothermal fluid flow is caused by the interaction between an electric field and a temperature gradient in the bulk of a fluid. The gradient proceeds from the region of highest temperature at the electrodes. This temperature gradient can be caused by an external source like illumination or an internal source like Joule heating [41]. This rise in temperature was calculated to be less than 5 K even with biofluids with a conductivity of 88 mS/m, thus being safe for biological samples [56]. The electric field interacts with the resulting gradients in conductivity and permittivity giving a body force and thus a flow into the fluid. The strength of the flow depends on the temperature gradient, the conductivity of the fluid, the applied frequency of the electric field and the field strength [57]. The effect was applied, among others, for pumping [58], mixing [59] and further manipulation of bioparticles [60].

1.5 ACEK manipulation of biological objects

ACEK effects have been used to study the manipulation of polarizable biological objects for years. Cells are the most studied objects, since the dielectrophoretic force increases with the volume of the object, making manipulation more accessible. The DEP separation of live and dead cells was first demonstrated by Pohl *et al.* in 1966 [40]. Since then, a significant portion of DEP research and development has been devoted to the separation and collection of mammalian cells. One approach is to distinguish different cells from one another by their individual crossover frequencies that can be used to separate them from mixtures, recover them, or analyze how they react to various environments. ACEK manipulation has been demonstrated for a wide variety of cells, like cancer cells, blood cells and stem cells. [61–64] It has also been shown to have a commercial usage [65–68].

The progress in instrumentation and microfabrication technologies of semiconductors allowed the manufacturing of electrodes with more complex and down to nanometer-sized geometries. The creation of stronger and sharper electric fields and electric field gradients became possible and thus the manipulation of smaller objects, like viruses, proteins [69–71], DNA [72–74] and small molecules [75]. However, the amount of publications in these fields are significantly smaller compared to the amount of publications about cell-based manipulation. The spatial manipulation by ACEK of medically relevant submicrometer objects such as organelles [76–78], liposomes [79, 80] and exosomes [81, 82] is gaining popularity. When it comes to the ACEK manipulation of viruses various virus types have been investigated so far, like adenovirus [83], cowpea mosaic [84], hepatitis [85], herpes simplex [86–88], influenza [89–92], norovirus [93], rotavirus [83, 93], Sendai [94, 95], Sindbis [96] and tobacco mosaic virus [84, 87, 97, 98]. The majority of early publications were focused at the experimental validation of trapping [88, 94, 95], separation [87] and investigation of the dielectric properties of viruses [84, 86]. More recent publications - there are only a few - are focused on the application of ACEK forces on virus particles for a more medical research and usage [34, 91, 92]. However, ACEK forces have not been used to directly functionalize the surface of electrodes with viruses but rather to assist bringing the particles into spatial proximity of antibodies [34] or to concentrate the viruses before cell infection [91, 92].

When it comes to the spatial manipulation of proteins, especially antibodies, the selection of publications is even smaller. One reason is the mentioned relation between the decreasing

object-size to the increasingly demanding electrode geometry. To evade this challenge, antibodies have been attached to larger, more easy to manipulate objects, like nanobeads [99, 100] or single-walled carbon nanotubes [101, 102]. When it comes to the direct manipulation of antibodies ACEK forces were used to bring the antibodies into spatial proximity of their antigen. This results in a shorter assay time and increased sensitivity of the sensor [103, 104]. To the best of our knowledge, there are only two studies about the direct immobilization of antibodies to the surface of electrodes [105, 106]. Han *et al.* used two coplanar ITO electrodes on a glass wafer to concentrate troponin I antibodies at the electrode edge by an superimposed AC electrical signal [105]. Otto *et al.* used a nanoelectrode array of more than 10^5 cylindrical tungsten electrodes. So far, these authors are the only ones demonstrating a permanent immobilization of antibodies by ACEK that retained their functionality [106].

There are not many papers in the literature that discuss the permanent immobilization caused by ACEK particularly in the submicrometer range and its effect on the confirmation of proteins. The ability to regulate the electric field strength to accomplish permanent immobilization of bovine serum albumin (BSA) was demonstrated for the first time by Yamamoto *et al.* [107]. The only additional studies are the ones with the same or a similar electrode design as the one in the present study [71, 108–111]. There has not been much research on how ACEK affects the confirmation of proteins or the activity of, e.g., antibodies. It has been demonstrated that the electric field, especially DEP, can be used to stretch cells and DNA [73, 112]. Furthermore, some studies have investigated the influence of electric fields on the confirmation of proteins [113–117]. But so far only Otto *et al.* have investigated the activity of antibodies after ACEK immobilization [106] and Prüfer *at al.* and Laux *et al.* of enzymes [71, 108, 111]. Furthermore, Prüfer et al. have shown that the strength of activity depends on the enzyme species.

1.6 Aim of Thesis

The objective of this study is to lay the groundwork for the development of an affinity-based biosensor capable of rapidly detecting influenza viruses or anti-influenza antibodies. Due to its medical relevance, the influenza virus is chosen as a model organism. The system offers several advantages as compared to conventional detection methods. It enables the concentration of biological objects from very small volumes (3-5 µl), the detection of multiple analytes on a single chip, it allows for quick measurements, and has the potential for the integration into a point-of-care system.

A critical aspect in the biosensor design involves the functionalization of the sensor surface with a bio-receptor. Common methods for surface functionalization are complex, time-consuming, and often involve the use of harsh chemicals. In this work, the use of ACEK forces as an alternative approach for a rapid and simple surface modification without the need for prior chemical alteration of neither the sensor surface (nanoelectrodes) nor the bio-receptor (viruses or antibodies) is introduced. The potential side effects associated with ACEK manipulation are discussed, which are more significant in manipulating smaller objects such as viruses or antibodies compared to larger entities like cells.

Different potential applications of the system shall be discussed. Specifically, a focus is set to the investigation of the present system as an affinity-based biosensor using either: A) influenza virus as the bio-receptor or B) influenza virus as the analyte (Figure 1-6).

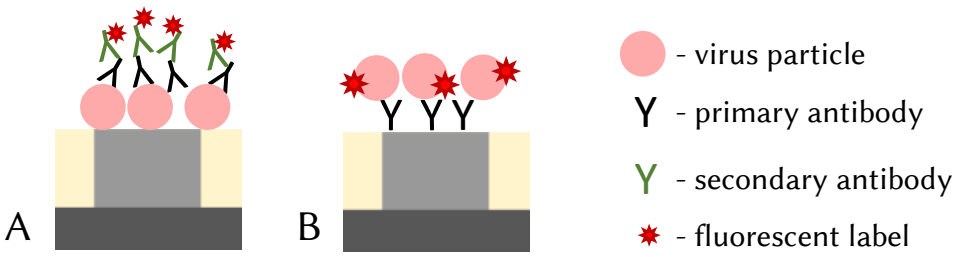

Figure 1-6 Schematic representation of the on-chip arrangement. (A) A single nanoelectrode is shown in cross-section (light grey), the surrounding SiO_2 (ochre) and an underlying metal layer (dark grey). Unstained influenza viruses (bio-receptor) are immobilized on the electrode using ACEK and then incubated with unlabeled primary antibodies (analyte). Binding is measured using a fluorescently labeled secondary antibody. (B) Antibodies (bio-receptors) are immobilized on the electrode by ACEK and then incubated with fluorescently labeled influenza viruses (analyte).

2 Materials

The following tables give an overview and detailed information about the materials used. For a better clarity, the categorization was done based on chemicals and substances, as well as devices and software. Some tables were generated specifically for components that share a thematic link, such as super-resolution microscopy.

Table 2-1 List of chemicals and substances

Chemical / Substance	Manufacturer
Bromephenole blue	Sigma-Aldrich; St. Louis, USA
BSA; Albumin Fraction V	PanReac AppliChem; Darmstadt, Germany
Conductive silver paint	Conrad electronic SE; Hirschau, Germany
Coomassie®; Quick Coomassie® Stain	Serva; Heidelberg, Germany
Dithiothreitol (DTT)	Sigma-Aldrich; St. Louis, USA
Glycerol	Sigma-Aldrich; St. Louis, USA
Glycine	Carl Roth; Karlsruhe, Germany
H_2SO_4	Sigma-Aldrich; St. Louis, USA
Influenza A, H1N1, A/Brisbane/59/2007	BeiRecources; Manassas, USA
Influenza A, H3N2, X-31, A/Aichi/1968	RKI; Berlin, Germany
Milk powder	PanReac AppliChem; Darmstadt, Germany
PBS	PanReac AppliChem; Darmstadt, Germany
PEG 600	PanReac AppliChem; Darmstadt, Germany
PEG 20.000	Carl Roth; Karlsruhe, Germany
Polyacrylamide gel; 12% Mini-PROTEAN® TGX™	Bio-Rad; Hercules, USA
Protein labeling kit; DY-634	emp Biotech GmbH; Berlin, Germany
Protein marker; peqGold protein-marker V	VWR; Radnor, USA
R18, Octadecyl rhodamine B	Biotium; Fremont, USA
Tris(hydroxymethyl)aminomethane (TRIS)	Carbochem; Philadelphia, USA
TRIS-HCl	Sigma-Aldrich; St. Louis, USA
Sodium dodecyl sulfate (SDS)	Sigma-Aldrich; St. Louis, USA

Table 2-2 Buffers and their composition

Buffer	Composition
PBS	10 mM phosphate, 2.7 mM KCl, 140 mM NaCl; sterile filtrated
TMB solution	0.1 M Na_2HPO_4 (5 parts), 0.1% H_2O_2 (4 parts), 0.1% TMB (1 part)

Table 2-3 Antibodies

Type	Description	Catalog number	Manufacturer
Primary antibody	Anti-H1, (H1N1) (A/Brisbane/59/2007); polyclonal antibody; used for: chip passivation experiment/on-chip immunoassay	MBS432100	MyBioSource, Inc.; San Diego, USA
Primary antibody	Anti-H3, (H3N2) (A/Shangdong/9/93); monoclonal; used for ELISA/FLISA/on-chip immunoassay	3HG3	HyTest Ltd.; Turku, Finland
Secondary antibody	Goat anti-mouse IgG Fc-HRP; used for ELISA	GtxMu-004-EHRPX	ImmunoReagents; Raleigh, USA
Secondary antibody	Goat anti-mouse IgG Alexa Fluor® 488; FLISA/Passivation experiments/on-chip immunoassay	115-545-146	Jackson ImmunoResearch Europe Ltd.; Cambridgeshire, UK
Secondary antibody	Goat anti-mouse IgG STAR RED	STRED-1001	Abberior GmbH; Göttingen, Germany

Table 2-4 Electrical Setup and devices

Device	Model	Manufacturer
AC voltmeter	UT803	Uni-Trend Technology; Dongguan City, China
DC voltmeter	M9803R	Mastech; Taipei, Taiwan
Demodulator probe	TT-DE 112	Testec; Dreieich, Germany
Frequency counter	Voltcraft 7202	Conrad electronic SE; Hirschau, Germany
Function generator	Model 193	Wavetek; Paris, France
Oscilloscope	HM307	Hameg; Mainhausen, Germany
Wideband amplifier	TOE 7606	TOELLNER Electronic Instrumente GmbH; Herdecke, Germany

Table 2-5 Fluorescence microscope and devices

Device	Model	Manufacturer
CCD camera	F-View II	Olympus; Tokyo, Japan
LED lamp	pE-4000	CoolLED; Andover, England
Objective 4x	UPLFLN4X, NA = 0.13	Olympus; Tokyo, Japan
Objective 10x	UPLFLN10XPH, NA = 0.30	Olympus; Tokyo, Japan
Objective 20x	UPLFLN20XPH, NA = 0.50	Olympus; Tokyo, Japan
Objective 40x	UPLFLN40XPH, NA = 0.75	Olympus; Tokyo, Japan
Objective 60x	LUCPLFLN60X, NA = 0.70	Olympus; Tokyo, Japan
Objective 100x	MPLFLN100X, NA = 0.90	Olympus; Tokyo, Japan
Objective 100x	UPLFLN100XO2PH, NA = 1.30	Olympus; Tokyo, Japan
Objective 100x	UPLSAPO100XO, NA = 1.40	Olympus; Tokyo, Japan
Fluorescence filter Cy3	F46-004; excitation: ET545/25, emission: ET605/70, beam splitter: T565lpxr	AHF; Tübingen, Germany
Fluorescence filter Cy5	F46-006; excitation: ET620/60, emission: ET700/75, beam splitter: T660lpxr	AHF; Tübingen, Germany
Fluorescence filter FITC	F46-501; excitation: ET480/36, emission: H537/42, beam splitter: H507lpxr flat	AHF; Tübingen, Germany
Fluorescence filter WIBA	U-MWIBA3; excitation: BP460-495/25, emission: 510-550, beam splitter: 505	Olympus; Tokyo, Japan
Fluorescence microscope	BX51	Olympus; Tokyo, Japan
Shutter driver	VCM-D1	Uniblitz; Rochester, USA

Table 2-6 Super-resolution microscopy

Device	Model	Manufacturer
Cover slip	High precision, 1.5H	Paul Marienfeld GmbH; Lauda Königshofen, Germany
Immersion oil	Immoil-F30cc, Type-F	Olympus; Tokyo, Japan
Microscope	IX83	Olympus; Tokyo, Japan
Objective 10x	UPLXAPO10X, NA = 0.40	Olympus; Tokyo, Japan
Objective 40x	UPLFLN40XPH, NA = 0.75	Olympus; Tokyo, Japan
Objective 100x, oil	UPLXAPO100XO, NA = 1.45	Olympus; Tokyo, Japan
STED nanoscope	STEDYCON; excitation lasers: 405 nm, 488 nm, 561 nm, 640 nm; STED-Laser: 775 nm	Abberior Instruments GmbH; Göttingen, Germany

Table 2-7 Other devices and materials

Device	Model	Manufacturer
96-well plate	655101	Greiner Bio-One GmbH; Kremsmünster, Austria
96-well plate	655077	Greiner Bio-One GmbH; Kremsmünster, Austria
96-well plate	655900	Greiner Bio-One GmbH; Kremsmünster, Austria
Centrifuge	5415D	Eppendorf; Hamburg, Germany
Centrifugal Concentrator	Vivaspin® 500; 30,000 MWCO; VS0121	Sartorius; Göttingen, Germany
Conductivity probe	TetraCon® 325	WTW; Weilheim, Germany
Conductometer	Cond 197i	WTW; Weilheim, Germany
Gel filtration	CentriPure MINI Desalt Z-50	emp Biotech GmbH; Berlin, Germany
ITO cover slip	70-100 Ω; 06462-AB	SPI Supplies; West Chester, USA
LCR meter	3532-50	HIOKI; Ueda, Japan
Microplate reader	FLUOstar® Omega	BMG LABTECH GmbH; Ortenberg, Germany
Microplate reader; excitation filter 485BP12	BMG 0643A	BMG LABTECH GmbH; Ortenberg, Germany
Microplate reader; emission filter 520BP10	BMG 0648A	BMG LABTECH GmbH; Ortenberg, Germany
pH meter	inolab pH Level 1	WTW; Weilheim, Germany
Polyacrylamide gel electrophoresis system	Mini-PROTEAN® Tetra Cell	Bio-Rad; Hercules, USA
Power supply for SDS-Page	PowerPac™ 200	Bio-Rad; Hercules, USA
Scanner	Canoscan LiDe 200	Canon; Tokyo, Japan
Scanning electron microscope	Evo MA10	Zeiss; Jena, Germany
Shaker	Thriller®	PEQLAB Biotechnologie GmbH; Erlangen, Germany
Tungsten cylinder electrodes	-	Leibniz Institute for High Performance Microelectronics (IHP); Frankfurt/Oder, Germany

Table 2-8 List of software

Software	Version / specification	Manufacturer
Cell^{M}	3.1	Olympus; Tokyo, Japan
ImageJ	version 1.51n or higher	National institute of health; Bethesda, USA
ImageJ Plugin	DeconvolutionLab	Biomedical Imaging Group, EPFL; Lausanne, Switzer
ImageJ Plugin	Diffraction PSF 3D	OptiNav Inc.; Bellevue, USA
ImageJ Plugin	MicroArrayProfile	OptiNav Inc.; Bellevue, USA
Origin Pro 2019	9.6.0.172	OriginLab Corporation; Northampton, USA
SmartSEM	5.07	Zeiss; Jena, Germany

3 Methods

3.1 X-31

The Influenza A material (A/Aichi/2/68, H3N2, short X-31) was provided by the Robert Koch-Institute (RKI). 10-13 day old fertilized chicken eggs were inoculated with virus. After an additional incubation for 2-3 days at 35 °C the allantoic fluid was harvested. The sample was ultra-centrifuged at 100.000 g at 4 °C for 1.5 h in order to concentrate and purify the virus. The pellet was dissolved in phosphate-buffered saline (PBS). Further, the viral sample was inactivated by β-propio-lactone (BPL). After the evaluation of the inactivation, the protein concentration of the X-31 sample was determined by a bicinchoninic acid (BCA) assay. Samples were stored at -80 °C and unfrozen at 4 °C.

3.2 Characterization of viral material

3.2.1 SDS-PAGE

For the running buffer 25 mM tris(hydroxymethyl)aminomethane (TRIS), 192 mM glycine and 1 % (m/v) sodium dodecyl sulfate (SDS) were dissolved in 1 L of ultrapure water. The pH of the buffer was adjusted (WTW; pH level1) to 8.3 at room temperature. To break down secondary and tertiary structures by disrupting hydrogen bonds and stretching molecules the X-31 (1.3 mg/ml) was added to the sample buffer. This buffer was freshly made out of 62.5 mM Tris-HCl, 2 % (m/v) SDS, 10 % (v/v) glycine, 0.05 % (m/v) bromephenol blue and 0.1 M dithiothreitol (DTT). The virus sample and the sample buffer were mixed at a ratio of 1:2 and incubated for 10 min at 99 °C under constant gentle shaking. For separation, 20 µl of the denatured sample was loaded onto a 12 % precast polyacrylamide gel (Bio-Rad; Mini-PROTEAN® TGX™) that had been inserted into a vertical polyacrylamide gel electrophoresis system (Bio-Rad; Mini-PROTEAN® Tetra Cell). For the sizing of protein bands 5 µl of a pre-stained protein marker (VWR; peqGold protein-marker V), ranging from 10 kDa to 250 kDa, was added to the well next to the virus sample. The power supply was attached (Bio-Rad; PowerPac™ 200) and electrophoresis was run for 1.5 h at 120 V. Subsequently, the gel was washed with ultrapure water and stained in Quick Coomassie® stain

for 2 h. Then, the gel was washed for 30 min in ultrapure water, under gentle shaking. Finally, the gel was scanned (Canon; Canoscan LiDe 200).

For molecular mass determination, the relative migration distances (R_f) of the protein standards were measured with *ImageJ* (National institute of health; version 1.51n or higher). R_f is defined as the quotient of the mobility of a protein and the distance of the buffer front. A standard curve was plotted and linearly fitted using the logarithm of the molecular weight (MW) of the protein standards and R_f. The R_f values of the X-31 protein bands were converted to MW and compared to values from literature and UniProt (chapter 4.2.1).

3.2.2 Determination of particle diameter – scanning electron microscopy

A gold-coated glass substrate covered with an electropolymer was incubated with the X-31 virus sample. Preparation of the substrate and virus incubation was carried out by the bachelor student Kira Lenz.

Subsequently, the scanning electron microscope (SEM; Zeiss; Evo MA10) was used for imaging the substrate surface and the virus particles attached to it. The SEM was controlled by the manufacture's software *SmartSEM* (Zeiss; version 5.07). An acceleration voltage (EHT) of 2 kV and a probe current (I Probe) of 5 pA were applied at a working distance (WD) between 6 mm and 6.5 mm. Scanning speed and line integration were adjusted to a certain extent to lessen the charging effects.

Image processing was performed with *ImageJ*. The frequency distribution of the diameters was calculated, plotted and a Gaussian model was fitted to the data using *OriginPro2019* (OriginLab Corporation; Origin Pro 2019 version 9.6.0.172).

3.3 Virus staining

Two distinct methods were employed to stain the influenza virus X-31: A) staining the virus proteins or B) membrane labeling. Either the proteins or the membrane were stained. No double-staining was done. To stain the virus proteins, the sample was first unfrozen and briefly vortexed. Then, it was covalently labeled with the fluorophore DY-634 (empBiotech; MK-D0107). This particular fluorophore binds to the lysine groups of the viral proteins by a reactive NHS-ester. Ultrafiltration spin columns (Sartorius; 30,000 MWCO) were used to remove the unbound dye and to exchange the buffer against ultrapure water. Here, 4-5 centrifugation cycles at 16,000 g for 5 min were carried out (Eppendorf; 5415D).

In order to label the viral membrane the lipophilic octadecyl rhodamine B (R18) was used. To ensure that later only bound R18 dye is retained, three different purification methods were tested to remove unbound R18 dye: I) ultrafiltration spin columns, (II) gel filtration and (III) centrifugation. To this end, an R18 solution (Biotium; 60033) with c = 1 µM in PBS was set up and each purification method was applied to this solution: (I) The R18 solution was filtered with an ultrafiltration spin column (Sartorius; 30,000 MWCO) for 7 min at 16,000g; (II) the R18 solution was filtered by a gel filtration column (empBiotech; CentriPure MINI) for 2 min at 1,000 g; (III) the R18 sample was centrifuged for 50 min at 16,000 g. Finally, fluorescence images of the filtrate and concentrate from (I), the filtrate from (II) and the pellet and supernatant from (III) were acquired (Cy3 filter; 40x objective, exposure time = 500 ms).

Subsequently, the viral membrane was stained by incubating X-31 with a protein concentration of 130 µg/ml with R18 at a molar concentration of 1 µM for 30 min, at RT and shaken at 800 rpm (peqLab; Thriller). The unbound dye was removed by gel filtration for 2 min at 1,000 g.

3.4 Conductivity measurements

Since a high medium conductivity promotes nDEP and has an influence on the formation of unwanted side effects like electrolysis, Joule heating and thus electrothermal fluid flow [57], it is a critical parameter in electrokinetic experiments. Thus, it is crucial to keep the conductivity low. Since the virus sample was valuable and only available in small amounts a purpose-built conductivity probe was constructed. It was made up of four platinum wires with a 0.1 mm diameter, attached to the inside of a 200 µl pipette tip. Despite the small electrode surface, this four-electrode setup allowed minimal electrode polarization. An LCR meter (HIOKI; 3532-50; 1 kHz; 1 V) was used to measure conductance in the four-terminal sensing mode. With the help of this purpose-built setup sample volumes from 20 µl down to 8 µl can be measured.

To calibrate the system, the conductivity of a KCl dilution series ranging in logarithmic steps from 2 µS/cm to 4 mS/cm was measured with a conductometer (WTW; Cond 197i) equipped with a conductivity probe (WTW; TetraCon® 325), as well as measured with the described purpose-built probe. By plotting the measured values from both conductivity probes against each other in a semi-logarithmic representation a calibration curve was determined.

Finally, the actual sample was measured with the help of the purpose-built probe. Here, the conductivity varied between 3 µS/cm and 60 µS/cm. Since the lower bound of the purpose-built probe is 3 µS/cm, the actual sample conductivity can be even less than 3 µS/cm. This is a reasonable range of conductivity, since the upper limit is at 200 µS/cm for a pDEP application with the nanoarray configuration [118]. Changes caused by contamination from the ITO or the electrode chip were not monitored, but were kept to a minimum by rinsing both with ultrapure water and drying with an N_2 stream before the experiment was done.

3.5 Electrode configuration

The electrode chips were fabricated by the Leibniz Institute for High Performance Microelectronics (IHP) using a standard 250 nm CMOS technique on 8-inch silicon wafers. Deposition of a bottom electrode made up of metal layers (Ti/TiN/AlCu/TiN/Ti) is the first step in the CMOS process. The holes for the tungsten cylinders are etched by reactive ion etching (RIE) into a layer of SiO_2 that is deposited on top of the metal layers. Then, tungsten is used to fill the holes that are in direct electrical contact with the bottom metal layer. To polish the wafer surface, chemical mechanical polishing (CMP) is used. [106, 109]

A single chips outer dimension is 1x1 cm. Four electrode arrays are located at the center (Figure 3-1A), each consisting of 6256 tungsten electrode pins arranged in an 80 by 80 matrix. Each individual electrode has a cylindrical shape with a diameter of 500 nm and a mutual spacing of 2 µm (Figure 3-1C). While the four subarrays remain electrically isolated from each other, the underlying conductive Ti/TiN/AlCu/TiN/Ti layer connects all electrodes within each array. 16 electrode-free, cross-shaped sections per array exist for improved orientation.

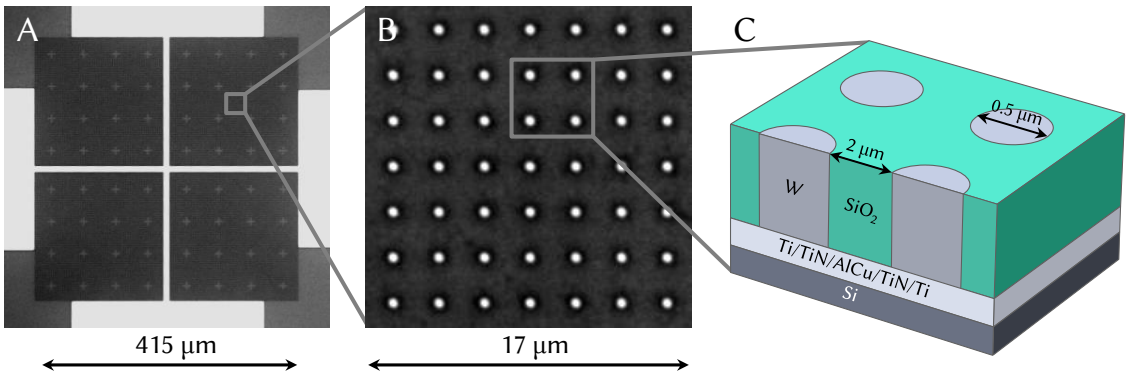

Figure 3-1 Electrode configuration. A microscopic image of the four nanoelectrode subarrays (top-view). Each array has 6256 electrodes. The four subarrays are electrically separated from each other. (B) A close-up of (A), revealing 49 electrodes. (C) Schematic cross-section of the electrode chip. The cylindrical electrodes are composed of tungsten, they have a diameter of 500 nm and a mutual distance of 2 µm. An underlying Ti/TiN/AlCu/TiN/Ti layer electrically connects the electrodes within each array. [11]

3.6 Electrode preparation

A microscope slide was used to hold the nanoelectrode chip in place (Figure 3-2). An indium tin oxide-coated cover slip (ITO; 70-100 Ω; SPI Supplies; 06462-AB) was used as a counter electrode. In order to keep the electrodes and counter electrode apart, an 80 µm thick lamination foil was used as a spacer. Therefore, a 3 mm hole was punched into the spacer, which was then hot-melted onto the electrode chip at a temperature of about 80 °C. The hole served as a sample chamber. Real-time optical microscopy observation of the experiment was made possible by the ITO's transparency. The electrical circuit between the electrodes and the ITO cover slip was closed using an additional pad covered in copper tape. Conductive silver paint (Conrad; 530042) was used to adhere copper wires to the contact pads after being soldered to the connector.

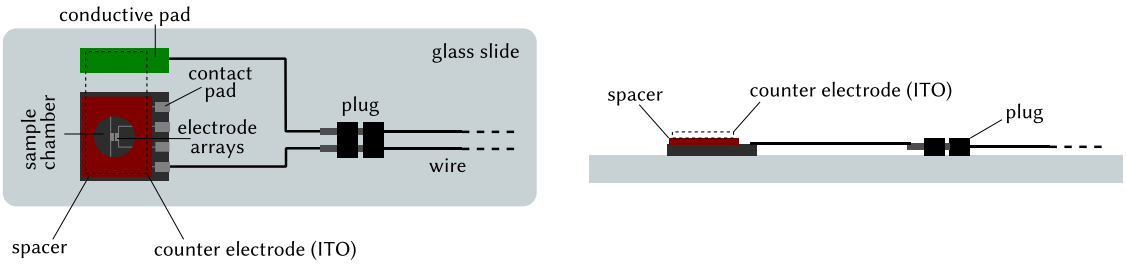

Figure 3-2 Scheme of an assembled chip. The chip was attached to the surface of a microscope slide. The counter electrode was an ITO cover slip (dashed rectangle), which was electrically connected by a pad wrapped in copper tape (green). An 80 µm thick spacer (red) separated the electrodes and the ITO cover slip. The sample chamber was formed by a 3 mm diameter hole punched into the spacer. (A) Top view, (B) side view. (modified from [11])

3.7 Electrical setup

Figure 3-3 depicts a schematic of the electrical configuration. A function generator (Wavetek; Model 193) created the AC signal, which was then amplified by a wideband amplifier. The wideband amplifier (Toellner; TOE 7606) was kept from being overdriven by the function generator's output signal by the attenuator. This made sure the voltage kept its sine shape. A separate frequency counter (Conrad; Voltcraft 7202) was used to track the frequency, and an oscilloscope (Hameg; HM307), an AC voltmeter (Uni-Trend; UT803), and a DC voltmeter

(Mastech; M9803R) with a demodulator probe (Testec; TT-DE 112) were used to measure the amplitude. The AC signal was turned on and off mechanically by a switch. Except for the two-wire cable connecting the switch and electrode chip, all devices were connected using coaxial cables. Any DC signal was blocked from getting to the electrodes by a 3.3 µF capacitor (WIMA; MKC4 SV21).

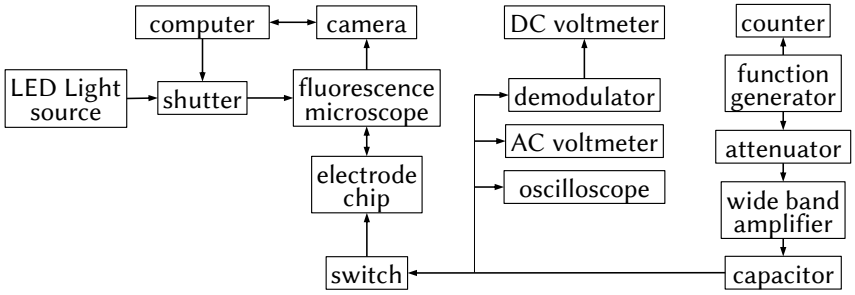

Figure 3-3 Scheme of the electrical setup. A function generator produced an AC signal, which was then amplified by a wideband amplifier. The frequency and amplitude were monitored with a frequency counter, voltmeters, and an oscilloscope. A fluorescent microscope with a CCD camera was used to capture the images. [11]

3.8 Fluorescence microscopy

An upright fluorescence microscope (Olympus; BX51) was used to monitor the fluorescently labeled samples. The experiment was observed through the transparent ITO counter electrode while the electric field was applied or through a cover slip for any other measurements. Except when working with the MPLFLN100x objective (NA =0.9), which is non-coverglass corrected. The microscope was equipped with a cooled charged-coupled device (CCD) camera (Olympus; F-View II). An LED lamp (CoolLED; pE-4000) served as the illumination source combining a 365 nm LED, a 460 nm LED, a 525 nm LED, and a 635 nm LED with an intensity setting of 5 % for bright field images and a setting of 100 % for fluorescence images combined with an LED matching the properties of the sample and the fluorescence filter. A list of the different objectives and fluorescence filters can be found in Table 2-5. The software *CellM* (Olympus; version 3.1) was used to control the shutter driver (Uniblitz; Model VCM-D1), the exposure time, the shutter and for image acquisition.

Images were processed using the software *ImageJ* extended with the plugins *MicroArray Profile* (OptiNav Inc.; USA), *Diffraction PSF 3D* (OptiNav Inc.; USA), and *DeconvolutionLab* (Biomedical Imaging Group; EPFL, Switzerland). *OriginPro2019* was used for curve fitting.

3.9 Indirect ELISA

If not stated otherwise, the antigen was diluted to a final concentration of 5 µg/ml in PBS. Subsequently, 50 µl of the antigen were added to wells of a 96-well plate (Greiner; 655101), which were then kept overnight at 4 °C in a humidity chamber. On the following day, the coating solution was removed, and the plate was washed once with tap water. To prevent non-specific binding, any remaining protein-binding sites on the coated wells were blocked using a 3% BSA solution (blocking solution) for 30 min at room temperature (RT). The plate was then incubated with 50 µl of a fresh primary antibody solution (Hytest; anti-H3), containing a concentration of 1 µg/ml in blocking solution. Incubation was done for 1 h in a humidity chamber at RT. Subsequently, the primary antibody solution was removed and the plate was washed three times with tap water. Then, 50 µl of a secondary antibody solution (ImmunoReagents; anti-mouse, HRP conjugate), diluted 1:4000 in blocking solution immediately before use, were added per well and incubated for 1 h in a humidity chamber at RT. Finally, 50 µl of a fresh TMB solution were added, incubated for 10-30 min and stopped with 50 µl of 1 M H_2SO_4. The absorption was measured at 450 nm with the reference at 630 nm using a microplate reader (BMG Labtech; FLUOstar Omega). Samples were measured in triplicates.

Table 3-1 Composition of samples and controls for ELISA. The antigen-solution was, if not stated otherwise, prepared in PBS and the antibody-solutions in blocking solution (3% BSA). If one of the components was not present, either PBS was added instead of Ag or blocking solution instead of primary Ab. PC: positive control; BG: background; NC: negative control; Ag: antigen; 1. Ab: primary antibody; 2. Ab: secondary antibody; (+) Component was present; (-) Component was not present.

	PC	Blank	BG	NC
Ag	+	-	-	+
1. Ab	+	-	+	-
2. Ab	+	+	+	+

To determine the contribution of background absorbance caused by the secondary antibody, PBS or blocking solution were added instead during both the coating step and the primary antibody incubation, to obtain the blank value. The absorbance of wells without any antigen but with primary and secondary antibody incubation in blocking solution was considered as the background. Additionally, negative control wells were incubated with the antigen and secondary antibody as described above, but the primary antibody was replaced with blocking solution. To verify the specificity of the anit-H3 antibody the wells have been coated with H1N1 instead of X-31 (H3N2).

3.10 Indirect FLISA

The fluorescence-linked immunosorbent assay (FLISA) is a method that merges fluorescent indicators with immunosorbent assay techniques. FLISA differs from conventional enzymatic reporter systems, as it employs fluorescent dye-conjugated antibodies that emit light when exposed to a specific wavelength.

At first the suitability of PBS buffer for fluorescence measurements in the microplate reader was verified. Therefore, a dilution series of the secondary antibody (Jackson ImmunoResearch; anti-mouse, Alexa 488 conjugated) from 1:200 to 1:1400 was prepared in PBS. 50 µl of each dilution were added to a well of a 96-well plate (Greiner; 655900) and its fluorescence intensity was measured by the microplate reader (excitation filter: 485BP12; emission filter: 520BP10). A well filled only with PBS was defined as the BG. Samples were measured in triplicates.

To determine a suitable concentration of the secondary antibody a 96-well plate (Greiner; 655077) was coated with 5 µg/ml of a primary antibody from mice (50 µl; in PBS) for 2 h at RT in a humidity chamber. The plate was washed with tap water and then blocked with 3% BSA for 30 min at RT. Then, the plate was washed again. The secondary antibody (anti-mouse; Alexa 488 conjugated) was prepared in a dilution series from 1:200 to 1:1400 in blocking solution. 50 µl of each dilution were added to the wells and incubated for 1 h at RT in a humidity chamber. Finally, the plate was washed, the wells were filled with 50 µl of PBS and measured by the microplate reader (excitation filter: 485BP12; emission filter: 520BP10). To determine the BG, wells were prepared as described, except that PBS was used instead of the primary antibody. All samples were measured in triplicates.

A protocol similar to the ELISA protocol outlined in chapter 3.9 was employed to confirm the antigen-antibody interaction, except for the use of a different secondary antibody (Alexa 488 conjugated) and its dilution in blocking solution at a ratio of 1:500. Instead of applying TMB and H_2SO_4, the plate was washed after the incubation with the secondary antibody and filled with 50 µl PBS per well. Subsequently, the fluorescence intensity was measured by the microplate reader (excitation filter: 485BP12; emission filter: 520BP10). The composition of the blank, BG and negative control are listed in Table 3-1.

3.11 Super-resolution microscopy - STED

To analyze the spatial distribution of immobilized antibodies super-resolution microscopy was employed, here stimulated emission depletion (STED). To prepare the chip, 5 µl of a secondary antibody solution (5 µg/ml; abberior STAR RED) was pipetted onto an electrode chip without a spacer. An electric field of 15 kHz and 5.3 V_{rms} was applied for 10 min. Then, the chip was washed and dried with N_2. 2 µl of glycerol as well as a cover slip were added. Finally, observation was done by fluorescence microscopy as well as super-resolution microscopy. For fluorescence microscopy a Cy5 filter, a 635 nm LED, a 100x objective (NA = 1.40) and an exposure-time of 2 s were chosen. The super-resolution microscope is a combination of an inverted confocal microscope (Olympus, IX83) and a STED super-resolution nanoscope (abberior, STEDYCON). The STEDYCON was equipped with four excitation lasers (405 nm, 488 nm, 561 nm, 640 nm) and a STED laser, also called depletion laser, at 775 nm. To acquire confocal images a 100x objective (NA = 1.45), a pinhole of 64 µm, a 640 nm excitation laser at 10% power, and a line accumulation of N = 1 were applied. Finally to acquire super-resolution images, the STED laser (775 nm) was set to 20% power and the line accumulation was raised to five.

3.12 On-chip experiments

3.12.1 AC electrokinetic manipulation of influenza viruses

For all non-immunoassay studies (see chapter 4.3), the surface proteins of the X-31 viral material were labeled with DY-634 as described in chapter 3.3. The labeled virus material was vortexed for 20 min and diluted to a protein concentration of about 5 µg/ml in ultrapure water. A volume of 5 µl was loaded into the sample chamber of an electrode chip and covered with an ITO cover slip. An electric field of 10-20 kHz and 3.5 V_{rms} was applied.

3.12.2 Electrode chip passivation

For the on-chip immunoassay studies the surface of the electrode chip was passivated to prevent unspecific binding, either of antibodies or the X-31 virus. To this end, different passivation solutions were tested like: 3% BSA, 2% milk powder (MP), 1% PEG 600, 1% PEG 20k and a 5 µg/ml antibody-solution.

Electrode chips were cleaned in 70% ethanol (EtOH) and dried with N_2. Then, a 5-10 µl droplet of the particular passivation solution was pipetted onto the chip and incubated for 30 min at RT in a humidity chamber. The chips were washed three times with tap water and again blow-dried with N_2. Next, 5-10 µl of a fresh 1:500 dilution of a secondary antibody (Alexa 488 conjugated) or of a R18 dyed X-31 sample (15 µg/ml), prepared in the appropriate passivation solution, was added onto the chip and incubated for 1 h at RT in a humidity chamber in the dark. Finally, the chip was washed and 5 µl of ultrapure water plus a cover slip were added and the fluorescence intensity was measured.

In order to establish the background, a chip was prepared as described, but instead of applying a passivation solution and incubating with a secondary antibody or X-31, only PBS was used. As a negative control, the chip was treated as described, but passivation was carried out using PBS, and the secondary antibody as well as the X-31 were diluted in PBS instead of a passivation solution.

3.12.3 On-chip immunoassay: Approach 1 - Influenza virus as the bio-receptor

The protocol for this on-chip immunoassay studies is based on the indirect ELISA- and FLISA-protocol as described in chapters 3.9 and 3.10. The electrode chips were cleaned by immersing them five times in a beaker filled with 70% EtOH and drying them with N_2. They were loaded with 5 µl of a non-labeled X-31 sample. The X-31 sample was diluted 1:260 with ultrapure water to reach a protein concentration of 5 µg/ml. The sample was covered with an ITO glass and an electric field of 20 kHz and 3.5 V_{rms} was applied for 10 min. After switching off the electric field, the chips were washed by immersing them five times in tap water and blowing them dry by N_2. Next, the chips were passivated by introducing 10 µl of 3% BSA (blocking solution) and incubating them with the blocking solution for 30 minutes at RT in a humidity chamber. Subsequently the chips were washed in the same manner as before. A fresh dilution of the primary antibody of 1 µg/ml in blocking solution was loaded with a volume of 10 µl onto the chips and incubated for 1 h at RT in a humidity chamber. Then, the chips were washed and dried as before. They were incubated with 10 µl of a fresh 1:500 dilution of the secondary antibody (Jackson ImmunoResearch; anti-mouse, Alexa 488 conjugated) in blocking solution for 1 h at RT in a humidity chamber in the dark. After a last washing step the chips were analyzed under the fluorescence microscope by loading a 5 µl droplet of ultrapure water and a cover slip. The WIBA filter set was used with the 490 nm LED.

A chip with just an X-31 incubation instead of being exposed to an electric field served as a negative control. For another negative control, the primary antibody was omitted. Instead, the chip was incubated with the blocking solution. Further handling was carried out as described.

In order to verify the specificity of antibodies, two more experiments were conducted. In the first experiment, H1N1 was substituted for X-31, while in the second experiment, an anti-H1 antibody was used instead of the primary antibody anti-H3.

3.12.4 On-chip immunoassay: Approach 2 - Influenza as the analyte

The electrode chips were subjected to a cleaning process which involved immersing the chips five times in a beaker containing 70% EtOH and subsequently blowing them dry using N_2. Following this, just before each experiment, 5 µl of an antibody solution (Hytest; anti-H3, 5 µg/ml) was freshly diluted in ultrapure water and loaded onto the chips. The sample was covered with an ITO cover glass and an electric field of 15 kHz was applied for 10 min. Either a voltage of 5.3, 3.5 or 1.8 V_{rms} was used. Subsequently, the chips were washed by dipping them five times into tap water and blow-drying them by N_2. The chips were passivated by incubation of 10 µl of 2% MP for 30 min at RT in a humidity chamber, followed by a washing step as described before. At last, 10 µl of a freshly labeled X-31 sample (20 µg/ml in 2% MP; R18 labeled) was loaded onto the chip and incubated for 1 h at RT in a humidity chamber in the dark. After a final washing step, the chips were measured by fluorescence microscopy using a Cy3 filter set and a 550 nm LED.

As a negative control a chip was incubated just with the antibody solution without any field application. The rest was performed as described.

In a final step, to prove the existence of immobilized non-labeled antibodies on the electrodes, the electrodes were incubated with an anti-mouse antibody (Alexa 488 conjugated). To this end, 10 µl of a fresh 1:500 dilution of the antibody was loaded onto the chip and incubated for 1 h at RT in a humidity chamber in the dark. Finally, the chips were washed, dried and their fluorescence intensity measured by a fluorescence microscope equipped with a 490 nm LED and a WIBA filter set.

3.13 Deconvolution and summation projection

After immobilization of viral material the chip was washed with ultrapure water and dried using N_2. After capturing fluorescence images a theoretical point spread function (PSF) was created using the *ImageJ* plugin *Diffraction PSF 3D* (OptiNav Inc.; USA) based on information about NA, wavelength and image pixel spacing. Based on the PSF, the *ImageJ* plugin *DeconvolutionLab* (Biomedical Imaging Group; EPFL, Switzerland) was applied using the Richardson-Lucy algorithm with a total of 100 iterations deconvolving the image.

Deconvolved images were enlarged by a factor of eight via *ImageJ* with bilinear interpolation, to better align the rectangular pixel distribution with the circular shape of the electrodes. Next, a grid was created, defining the position of 119 electrodes (7x17), using the *MicroArray Profile* (OptiNav Inc.; USA) plugin. A self-written *ImageJ* macro was used to read and convert the coordinates of each individual electrode into rectangular ROIs of equal size (see Appendix A). These ROIs were then utilized to extract each electrode as individual images, and the pixels at the same position in all 119 images were subsequently added up to create a summation projection. The individual steps are shown schematically in Figure 3-4A-F.

To visualize the spatial distribution of the fluorescence intensity 31 circular ROIs were concentrically aligned on top of the summation projection. The external radii ranged from 2 px (21.5 nm) to 62 px (666.5 nm) with each ring having a width of 2 px. The BG was defined as the mean fluorescence intensity of the area surrounding the outermost ring. Furthermore, the summation projection of 70 empty electrodes from the array center was created. Finally, the mean fluorescence intensity for each ring was determined, the BG was subtracted, as was the mean fluorescence intensity for each ring of the empty electrodes. The fluorescence values were normalized and plotted against the spatial distance (Figure 3-4G).

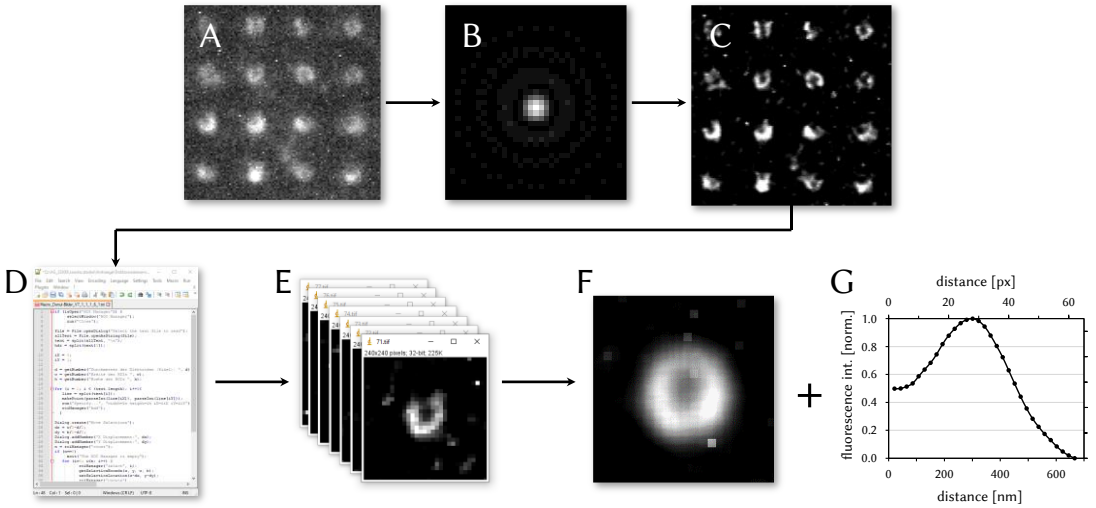

Figure 3-4 Experimental procedure and data analysis for the determination of the spatial distribution of viral material. (A) The original fluorescence image was captured. (B) Definition of the point spread function (PSF). (C) Based on the PSF the image from (A) was deconvolved. With the help of a self-written *ImageJ* macro (D) each individual electrode was cut out (E) from the deconvolved image. Finally, these images were combined into a summation projection (F) and the spatial dependency of the fluorescence signal was plotted (G).

4 Results and Discussion

In the following sections the results of the experimental studies are presented and discussed. At first the viral sample is introduced in more detail and characterized (section 4.1 and 4.2). In the following section 4.3, the main section, the AC electrokinetic immobilization of influenza viruses on nanoelectrode arrays is observed. Here, the focus is set to the temporal development, the permanent immobilization that is unusual for pDEP and the spatial distribution of viral material on the electrodes. This section was published by Stanke *et al.* [11]. Finally, first experimental studies for an on-chip immunoassay are presented in chapter 4.4. Here a differentiation was made between X-31 being the bio-receptor or being the analyte.

4.1 The virus strain X-31

The X-31 strain is a reassortant between A/aichi/1968 (H3N2) and A/PuertoRico/8/1934 (H1N1). Crossing these two virus strains results in a strain with H3 and N2 as surface proteins on the one hand and an increased growth capacity coming from A/PuertoRico/8/1934 leading to a high-yield virus strain in chicken egg production on the other hand. The yield is 8-fold higher compared to the parental virus. [119, 120]

The virus samples were inactivated with BPL by the RKI. BPL invades X-31 and interacts with nucleic acids. Here, due to its electrophilic nature BPL alkylates the viral RNA [121]. Thus, the spherical structure of the virus particles remains intact [122]. Another advantage of BPL is that it does not require a neutralizing agent to stop its reaction since it completely hydrolyzes into non-toxic compounds [123]. However, the influence of BPL on the viral infectivity is still subject of research [124, 125].

4.2 Characterization of the viral material

4.2.1 SDS-PAGE

Figure 4-1B shows a section of the stained and washed polyacrylamide gel. The contrast was adjusted via *ImageJ*. The top lane shows the pre-stained protein marker, the bottom lane the separated proteins from the X-31 sample. The marker lane was used to create a standard curve with a logarithmic fit with a coefficient of determination (R^2) of 0.99 (Figure 4-1A).

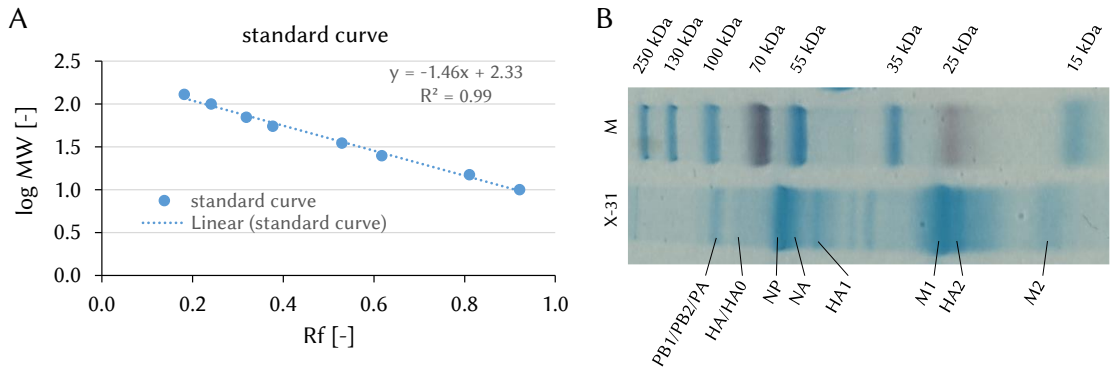

Figure 4-1 Analysis of protein composition via SDS-PAGE. (A) Standard curve for molecular weight determination. The relative migration distances of the protein standards were measured. Dividing the mobility of a protein by the distance of the buffer front gives R_f. The standard curve was plotted with a linear fit (dotted line). (B) SDS-PAGE separation of proteins from the X-31 sample. Proteins were separated on a 14 % polyacrylamide gel. M: pre-stained protein marker.

Characteristic proteins were identified by comparing values calculated from SDS-PAGE with values from UniProt and literature, as shown in Table 4-1. While there is a good agreement between the calculated values and values from the literature, there is a partially large deviation from the UniProt values. UniProt uses merely the molecular weight of the amino acid chain, while values from SDS-PAGE and Literature also include posttranslational modifications.

Table 4-1 Comparison of the measured molecular weight of X-31 proteins to values from literature and UniProt. MW: molecular weight.

Protein	UniProt MW [kDa]	Literature MW [kDa]	SDS-Page MW [kDa]
PB1/PB2/PA	83-87 [126–128]	88-94 [129]	91
HA0/HA	64 [130]	75-84 [129, 131–134]	81
NP	56 [135]	62 [129]	64
NA	43 [136]	56-57 [129, 131]	61
HA1	36 [130]	51-58 [129, 131, 133, 134, 137]	54
M1	28 [138]	27-28 [129, 131, 139]	28
HA2	26 [130]	25-30 [129, 131, 133, 134, 137]	26
M2	11 [140]	15-17 [131, 141, 142]	16

4.2.2 Determination of particle diameter

For the SEM images a low EHT of 2 kV and I_{probe} of 5 pA were applied for two reasons: (I) to minimize the penetration depth of the electron beam and thus to enable to scan the surface. (II) The sample was not gold-coated, as is common in SEM measurements of biological samples. This allows for the examination of unaltered virus particles. There is also the fact, that the virus sample is an insulator and does not efficiently transports incident electrons. To achieve a balance between incoming electrons and emerging secondary electrons, a low EHT and I Probe are required. As a result, charging effects are diminished, but resolution suffers somewhat though.

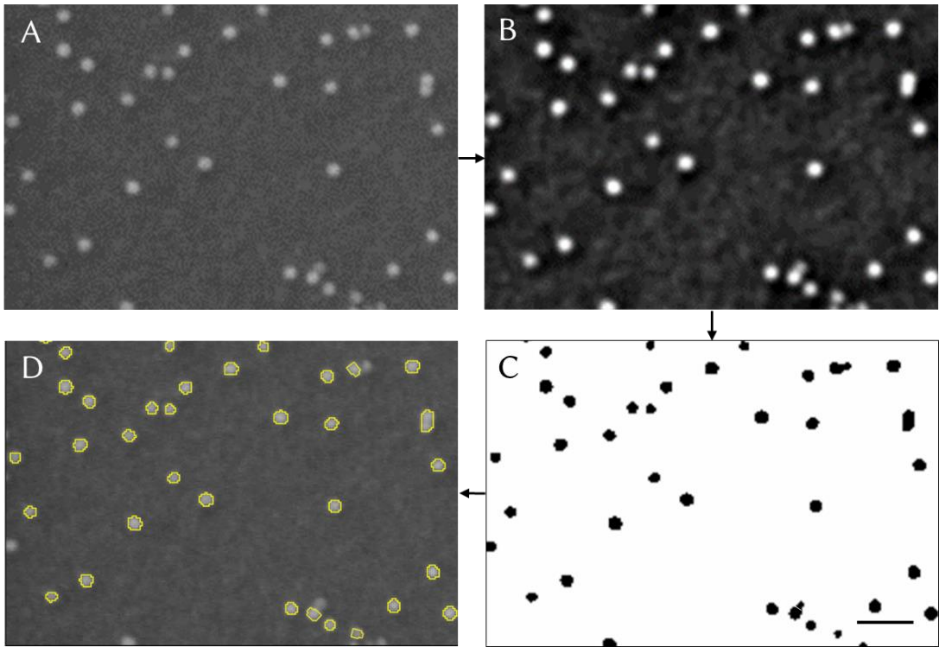

Figure 4-2 Determination of virus diameter. (A) Original SEM image. EHT = 2 kV, I Probe = 5 pA, WD = 6.5 mm. (B) The SEM images were processed by FFT to be smoothed. (C) Images were transferred into binary images where pixels smaller than a certain value are defined as the BG and pixels above that values are defined as virus particles. (D) Since each virus particle is defined as a ROI, its area can be read out and converted into the particles diameter. Scale bar: 500 nm.

Image processing was performed with *ImageJ* (Figure 4-2B-C). At first, the spatial scale of the original SEM images was defined. With the help of a fast Fourier transformation (FFT) the images were filtered for specific minimum and maximum feature sizes to smoothen the images. A threshold was defined to generate binary images where pixels smaller then this threshold were

considered to be the background (BG) and pixels greater than this value were considered to be virus particles. The surface area of each particle was calculated after they were classified as regions of interest (ROI). The area of each particle was converted into the diameter.

For the determination of the particle diameter a total number of 573 virus particles were analyzed from SEM images. The frequency distribution and the Gaussian fit of these diameters are displayed as a histogram in Figure 4-3 with an interval width of 10 nm extending from 60 nm up to 170 nm. About 90 % of all virus particles are in the range of 80 nm to 130 nm. The arithmetic mean (AM) is at $\overline{X}_{arithm.}$ = 113.6 nm with a standard deviation (SD) of σ = 14.3 nm, which is consistent with the literature where the outer diameter of spherical X-31 particles range from 84 nm to 170 nm with a mean at 120 nm [9, 143].

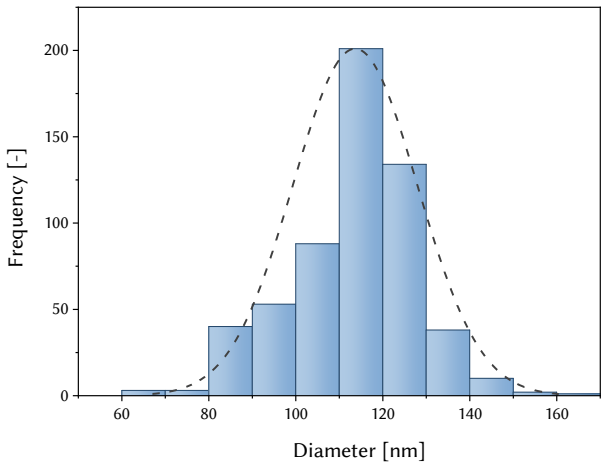

Figure 4-3 Frequency distribution of the X-31 particle diameter. 573 virus particles were analyzed having a size distribution from 60 nm to 170 nm. About 90 % of all particles are in the size range from 80 nm to 130 nm. The arithmetic mean is at 113.6 nm. Dashed line: Gaussian fit.

4.3 AC electrokinetic immobilization of influenza virus material

In the following subchapters, the study of the temporal development of the AC electrokinetic immobilization of influenza viruses is presented. A detailed explanation of the experimental parameters and image processing methods is provided. The change in fluorescence intensity of the outer seven rows is measured, analyzed and discussed, highlighting the inhomogeneous distribution pattern and its side effects. The immobilized virus material is subjected to different forces after switching off the electric field, demonstrating that some parts of the material are temporarily accumulated to the electrodes, while others are permanently accumulated. Lastly, the spatial distribution of the immobilized viral material is analyzed at the single-electrode-level by combining fluorescence microscopy and deconvolution.

4.3.1 Temporal development of the dielectrophoretic immobilization

4.3.1.1 Determination of the experimental parameters

The applied voltage (I) and frequency (II) are the two main electrical factors that can be varied for ACEK-experiments. (I) Using high voltages can have negative effects such as electrolysis, joule heating, and fluid streaming, which can work against the intended dielectrophoretic force [41, 52, 57, 106]. Therefore, to minimize these side effects and achieve a rapid but gentle immobilization a voltage of 3.5 V_{rms} was selected. (I) Based on previous research [75, 108–111] a range between 10 and 20 kHz was determined to be appropriate for immobilizing submicrometer objects like nanospheres and enzymes. In order to increase the effectiveness of immobilization, the frequency applied was analyzed in a systematic manner for this frequency range. Frequencies below 5 kHz were found to cause bubble formation due to electrolysis [52, 57, 111]. While the viral material initially gathered unevenly at the electrodes at 10 and 15 kHz, a more uniform distribution was achieved at 20 kHz. As a result, all subsequent experiments were conducted at 20 kHz.

An upright fluorescence microscope was used to monitor the dielectric immobilization of the X-31 virus material on the non-transparent nanoelectrode chip. The images were captured using a 60x objective and a Cy5 filter, with an exposure time of 500 ms. The images were taken at 20 s intervals over a total time span of 180 s. The only time point at which no AC-electric field was applied was at t=0 s. The shutter was closed between image captures to minimize bleaching effects.

The experiment manager of *CellM* was used to time the opening of the shutter, illumination, image acquisition, and closing of the shutter.

It was observed that no viral material accumulated on the electrodes of a non-activated array (negative control), which demonstrates that the viral material was not trapped by adsorption to the activated electrodes.

4.3.1.2 Definition of ROI size

For image evaluation, five different ROIs were studied, including three circular ROIs and two ring-shaped ones. The circular ROIs had diameters ranging from 4 px (C4, d = 590 nm), to 8 px (C8, d = 1.18 µm) and finally 16 px (C16, d = 2.36 µm). With pixel sizes of 147.5 nm x 147.5 nm, the circular ROIs were covering areas from the size of the electrode to almost halfway to the neighboring electrodes. The ring-shaped ROIs had an outer diameter of 8 px (R8) and 16 px (R16) and an inner diameter of 4 and 8 px, respectively. These ROIs did not cover the surface of the electrodes but formed a ring around the electrodes. All ROI sizes were aligned concentrically as shown in Figure 4-4A. As a reference point, a rectangular ROI surrounding 7×12 electrodes at the corner of an unused electrode array was defined to determine the background fluorescence. This BG signal was determined for each time point. Mean and integrated intensity values of 30 electrodes from the outermost row (row 1) were plotted for all ROI sizes (Figure 4-4). The results revealed an exponential correlation between the amount of immobilized viral material and the investigated timespan with R^2 from 0.98 to 0.99:

$$y = y_0 + A_1 e^{\frac{-t}{t_1}} \tag{4}$$

The graphs exhibit a strictly monotonic increase, while the function approaches the limit value y_0 asymptotically as $t \longrightarrow \infty$, signifying that $y = y_0$ functions as an infinity asymptote. The point of intersections between the tangent of the curve at $t_0 = 0$ and the asymptote y_0 is t_1. At t_1, the function's value is about 63 % of the final value y_0, or $y(t_1) = 0.63 y_0$. As t_1 becomes smaller, the mean fluorescence intensity for the corresponding ROI increases faster and stronger.

The concentric alignment of all ROIs with the electrodes results in C4 closely surrounding the nanoelectrode surface. AC electrokinetic forces are known to be strongest at the edge and surface of the electrodes, resulting in direct attraction of the viral material to the nanoelectrodes. Hence,

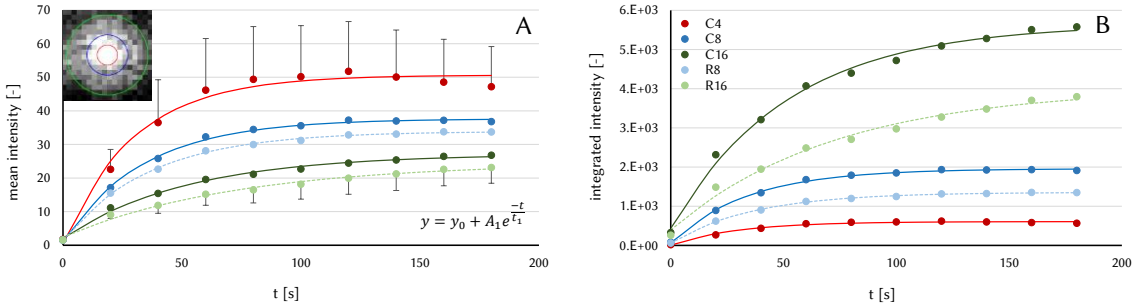

Figure 4-4 Correlation of mean (A) and integrated (B) fluorescence intensity for different ROIs with the duration of the applied AC-field. An AC-field with f = 20 kHz and U = 3.5 Vrms was applied for 180 s. Five ROIs were defined: three circular ROIs (solid lines) with a diameter of 4, 8 and 16 px (C4 - red, C8 - blue and C16 - green) as well as two ring-shaped ROIs (dashed lines) with outer diameters of 8 and 16 px (R8 – light blue and R16 – light green) and inner diameters of 4 and 8 px, respectively. All ROIs were concentrically aligned (as shown in the upper left corner). The evaluation was performed on 30 electrodes from the outermost row (row 1). All values are BG-corrected, 1 px = 147.5 nm x 147.5 nm. (A) Mean fluorescence intensity (circles: data; lines: exponential curve fit with equation (4); C4: y0 = 50.6, A1 = - 49.9, t1 = 29.9, R2 = 0.98; C8: y0 = 37.7, A1 = - 36.3, t1 = 34.1, R2 = 0.99; C16: y0 = 27.2, A1 = - 25.1, t1 = 52.2, R2 = 0.99; R8: y0 = 33.9, A1 = - 32.3, t1 = 36.7, R2 = 0.99; R16: y0 = 24.6, A1 = - 22.2, t1 = 73.3, R2 = 0.99). Error bars indicate standard deviation and are displayed only for the top and bottom curve. (B) Integrated fluorescence intensity. Grey values of all pixels within one ROI were summed up (circles: data; lines: exponential curve fit with equation (4); C4: y0 = 607.7, A1 = - 599.4, t1 = 29.9, R2 = 0.98; C8: y0 = 1957.9, A1 = - 1887.5, t1 = 34.1, R2 = 0.99; C16: y0 = 5651.7, A1 = - 5211.0, t1 = 52.2, R2 = 0.99; R8: y0 = 1355.4, A1 = - 1290.7, t1 = 36.7, R2 = 0.99; R16: y0 = 4036.5, A1 = - 3637.6, t1 = 73.3, R2 = 0.99). AC: alternating current; BG: background; ROI: region of interest. (modified from [11])

the slope is strongest and t_1 is smallest for C4. However, the limited optical resolution of approximately 550 nm for the 60x objective combined with the Cy5-filter set does not provide enough information to differentiate whether the viral material is drawn to the surface or the edge of the electrodes. A detailed discussion on this topic will be provided in later sections of this thesis (4.3.3). In this study, the data for C4 showed that a plateau was reached from 80 s, indicating that a saturation closely at the nanoelectrodes had occurred. Four potential explanations for this saturation are considered. (I) Firstly, it can be suggested that the viral material in the volume had been depleted, but the sustained increase in intensity for C8 and C16 from 80 s and the increasing intensity up to 180 s for the electrodes in rows 2-4 (as shown in chapter 4.3.1.3 and Figure 4-5) prove otherwise. (II) Secondly, equation (1) demonstrates that the DEP force is dependent on the gradient of the electric field-squared $\nabla|E|^2$. Electric field plots of the cylindrical electrodes show, that the gradient of the electric field is strongest at the electrode edge but decays quickly with distance [106, 144]. Due to the relatively large distance of 80 µm between the electrode chip and

counter electrode, the electric field is uniform for most of the volume above the nanoelectrodes, with the electric field lines being parallel to each other and perpendicular to the chip surface. Therefore, no dielectric force affects the viral material in this region. As a result, there is a height limitation of approximately less than 1 µm above the electrodes at which viruses experience a substantial dielectric force. (III) Thirdly, the amount of immobilized viral material is further limited by the insulating nature of the sample. When immobilized to the electrodes the viral material shields the electric field, with the degree of shielding increasing with layer thickness. (IV) Finally, the mere presence of viral material hinders further accumulation.

As described before the strong viral collection close to the edge is demonstrated by the smallest t_1-value of 29.9 for C4. This value increases to 34.1 for C8, an ROI (d = 1.18 µm) covering the electrode as well as the surrounding area up to a distance of 340 nm from the electrode edge. And finally, t_1 = 52.2 for C16, an ROI (d = 2.36 µm) covering the electrode as well as the surrounding area up to a distance of 930 nm from the electrode edge. From 80 to 140 s, the average intensity of C4 is oscillating around 50 ± 2. Between 140 and 180 s, the average intensity declines by 5.8, possibly due to bleaching or self-quenching. C8 reaches a plateau at 120 s and then fluctuates around an average intensity of 37 ± 0.5. Following electrode saturation, the viral material accumulates increasingly in the inter-electrode space. The greater the distance from the electrode edge the smaller the influence of the dielectrophoretic force. Thus, a gradient is formed in the density of the accumulated virus material, decreasing from the electrode edge towards the inter-electrode space. Consequently, the asymptote is decreasing from 50.6 for C4 to 37.7 for C8 and 27.2 for C16.

The slope at t_0 for C4, C8, and C16 is equivalent for both integrated and mean intensity, as evidenced by comparing the t_1 values for each type of intensity. However, the integrated intensity measurements have resulted in a reversed order of the graphs, where the highest values are observed for C16 and the lowest values for C4 (Figure 4-4B).

In order to include viral material collected at the electrodes as well as the material spreading from the edge to the inter-electrode space in subsequent analyses, a circular ROI measuring 16 px in diameter was selected.

4.3.1.3 Immobilization of viral material and side effects

The change in the amount of immobilized viral material over time was observed. Therefore, an electric field was applied for 3 min and the fluorescence intensity was measured every 20 s. Figure 4-5 illustrates the time-dependent intensities of 30 electrodes for each of the outer seven rows. The collection of viral material starts immediately after the electric field was switched on. An uneven distribution decreasing from the outer rows to the inner ones can be observed from an early stage on (Figure 4-5B, C). This uneven distribution has also been observed for the dielectric immobilization of BSA [109] and enzymes [71].

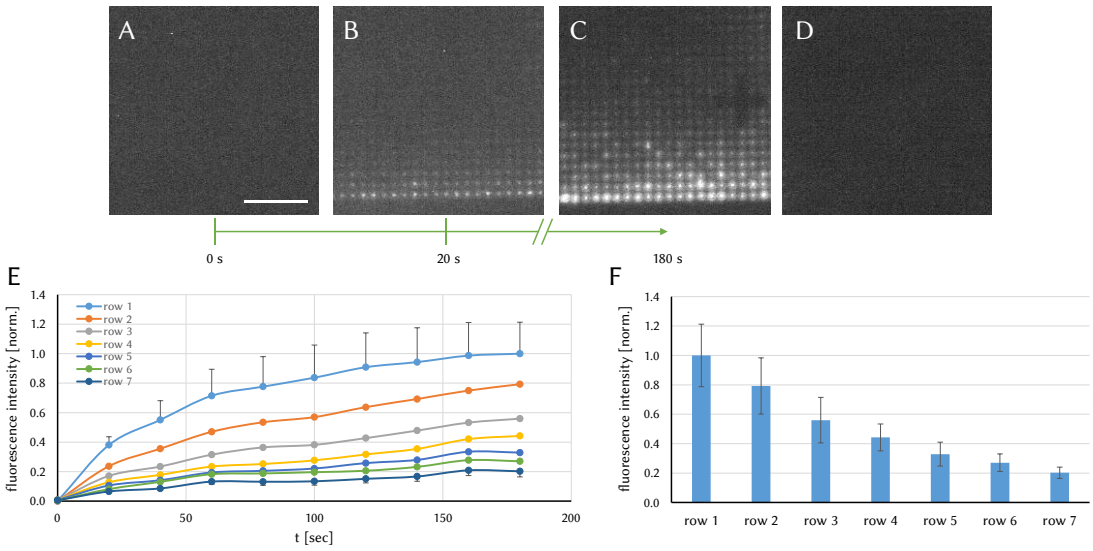

Figure 4-5 Time-dependent accumulation of viral material to the electrodes. An electric field was applied for 3 min, at 20 kHz and 3.5 V_{rms}. (A-C) Fluorescence images after 0 s, 20 s and 180 s of field application. (D) Negative control. An unused neighboring array from the same chip. (A-D) 60x objective, Cy5 filter set, exposure time: 500 ms, scale bar: 15 µm. (E-F) Background corrected, normalized fluorescence intensities of 30 electrodes from rows 1-7 each. (E) The temporal development for each row for the time span of 180 s. (F) The fluorescence intensity after 180 s for each row. All fluorescence images have same contrast settings. (modified from [11])

The gradient can be explained by a variety of causes. The first one is the distribution of the electric field strength E as well as of the electric field gradient $\nabla|E|^2$ over the entire electrode array. In their paper, Laux *et al.* have immobilized BSA on an array of cylindrical nanoelectrodes [109]. They revealed a good correlation between atomic force (AFM) measurements, meaning the amount of immobilized BSA, and field simulations. For their field

simulations, they computed, among others, the field distribution of 45 electrodes from the corner of an array, thus showing a stronger E and $\nabla|E|^2$ for the edge electrodes and especially for the corner electrode. This stronger E and $\nabla|E|^2$ span over the outer three rows until they reach a steady value. So, even though the array is made up of thousands of electrodes, looking from above, this array exhibits the characteristics of a single square-shaped electrode. Here, E and $\nabla|E|^2$ are strongest at the edge, as it was also demonstrated for a variety of electrodes like IDEs [35, 145], castellated [35, 46], quadrupole [35, 46, 146] and circle-shaped ones [81]. The electric field gradient $\nabla|E|^2$ is a measure for the dielectrophoretic force F_{DEP}. It is therefore to be expected and it is also shown in the sources mentioned that the amount of immobilized material correlates with $\nabla|E|^2$.

Another factor is the number of neighboring electrodes. The corner electrode has only two adjacent electrodes, while the edge electrodes have three, and those from the second row have four (Figure 4-6A). Consequently, the corner and edge electrodes face less competition for viral material as compared to the inner electrodes.

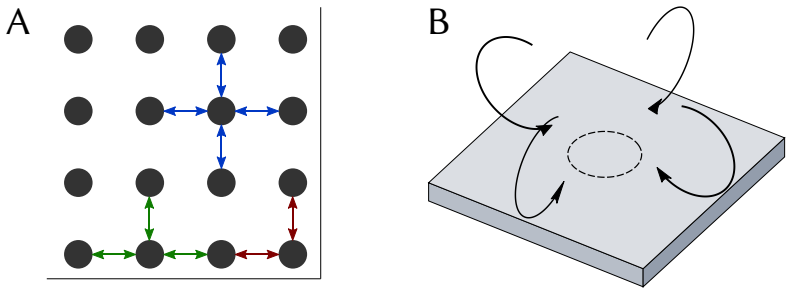

Figure 4-6 Ratio of electrodes to neighboring electrodes (A) and flow direction at electrode array (B). (A) The corner electrode has two direct neighbors (red arrows), the edge electrodes three (green arrows) and the center electrodes have four direct neighbors (blue arrows). (B) Flow pattern and vortex formation at the edge of the used nanoelectrode array. The fluid comes from the outside of the array, flows to the edge, across the outer rows towards the arrays center and then back into the volume. This streaming prevents accumulation of viral material at the array center (dashed lines).

The two reasons mentioned so far explain how the stronger accumulation at the array edge comes about. Further explanations follow, giving even more reasons for this edge accumulation and at the same time explain why the gradient goes beyond the outer 3 rows.

Polarizable particles in suspension subjected to an AC electric field are exposed to a variety of forces such as gravity, buoyancy, Brownian motion and DEP. Additionally, there are also two main forces generated by the electric field acting on the surrounding fluid: (I) ACEO, and (II) electrothermal fluid flow. Submicrometer particles are exposed to a more complex interplay of these forces than larger biological objects like cells. Giving a brief insight: The dielectrophoretic force, which scales with the particle radius, weakens as particle size decreases. Conversely, Brownian motion intensifies as particle size diminishes. Figure 4-7A illustrates that a three-fold increase in applied voltage can result in an one-order-of-magnitude increase in particle displacement. Therefore, while a 100 nm particle is primarily governed by Brownian motion at 5 V, at 15 V, DEP becomes the dominant force [57]. However, a stronger electric field induces higher local heat, leading to the emergence of electrothermal fluid flow. In the presence of an electric field, gravity and buoyancy play a minor role in particle motion. Thus, DEP competes mostly with ACEO and electrothermal fluid flow. In AC fields fluid can stream in different directions and at different velocities depending on several factors like frequency, voltage, fluid conductivity and permittivity as well as the geometry and size of the electrodes.

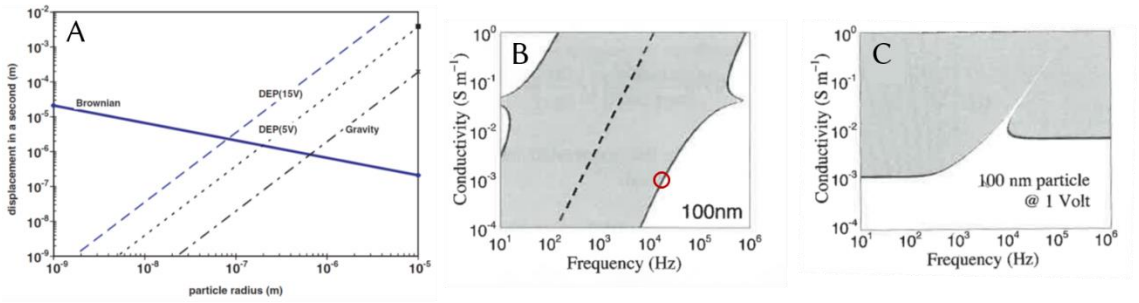

Figure 4-7 Overview of the different forces acting on a particle in an electric field. (A) Influence of gravity, Brownian motion and dielectrophoresis on the displacement of a particle in 1 s. [57] (B) Frequency and conductivity dependence of ACEO and DEP for a 100 nm particle. White is the area where DEP dominates, grey the area where ACEO dominates. The dashed line marks the characteristic frequency of electrode polarization. The red circle marks the position of the used influenza sample with a diameter of about 100 nm, an applied frequency of 20 kHz and a conductivity of about 10 µS/cm. (C) Frequency and conductivity dependence of electrothermal fluid flow and DEP for a 100 nm particle. White is the area where DEP dominates, grey the area where electrothermal fluid flow dominates. (B and C modified from [41]).

ACEO flow is created due to the interaction between the tangential part of the electric field E_t and the ions of the electrical double layer at the electrode surface [45, 50, 147]. In their study, Green *et al.* utilized particle image velocity (PIV) techniques to experimentally observe the fluid flow generated by ACEO [50, 51]. Therefore, they used a pair of parallel plate electrodes on a glass substrate, which were 2 mm long, 120 nm thick and 100 µm with a gap of 25 µm. They tracked the motion of latex beads at a frequency range of 10^2 to 10^5 Hz with a fluorescence microscope and a digital camera in a plane normal to the electrode surface. With their setup they could observe that without any fluid streaming, at low and high frequencies, the particles are drawn to the edge of the electrode due to pDEP. When the frequency was adjusted to the mid-range, the fluid flow intensified and carried the particles from the edge onto the surface. As a result, some of the particles accumulated in bands on the electrode surface, which were located either close to the edge or closer to the center of the electrode, depending on the frequency. Meanwhile, other particles were carried along with the flow, creating a visible vortex-shaped fluid flow pattern. The highest velocity was measured at the edge due to the strong electric field. Based on these measurements Figure 4-7B shows the domination of DEP and ACEO depending on the frequency and conductivity for an insulating 100 nm particle. The used combination of influenza viruses having a diameter of about 100 nm, a medium conductivity of about 10 µS/cm and an applied frequency of 20 kHz leads to a position at the border in Figure 4-7B where ACEO force and DEP force are equal. However, this only holds for a homogeneous, isolating particle, whilst the virions interior is more complex being composed of RNA, proteins and presumably cytoplasm. Furthermore, the electrode structure is different.

When it comes to electrothermal fluid flow, an applied electric field generates a temperature gradient in the fluid and thus a gradient in density, permittivity and conductivity is formed. Fluid flow is created by buoyancy forces and the interactions of the electric field with the gradients in conductivity and permittivity [45, 148, 149]. The source of the temperature gradient can be internal, as joule heating, or external, as illumination. Both numerical modeling and experimental observation using PIV indicate that the direction of the flow pattern can be influenced by the frequency applied and the presence of an external heat source [148, 150]. In contrast to ACEO, where the center of the vortex is positioned nearer to the edge of the electrodes, the center of the vortex in electrothermal fluid flow is situated closer to the center of the electrode surface and deeper within the volume. Figure 4-7C demonstrates that the influence of DEP and electrothermal fluid flow on a 100 nm particle is determined by the applied frequency and conductivity [41]. The

intensity of the electrothermal fluid flow is affected by the conductivity, with higher conductivity resulting in a stronger electrothermal fluid flow. By increasing the applied potential, the grey area shifts downwards, indicating that electrothermal fluid flow can become dominant even at lower conductivities.

If we relate all this to the context of manipulating 100 nm virus particles using a nanoelectrode array, we get to see the multi-layer complexity of this subject. The dynamics of the fluid flow is dependent upon particle characteristics, such as size and dielectric properties, as well as on other factors such as the applied frequency and voltage, conductivity, permittivity, and electrode design. It is also important to note that previous findings in the literature are not directly applicable to the nanoelectrode array used here due to differences in electrode geometry, experimental objects, and operating parameters. As a result, the precise mechanisms underlying fluid flow and particle manipulation still remain uncertain. However, it is evident that the spatial manipulation of viral particles is not solely achieved through dielectrophoresis, but rather a combination of different AC electrokinetic effects including electrothermal fluid flow.

Referring to the nanoelectrode array used in this thesis, AC electrokinetic effects generate a fluid motion in a vortex shape at all four edges of an activated array. At each edge, the fluid streams from outside the array towards its edge, then moves across the outer rows of electrodes towards the center of the array, and finally flows upward and back into the volume (see Figure 4-6B). The fluid streaming prevents the viral material from accumulating at the central part of the array and creates a viscous drag force on the viral material. The drag force on a spherical particle is determined by Stoke's law:

$$F_{drag} = 6\pi\eta r v \tag{5}$$

where η is the viscosity of the fluid, r is the particle radius, and v is the particle velocity [151]. $6\pi\eta r v$ is the friction factor of a sphere. Equation (1) demonstrates that the strength of the DEP force is directly proportional to the volume of the particle. On the other hand, the drag force is proportional to the particle radius (equation (5)). As the size of the particle decreases, the DEP force decreases at a faster rate than the drag force. Thus, the drag force has a more significant effect on the movement of viral particles than on commonly manipulated objects by DEP such as mammalian cells or bacteria in the same electrode setup.

Considering all factors, including (I) the higher $\nabla|E|^2$ strength at the edge of the array when seen as a single square-shaped electrode, (II) the count of neighboring electrodes, and (III) the AC electrokinetic effects and the drag force operating on the virus particle, depending on the spatial position either the DEP force or the drag force is dominant on a viral particle. The accumulation of viral material towards the electrodes leads to the formation of a stack, which determines the fluorescence intensity. The height of this stack is determined by the DEP force or $\nabla|E|^2$, as well as the competing drag force. The temporal development of immobilization (Figure 4-5E) demonstrates an exponential correlation (equation (4)) across all analyzed rows, with R^2 values ranging from 0.94 to 0.99. The fluid flow carries the viral particles to the array edge. Here parts of the viral material is drawn to the electrodes by pDEP. Row 1 experiences strong immobilization due to the strong $\nabla|E|^2$ gradient, the presence of few neighboring electrodes, and being the first electrodes to receive fresh viral material. A plateau formation can been seen. The reasons for this plateau formation is explained in detail in chapter 4.3.1.2. The time constant t_1 increases from 51.9 for the first row to 85.2, 108.9, and 187.1 for rows 2-4, respectively, due to the decrease of $\nabla|E|^2$ with increasing row number. A steady supply of viral material from the sample volume is indicated by the continuous increase in fluorescence intensity up to 180 s for rows 2-4. A plateau formation is also anticipated for these rows, with a time delay resulting from the dominance of row 1 and a smaller maximum value than row1 caused by the smaller $\nabla|E|^2$. Starting from row 5, the interplay between DEP force and drag force becomes more distinct. The data indicates the formation of a plateau at an early stage, and the intensity at 180 s is less than 30 % of the intensity observed in row 1. At this point, the DEP force continues to immobilize viral material, but due to a weaker $\nabla|E|^2$ and the existing drag force, there is a stronger height limit. There exists a good correlation between the modeled values of $\nabla|E|^2$ plus the height profiles of immobilized BSA from [109] and the endpoint fluorescence intensities for all 7 rows displayed in Figure 4-5F.

The benefit of the current fluid flow lies in its continuous delivery of a greater amount of viral material from the volume. So not only viral particles in spatial proximity or particles coming into spatial proximity by diffusion are being immobilized. ACEO and electrothermal fluid flow are even used intentionally to pump [58, 152] or mix samples [59, 153].

For a better understanding which effect is the dominant cause of the fluid streaming at the nanoelectrode array one could have a closer look at the shape and velocity of the vortices. As previously noted, the electric double layer is responsible for fluid streaming induced by ACEO,

resulting in vortices located near the electrode edge. In contrast, the center of the vortices resulting from electrothermal fluid flow are located further into the volume above the electrode. Increasing the conductivity would slow down the streaming velocity if caused by ACEO, while the velocity would increase if caused by electrothermal fluid flow. [50, 51, 57, 148]

To minimize those streaming effects and to aim for a more even distribution different strategies are possible. (I) ACEO is zero at small and high frequencies. So, one could look for a frequency window where ACEO is small, pDEP is still possible and electrothermal fluid flow is not emphasized. (II) Appling a pulsed AC electric field. Achieving the appropriate ratio between the pulse and break periods might result in immobilization through positive dielectrophoresis (pDEP) and impede temperature increase during cool-down phases. (III) An external heating source that allows the electrothermal flow to be controlled. In literature the use of an external heat-source was applied usually to raise the temperature, resulting in increased electrothermal fluid flow and improved sample mixing, a common challenge in microfluidics [154, 155]. However, simulations have shown that reducing the temperature gradient through external heating leads to a decrease in the velocity of the electrothermal fluid flow [149]. Excessive reduction of temperature should also be avoided as it results in altered flow patterns.

4.3.2 Temporary versus permanent immobilization

Typically, pDEP-induced accumulation is a reversible phenomenon, wherein the objects are removed by diffusion or fluid flow when the electric field is turned off. The current study examined the impact of diffusion, shear forces, and rinsing on the stability of immobilization. Image acquisition was performed using a 60x objective (NA = 0.7) and a Cy5 filter set with an exposure time of 500 ms. Following 180 s of viral material accumulation at 20 kHz and 3.5 V_{rms}, the electric field was turned off, and the fluorescence signal was measured after dwell times of 0, 1, 3, 5, and 10 min to assess the impact of diffusion. Shear forces were induced by carefully lifting the ITO-cover glass with tweezers and returning it to the chip, thus the sample's meniscus runs twice across the immobilized viral material. Lastly, the chip was rinsed with ultrapure water.

In order to determine the percentage of material loss, the mean BG of an unused neighboring array was measured for each individual image, including images of diffusion, shear force, and rinsing. The corresponding BG was then subtracted from each image to correct for background noise. Within these BG-corrected images, 153 nanoelectrodes were enclosed in an ROI. The brightness values of all pixels within this ROI were then added together to obtain the integrated intensity. The percentage change in the sum of the integrated intensity in the different images was calculated relative to the initial time point of diffusion (t = 0 min). These steps and their results are presented in Figure 4-8.

At a time of t = 0 min, which is defined as the starting point for all subsequent states, the electrical field is switched off. Material, immobilized by pDEP, starts to stack up while the electric field is applied and forms multiple layers on top of the electrodes following the findings of Laux *et al.* [109]. For dwell times of 3, 5, and 10 min a decrease of the fluorescence signal was observed showing that the top layers of immobilized material start to diffuse back into the volume up to a signal loss of 24 % for a dwell time of 10 min. However, at a dwell time of 1 min, there was even a 2.8 % increase in signal. Several possible explanations for this increase include: (I) fluid streaming may not cease simultaneously with the switch-off of the electric field, resulting in the transport of new viral material into the evaluated ROI area, leading to an increase in fluorescence signal. (II) Some fluorescence dyes form dimers and cause a self-quenching effect at high concentrations. Here, the spatial distance between the dye molecules is too small, resulting in a decrease in fluorescence signal. This effect was used to develop DNA probes labeled with the same dye at both ends [156, 157]. In the case of immobilized viral material, the molecules may be tightly

packed, causing the same quenching effect. With the electric field switched off this packing should relax increasing the mutual distance between the fluorophores und thus decreasing the self-quenching effect. (III) Additionally, the high concentration of fluorophore molecules can lead to self-absorption of emitted photons.

Moving the ITO cover slip over the electrode arrays and the immobilized viral material as described creates shear forces that cause an additional loss of approximately 36 % of the material. Further, rinsing the chip with ultrapure water causes an additional loss of approximately 17 % resulting in a total loss about 77%. The remaining viral material permanently sticks to the tungsten electrodes.

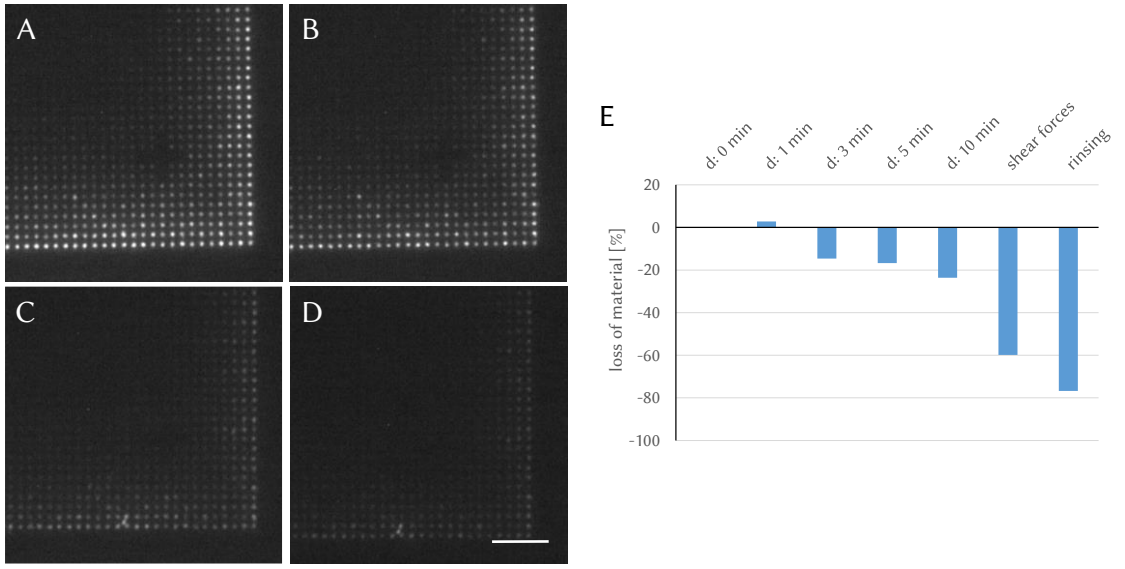

Figure 4-8 Temporary versus permanent immobilization. Fluorescence images at different time points: immediately after turning off the electric field (A), after a 10-minute diffusion dwell time (B), after applying shear forces by lifting and returning the ITO cover slip (C), and after rinsing with ultrapure water (D). The images were taken using a 60x objective and a Cy5 filter with an exposure time of 500 ms. Scale bar: 15 µm. (E) The relative loss of viral material was calculated in comparison to the initial time point of diffusion (t = 0 min). All fluorescence images have same contrast settings. d: dwell time; ITO: indium tin oxide. [11]

Only a limited number of studies in the literature have reported on the permanent immobilization by DEP in general and especially in the submicrometer range. In their study, Yamamoto *et al.* were the first to show that the electric field strength can be controlled to achieve either temporary or permanent immobilization of BSA [107]. Here, pillar-structured nanoelectrodes with a diameter of 50 nm made from a diamond-like carbon and coated with

aluminum were used. Depending on the arrangement of these nanopillars, a field strength of either 3 or 5 MV/m was required to permanently immobilize BSA. The field simulations conducted by Knigge share high similarities with the cylindrical electrodes utilized in the present thesis. These electrodes, with a diameter of 435 nm, a potential difference of 1 V, and a spacer of 99 µm, were found to have a maximum field strength of around 0.2 MV/m [144]. This translates to 0.7 MV/m for the present study. Demonstrating that the use of nanoelectrode arrays led to the permanent immobilization at much lower field strengths compared to the findings reported by Yamamoto.

However, equation (1) indicates that the CM-factor ranges between -0.5 to +1, thus the predominant factors influencing F_{DEP} are the particle's diameter and the gradient of the electric field. Considering the literature, electric field gradients between 10^{12} and 10^{24} V^2/m^3 were applied to immobilize proteins by DEP [158, 159]. Nevertheless, with very few exceptions [107], only temporary immobilization was reported. With an electric field gradient of about 10^{17} V^2/m^3 for the field simulations by Knigge [144], the electrodes used in this thesis are within the mentioned gradient range and still lead to permanent immobilization of the viral material. In addition to the permanent immobilization of virus material, previous research utilizing the same electrode design has successfully achieved permanent immobilization of biomolecules, such as BSA [109] and enzymes [71, 108], as well as polystyrene nanobeads [110]. This demonstrates that the electric field gradient is not the only factor deciding about permanent immobilization when it comes to tungsten cylinder electrodes. Knigge *et al.* have demonstrated that the degree of permanent immobilization of nanobeads is size-dependent [110, 144]. Polystyrene nanobeads in the size range of 100 nm to 2 µm were immobilized with the same chip design as used in the present thesis. While particles from 500 nm to 2 µm could be removed, the immobilization of the smaller ones with a diameter of 100 nm and 200 nm was irreversible.

The cause of the permanent immobilization remains unclear. It is possible that the attraction of viral material disrupts the hydration layer on the electrode surface and on the virus surface, leading to hydrophobic interactions and van der Waals forces between the viral surface proteins and the electrodes. Further investigations are necessary to gain a better understanding of the protein-surface interactions. Altering the surface proteins or the surrounding medium is expected to influence the strength of van der Waals forces. Therefore, comparative experiments involving modified viral surface proteins through protein digestion or crosslinking, as well as changes in the pH value, ionic concentration, or ionic composition of the medium may be appropriate. An

alternative approach could be to modify the electrode's surface by either using a different type of metal - although Ag, Au and Pt are not CMOS compatible - or covering the electrode's surface with an insulating layer.

To the best of our knowledge, there are no published studies reporting the permanent immobilization of viral particles using DEP. A disadvantage of the permanent immobilization of viral particles is that the chip can only be used once, making it a single-use device. In order to maintain experimental cleanliness, a new chip must be used for each experiment. However, the benefits of this approach outweigh the limitations since the functionalized chip can be used without the need for an electrical field, without the bulky electrical setup, or without a flow-through system.

4.3.3 Spatial distribution of viral material on the electrodes

The resolution of a microscope is limited by various factors such as the wavelength of light, the numerical aperture (NA), diffraction, the refractive index of the medium between the objective and sample, the sample thickness, imperfections in lenses, and misalignment. Due to the limited optical resolution of approximately 550 nm for the 60x objective (NA = 0.7) and the Cy5 filter-set, it is challenging to differentiate whether the viral material is attracted towards the surface or edge of the nanoelectrodes. To overcome this limitation, images were deconvolved to improve their resolution and quality. Therefore, the effects of a known convolution process are reversed or removed, which can occur when an image is taken by an optical system. This is accomplished by mathematically modeling the point spread function (PSF) of the microscope. The PSF describes how light gets spread and deflected as it passes through the optical system of the microscope. By deconvolving the image with the PSF, the blurred features in the image can be restored to their original sharpness, improve the contrast and the signal-to-noise ratio. [160, 161]

The deconvolution of fluorescence images has various applications, including detection of single RNA molecules [162], colocalization analysis [163] and structural investigation of the yeast actin cytoskeleton [164]. The output of the deconvolution relies on factors such as parameter settings, the specific image being analyzed, and the used algorithm. In their study, Sage *et al.* compared various deconvolution algorithms available in the *DeconvolutionLab2* plugin for *ImageJ* [165]. The naive inverse filtering (NIF) algorithm produced significant artifacts, while the Tikhonov regularization (TR) and regularized inverse filtering (RIF) algorithms led to ringing artifacts. Iterative algorithms, such as Landweber (LW), Richardson-Lucy (RL), and Tikhonov-Miller (TM), demonstrated the best results [165].

For a better spatial resolution, the optical system's PSF used was determined (NA = 0.9; wavelength: 664 nm; pixel spacing: 86 nm), and the fluorescence image was deconvolved using the Richardson-Lucy algorithm. While in the original image, the electrodes have a blurred and cloudy appearance (Figure 4-9A), they show a clear shape after the deconvolution (Figure 4-9B). Furthermore, the distribution of viral material differed for each electrode, with some showing distinct accumulation at the electrode's edge, resulting in a ring-shaped or almost ring-shaped fluorescence signal. While for other electrodes, the accumulation of viral material was observed to be arbitrary or indistinguishable between surface and edge accumulation. Consequently, each electrode has a unique accumulation pattern and can be considered as a single event.

The summation projection from Figure 4-9C was generated by identifying and isolating each of the 119 electrodes, and then adding up their individual gray values. While each electrode has an individual distribution of viral material, the merging of those events results in an overall ring-shaped distribution at the edge of the electrode. In chapter 4.3.1.3 it is explained that viral particles are subjected to various forces and side effects. These include electrothermal fluid flow and ACEO, which create a fluid streaming pattern that moves from the outer rows to the inner ones and back in the volume (Figure 4-6B). This flow pattern results in the transportation of new viral material to the electrodes and affects the spatial distribution of immobilized viral material. The summation projection from Figure 4-9D is based on 64 electrodes that were exposed to a fluid stream that came from beneath the electrodes, as indicated by the blue box in Figure 4-9B. This flow resulted in an enhanced accumulation of viral material at the bottom half of these electrodes, which is enhanced in the summation projection. The red area, located in the lower right corner of the array, is exposed to fluid flow from beneath as well as from the right. This flow pattern caused a pronounced accumulation of the viral material on the bottom right side of the summation projection in Figure 4-9E. These results underscore the importance of taking global fluid flow effects into account when analyzing the spatial distribution of immobilized material on nanoelectrode arrays.

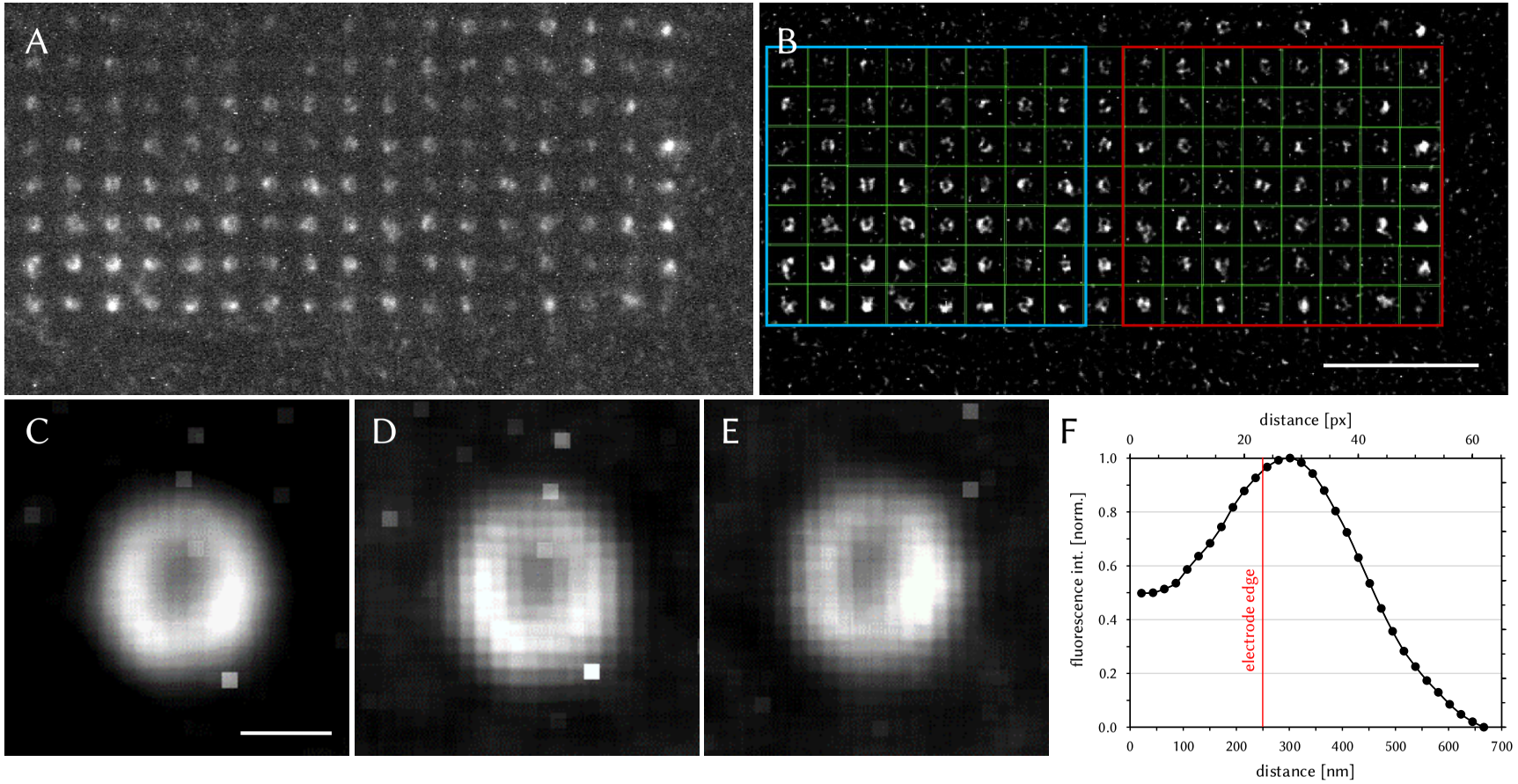

Figure 4-9 Deconvolution and spatial distribution of the accumulated viral material. (A) Original fluorescence image of the bottom right corner of a nanoelectrode array. Taken with a 100x objective (NA = 0.9), a Cy5-filter and an exposure time of 5 s. (B) Deconvolved image using the PSF and the Richard-Lucy algorithm (N = 100). The deconvolution process improved the resolution of the original image, resulting in sharp fluorescence signals for each electrode. (C) Summation projection of all 119 nanoelectrodes from the green ROIs. (D) Summation projection of the individual electrodes from the blue ROI. (E) Summation projection of the individual electrodes from the red ROI. (F) Normalized mean fluorescence intensity as a function of distance for (C). The x-axis starts at the electrode center. The red line marks the electrode edge. Scale bar from (B) = 10 µm, scale bar from (C): 500 nm. ROI, region of interest. (modified from [11])

To determine the spatial distribution of immobilized viral material, the normalized mean fluorescence intensity of concentric aligned rings covering the area from the center of the electrode to a distance of approximately 400 nm from the electrode edge was plotted (Figure 3.7F). The red line indicates the position of the electrode edge. The plot displays a graph that starts from the electrode center with an intensity of about 0.5, increases and finds its peak at about 50 nm outside the electrode edge. The fluorescence intensity decreases as distance increases, reaching zero at around 450 nm from the edge. This ring-shaped accumulation is consistent with both theory and field simulations that show that field strength and field gradient are strongest at the electrode edge. When it comes to the cylindrical shaped electrodes used in this thesis, detailed field simulations can be found in [106, 144]. These simulations confirm that the electrode edge has the highest field gradient, resulting in a stronger DEP force and accumulation. Upon closer inspection, a radial outward shift of the electric field gradient can be seen in the simulations, which is caused by the electric field bending at the electrode edge. Consequently, the viral material accumulates in a peak that is shifted diagonally 50 nm away from the edge, rather than directly above it at a 90-degree angle.

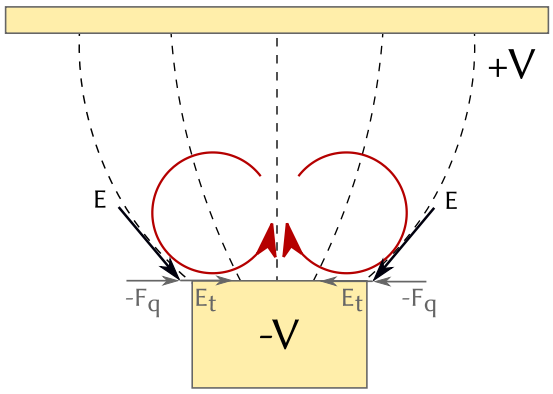

Figure 4-10 ACEO fluid flow on top of the electrode surface. Applying an AC electric field E (dashed lines) gives rise to the polarization of the electrodes. Charges accumulate at the surface of the electrode (not shown). The tangential part E_t interacts with those charges and the resulting force F_q is expected to lead to the formation of a fluid motion towards the electrode's center (red arrows). Here, one half of the AC period is shown.

While the intensity decreases with increasing distance from the electrode, the intensity at the electrode center remains constant at 50%. ACEO has been considered as one of the side effects to

explain the fluid flow in the region above an entire activated array (chapter 4.3.1.3). However, it can also be used to clarify the attraction of viral material to the electrode surface, where the electric field gradient is much smaller than at the electrode edge. When an AC electric field E is applied to the electrodes, ions accumulate at the surface between electrode and the medium. The electric field then exerts a force on these ions, which causes them to be dragged by the tangential component of the electric field E_t. This drag creates a suction and a fluid flow, which leads to the force F_q. In an AC field, the potential sign changes periodically, which causes induced ions and the direction of the tangential force to change accordingly. However, the direction of the force vector and the fluid flow direction remain the same [166, 167]. For tungsten cylinder electrodes, the tangential component of the electric field points circular from the edge to the center of the electrodes, and it becomes zero at the electrode center. Thus viral material is dragged from the edge to the surface of the electrode. A schematic illustration of the ACEO fluid flow is shown in Figure 4-10. This illustration is analog to the mechanism of ACEO at IDEs presented by Morgan and Green in [41]. This phenomenon was employed to focus bacteria, yeast cells, spores, latex beads and DNA in a controlled manner at the center of electrode surfaces [46, 54, 55]. This implies that immobilization of viral material occurs through the combined effects of various electrokinetic phenomena.

4.3.4 Conclusion

Under the given electrode setup and under the given conditions, it was demonstrated that it is possible to immobilize objects in the size range of approximately 100 nm, here specifically influenza virus particles. Parts of the immobilized influenza material adhere permanently to the electrodes, although the reason for this permanent immobilization remains uncertain. Nevertheless, an explanatory approach was presented, as well as proposals for further investigations. Even though this permanent immobilization turns every chip into a single-use device, functionalized chips can be used independently from the electrical setup. In general, this permanent sticking simplifies handling for most of the applications presented in this thesis. In particular, it can serve, for example, as a fixation method for structural analysis by super-resolution microscopy, which is still a challenge today [168, 169].

A variety of forces act on a suspension of 100 nm particle in a non-uniform AC electric field. Following the current literature it is still an open question which force is the dominant one. Thus, these forces are grouped together as AC electrokinetic effects comprising DEP, ACEO and electrothermal fluid flow. ACEO and electrothermal fluid flow create a vortex-shaped fluid motion, resulting in a drag force on the virus particles that competes with the DEP force. This leads to a gradient of the immobilized viral material decreasing from the outer rows to the inner ones. The advantages and disadvantages of the gradient formation were presented, as well as suggestions for its minimization.

Last but not least, the examination of the spatial distribution at the level of individual electrodes shows, that the majority of the immobilized viral material was drawn to the electrode edge with a radially outward shift due to the bending of the electric field. Parts of the immobilized viral material is located at the surface of the electrodes, presumably due to the transport by ACEO.

The platform presented in this study enables the rapid functionalization of electrode surfaces with minimal sample consumption. The electrodes are arranged in a regular pattern, which allows for automated evaluation and statistical analysis. A broad range of applications related, but not limited, to 100 nm objects exists. Some potential applications of this platform include: (I) Firstly, the four electrode arrays can be functionalized individually, enabling multiparameter measurements. One array can serve as an internal control and an upscaling to more than four nanoelectrode arrays is possible as well. Thus, the characterization of various influenza subtypes

or different viruses like the corona virus is possible. (II) Secondly, single virus particle analysis is feasible, as demonstrated by Knigge *et al.* in their research on the singling of polystyrene nanobeads [110, 144]. The optimal size ratio between particle diameter and electrode diameter for successful singling was found to be about 2:1, meaning the particle diameter should be about double the diameter of the cylindrically shaped electrode. Therefore, single virus particles could be analyzed using an electrode diameter of approximately 50 nm. This can benefit the study of single-virus membrane fusion studies with, for example, membrane vesicles, as the infection mechanisms of enveloped viruses are still up for debate [170–172]. (III) The fusion analysis from the previous point can be expanded to the fusion of viruses with their host cell. Host cells could be singled out on the electrodes and the interaction between cell and viruses can be tracked. (IV) Surface-enhanced Raman spectroscopy (SERS) is a method that amplifies Raman signals from biosamples by several orders of magnitude [173]. This technique involves increasing the scattering efficiency of samples by adsorbing them onto metal colloidal nanoparticles or rough metal surfaces. The SERS spectroscopy has been widely used for analyzing various biosamples, including viruses like influenza and corona [174, 175]. In this regard, ACEK forces can be employed to immobilize gold or silver nanoparticles onto the nanoelectrodes to create a suitable SERS substrate [176]. Thus, single particle analysis by SERS is plausible. (V) Through the optimization of experimental parameters, it may be possible to achieve an improved separation of DEP and ACEO. This would enable the same electrode to be functionalized successively by two different object species. For instance, DEP could be utilized to accumulate object type A at the rim, while ACEO could be utilized to accumulate object type B on the surface. (VI) As an immunoassay, e.g. to detect antibodies in sera. This last one, a potential application as an on-chip immunoassay, will be presented and discussed in the following chapters.

4.4 On-chip immunoassay

In the following sections, the initial stages of a prospective implementation of the presented platform as an on-chip immunoassay are presented. Here, the focus is on two distinct approaches: (I) utilizing ACEK effects to immobilize influenza viruses as the bio-receptor, with the anti-H3 antibody serving as the analyte, and (II) the same system rotated by 180 degrees. Preliminary experiments, like the chip passivation, are described and sources of error are identified. In the end achievements, but especially aspects that were unsuccessful, are discussed.

4.4.1 Approach 1 - Influenza virus as the bio-receptor

4.4.1.1 Identification of sources of error – indirect ELISA and FLISA

In the first attempts of an on-chip immunoassay nanoelectrode chips were functionalized with DY-634 stained viruses as described in chapter 3.12.1. After several failures to measure any binding of an antibody to the immobilized X-31 on chip (data not shown) a step was taken back. The electrode chips, their preparation and the electrical setup form a complex system with a lot of potential sources of error. To simplify troubleshooting the focus was set to measure only the antigen-antibody interaction by indirect ELISA.

To this end, wells of a 96 well plate were coated with 5 µg/ml of the particular antigen and incubated with a monoclonal anti-H3 primary antibody (1 µg/ml) and an anti-mouse secondary antibody, respectively. To estimate non-specific binding by the primary and secondary antibody the antigen X-31 was omitted, referred to as BG. To exclude non-specific binding between antigen and secondary antibody the primary antibody was omitted, termed NC. The reference sample was a freshly prepared, untreated, unstained X-31 sample diluted in PBS. The specificity of the anti-H3 antibody was demonstrated by using an H1N1 strain instead of X-31 (H3N2) as the antigen.

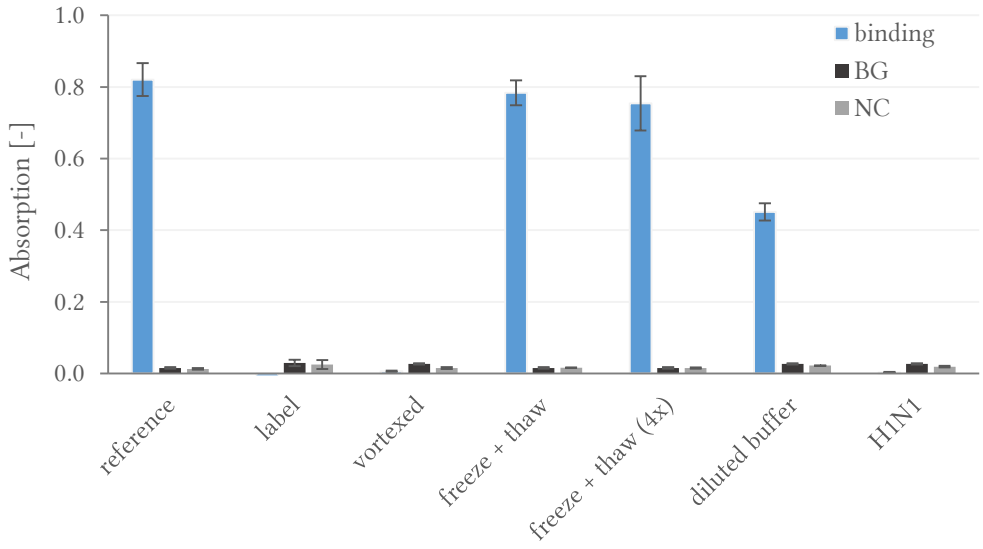

Figure 4-11 Identification of sources of error by indirect ELISA. Different potential sources of error that might prevent the interaction between the anti-H3 antibody and X-31 were considered. Reference: a freshly prepared, untreated, unstained X-31 sample diluted in PBS. Label: an X-31 sample labeled with DY-634 which covalently binds to proteins by an active NHS ester. Vortexed: the samples was vortexed for 2 min to achieve a more even particle size distribution. Freezing + thawing: the sample was frozen and thawed once or multiple times (4x). Diluted buffer: storage of the viral sample in a 1:260 diluted buffer to facilitate the ACEK manipulation. H1N1: X-31 was substituted by a H1N1 virus to demonstrate the specificity of the anti-H3 antibody.

Various potential sources of error were taken into account. (I) The protein label: For the microscopic observation of the ACEK manipulation of X-31 the virus sample was covalently labeled with DY-634 by an active NHS ester. This label was necessary to directly observe the spatial distribution of the viral material. As shown in Figure 4-11 the fluorescent dye prohibits the anti-H3 antibody from binding to its epitope located at the hemagglutinin. The dye might bind to the epitope or sterically hinders the antibody from binding. (II) Sample vortexing. The virus sample forms aggregates. For a more homogeneous size distribution, when it comes to the ACEK manipulation, the virus samples were vortexed. The ELISA experiments showed that the antigen-antibody interaction is prevented from a vortex period of 2 min at the latest. (III) Freezing and thawing. The virus samples are valuable. To protect them from spoilage they were frozen in aliquots. ELISA experiments show, that freeze and thawing cycles (up to 4x) have only a minimal impact. (IV) Storage in diluted buffer. To facilitate the ACEK manipulation and immobilize the virus material onto the electrodes, it was necessary to store the samples in a low-conductivity solution. Here, the buffer of the virus sample was diluted by diluting the X-31 sample 1:260 in

ultrapure water. Thus the X-31 sample had a concentration of 5 µg/ml and a conductivity of about 60 µS/cm. ELISA results indicate a signal strength of approximately 50% compared to the reference, suggesting that storage in the diluted buffer destabilizes the virus samples. Consequently, this affects the interaction between anti-H3 and X-31. Still, this has to be put into perspective. While for the ELISA measurement this X-31 sample was stored in diluted buffer overnight, this is not the case for the viral sample for the on-chip immunoassay experiments. Here, the storage was in a timeframe of maximum 30 min.

While with ELISA the detection is based on an enzymatic reaction, the on-chip immunoassay is a fluorescent detection system. As a consequence the ELISA measurement for the reference sample was repeated as an FLISA with the same primary and secondary antibody that will be used for the on-chip immunoassay. At first the aptitude of PBS for FLISA was demonstrated by the linear dependence between the fluorescence signal and the secondary antibody concentration in PBS (Figure 4-12A). Second of all, the concentration of the secondary antibody was determined by choosing a dilution (1:400) from the linear part of the sigmoidal curve from Figure 4-12B. Last but not least, based on these findings, the antibody-antigen interaction between anti-H3 and X-31 was also demonstrated by the FLISA (Figure 4-12C).

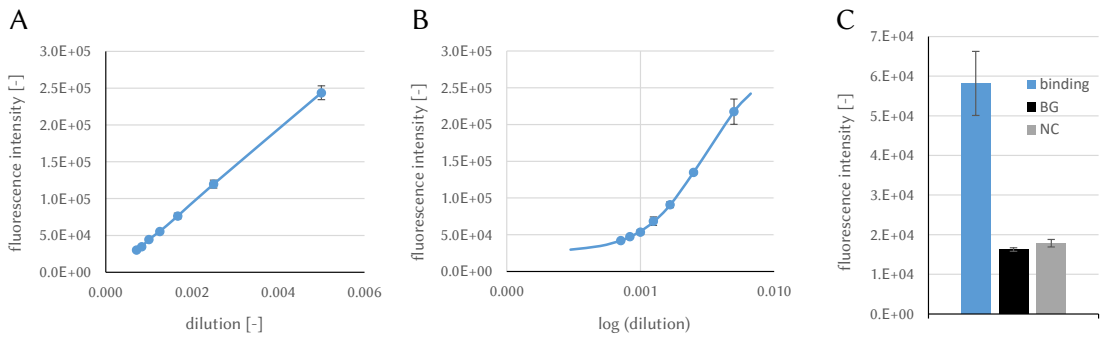

Figure 4-12 Indirect FLISA. (A) Checking the suitability of the buffer for FLISA. A serial dilution of the secondary antibody was prepared in PBS and its fluorescence intensity was measured in a plate reader. (B) Determination of the dilution of the secondary antibody. A dilution (1:400) was chosen from the linear part of the sigmoidal curve. (C) Demonstration of the antibody-antigen interaction of anti-H3 and X-31 by FLISA.

Summarizing this and drawing conclusions from it means that for the following on-chip experiments (for approach 1) the viral sample should be kept non-labeled. While it might be

feasible to achieve stained surface proteins while maintaining an antibody-antigen interaction, this was not pursued further. Instead the sample was immobilized by ACEK effects without visual control and the visualization was done afterwards with a fluorescently labeled antibody, analog to an indirect FLISA. The vortexing was reduced to a minimum, meaning that the sample was just vortexed for few seconds, for example when a dilution was made. Last but not least, the storage in diluted buffer was kept as short as possible which usually meant a maximum of 30 min.

4.4.1.2 Electrode chip passivation

Before using specific antibodies to detect the immobilized influenza virus material, all potential nonspecific binding sites on the electrode chip have to be blocked to prevent nonspecific antibody binding. If blocking is omitted, the antibodies may bind to sites that are not related to the specific antibody–antigen interaction. This can lead to incorrect results or a high background signal. Testing of different blocking solutions is needed to obtain the best possible results for a given combination of specific antibodies and other detection reagents.

Here, five different blocking solutions were tested: 3% BSA, 2% MP, 1% PEG600, 1% PEG20k and a 5 µg/ml antibody-solution. For the last one an antibody was chosen that does not bind to the X-31 virus, nor to the primary, nor to the secondary antibody, and that cannot be bound by the secondary antibody. Furthermore, in order not to compromise the stability of the X-31 virus no detergents like Tween or Triton-X were used.

As described in chapter 3.12.2 chips were incubated with the individual blocking solutions and subsequently exposed to a secondary antibody (Alexa 488 conjugated) that was diluted in the same blocking solution. The fluorescence intensity of nonspecific sticking antibodies was measured by fluorescence microscopy with a 60x objective (NA = 0.7), a WIBA filter, a 490 nm LED (at 100% setting) as illumination source and an exposure time of 2 s. The intensity of a SiO_2 area of about 1.75 μm^2 was measured. The intensity at the same position of a chip that was only incubated with PBS was defined as the BG. The same intensity measurements were done with 49 electrodes from the same chips. The negative control was defined by a chip that had not been incubated by any blocking solution. Here, “passivation” was done with PBS, followed by the incubation with the secondary antibody diluted in PBS as well. Finally, the BG-corrected values were plotted as in Figure 4-13A.

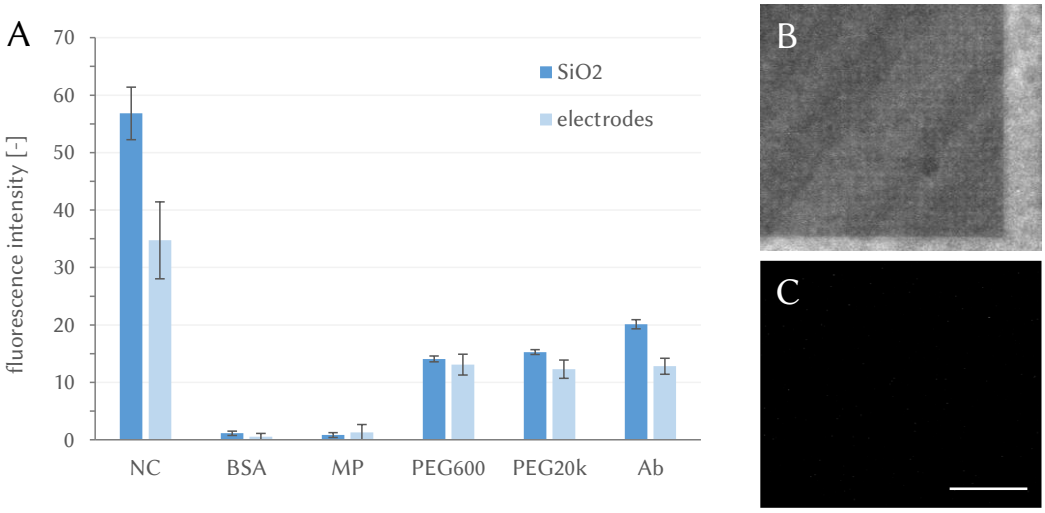

Figure 4-13 Chip passivation to prevent nonspecific binding of the secondary antibody. (A) Different blocking solutions were tested: 3% BSA, 2% MP, 1% PEG600, 1% PEG20k and a 5 µg/ml antibody-solution. The NC was a non-passivated chip. All values are BG-corrected. (B) and (C) are fluorescence images of the NC and a chip passivated with 3% BSA, respectively. 60x objective (NA = 0.7), WIBA filter, 490 nm LED, exposure time: 2 s, all fluorescence images have same contrast settings. NC: negative control; MP: milk powder; Ab: antibody. Scale bar: 20 µm.

All blocking solutions used to passivate the SiO_2 surface or the electrodes were successful in decreasing the fluorescence signal by avoiding nonspecific interactions between the surface and the secondary antibody. For example, the BG signal was reduced by 75% with a 1% PEG passivation in comparison to the non-passivated SiO_2 (NC). Best results were achieved with 3% BSA and 2% MP, which reduced the BG by about 98% compared to the NC. While the BSA solution is made up of one protein with a molecular weight of about 66 kDa, milk powder consists of multiple proteins with varying composition and quality across batches. Therefore, 3% BSA was used for passivation in on-chip experiments where chips were functionalized with X-31.

4.4.1.3 On-chip experiments

Next, a potential on-chip immunoassay was tested with the X-31 as the bio-receptor and anti-H3 as the analyte. The set-up on-chip was analogous to that of ELISA or FLISA, since a fluorescence-labeled antibody was used here.

Based on the ELISA results (chapter 4.4.1.1) the X-31 sample was kept unlabeled, was not vortexed or if so, then just as short as possible, e.g. to mix a dilution. Dilutions of X-31 were freshly made in ultrapure water and used for not more than an hour. X-31 was immobilized at 20 kHz and 3.5 V_{rms}. Based on the passivation studies (4.4.1.2) the chip was passivated with 3% BSA, and blocking as well as dilution of primary and secondary antibody were performed with 3% BSA as well. Further details are described in 3.12.3.

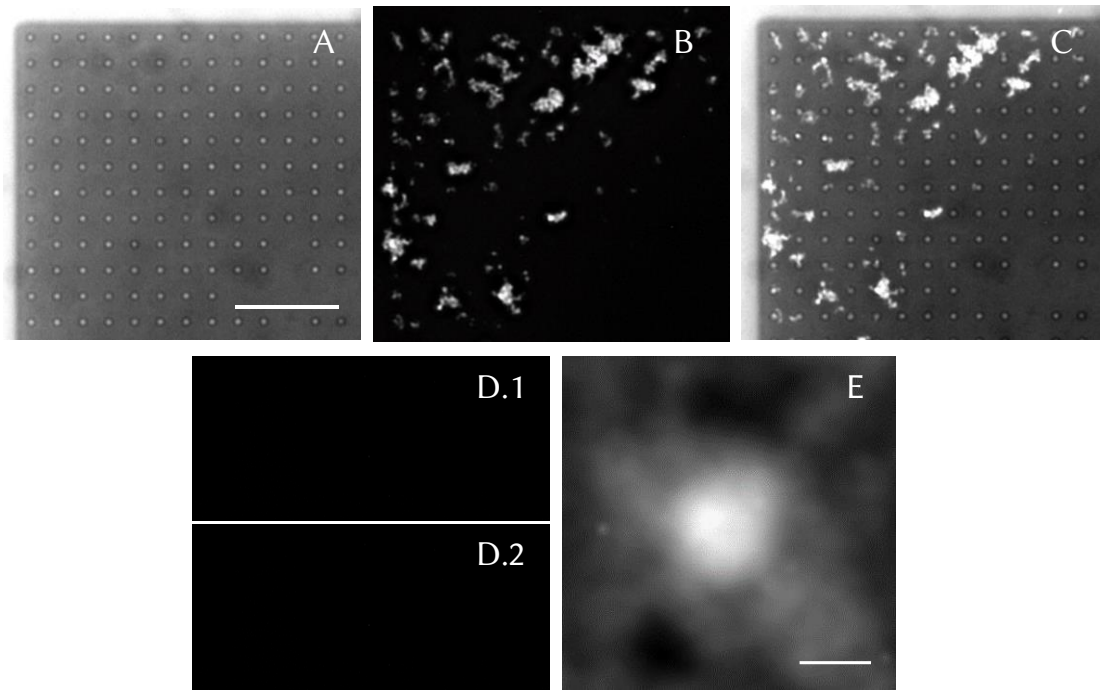

Figure 4-14 On-chip immunoassay – approach 1. (A) Bright field image of the upper left corner of an electrode array. Scale bar: 10 µm. (B) The antigen-antibody interaction between immobilized X-31 and anti-H3 is still working. Detection is based on an Alexa488 fluorescently labeled secondary antibody. Deconvolved fluorescence image: NA = 1.40, wavelength: 490 nm, image pixel spacing: 66 nm. (C) The sum of A and B. (D) Negative controls. 1 – Instead of immobilizing X-31 by ACEK the chip was just incubated with the virus sample. 2 – Anti-H3 antibody was omitted. (E) Summation projection of 119 single electrodes from B. Scale bar: 500 nm. Fluorescence images: 100x objective (NA = 1.40); WIBA filter set; exposure time: 2 s; LED: 490 nm.

Inspecting the results from the on-chip studies (Figure 4-14) shows that the blind immobilization of the X-31 was successful and an antigen-antibody interaction was still achievable. As before, there is a gradient of the immobilized X-31. Here, from about row 7 a clear drop in the amount of immobilized material appears. The most noticeable difference from previous X-31 immobilization studies (chapter 4.3) lies in the uneven fluorescence distribution (Figure 4-14B). Even with the variation from row to row, the fluorescence signal had so far been distributed around the edge of the electrode. Here, the distribution is rather cloudy and uneven. As a result of minimizing the impact of vortexing more virus aggregates are present. As known from the equation (1) the dielectrophoretic force is proportional to the particle size. As a consequence, preferentially these big aggregates are immobilized causing this cloudy and uneven distribution of X-31. These aggregates accumulate at the electrodes not as a ring but rather fill the entire electrode surface (Figure 4-14E). The strong background from this summation projection originates from the viral material in the interelectrode space. Here, viral material is not just randomly located but can usually be associated to a specific electrode, possibly because the entire aggregate was drawn to this electrode and it extends into the interelectrode space or additional aggregates have accumulated at the primary ones.

The negative controls (NC) proved evidence that the observed signal is not a result of nonspecific binding between the reaction components and the chip surface, but rather due to the binding of anti-H3 to X-31. For one of the NCs the chip was incubated with X-31 without applying an electric field (Figure 4-14D.1). In the other negative control, X-31 was immobilized by ACEK effects on the chip, but it was not incubated with the anti-H3 antibody. The remaining steps were kept as descripted in chapter 3.12.3. The specificity of the anti-H3 to X-31 was demonstrated by either substituting anti-H3 with anti-H1 or X-31 with H1N1. Both attempts yielded results similar to the negative controls (Data not shown).

Altogether, the feasibility of an on-chip immunoassay with X-31 as the bio-receptor was demonstrated. The negative controls prove that the binding signal can be traced back to the interaction between the anti-H3 antibody and the on-chip immobilized X-31 material.

4.4.2 Approach 2 - Influenza as the analyte

4.4.2.1 Spatial distribution of antibodies on the electrodes – STED

There was the opportunity to work on a STED microscope for some weeks. STED is a fluorescence microscopy technique that exceeds the diffraction limit of light. The method involves two lasers: one to excite fluorescent dyes and a second one known as the depletion laser. The last one has a donut-shaped beam that surrounds the excitation laser spot. When the depletion laser overlaps with the excitation laser, the excitation spot's outer region becomes dark, leaving only a small region in the center where the dyes remain excited. The remaining excited region can be reduced to well below the diffraction limit of light, resulting in high-resolution images. [177, 178]

Nanoelectrode chips were prepared with immobilized antibodies (15 kHz, 5.3 V_{rms}, 10 min) as described in chapter 3.11. Due to the small working distance of 0.13 mm of the 100x objective, no spacer was glued onto the chip. To prolong observation time, a glycerol droplet was used instead of water to suspend the specimen between the electrode chip and the cover slip. Antibodies from abberior were used, which were labeled with the fluorescent dye STAR RED (also known as KK114) due to its high brightness and photostability under excitation and depletion. This dye has been previously demonstrated to achieve a spatial resolution as low as 25 nm [179].

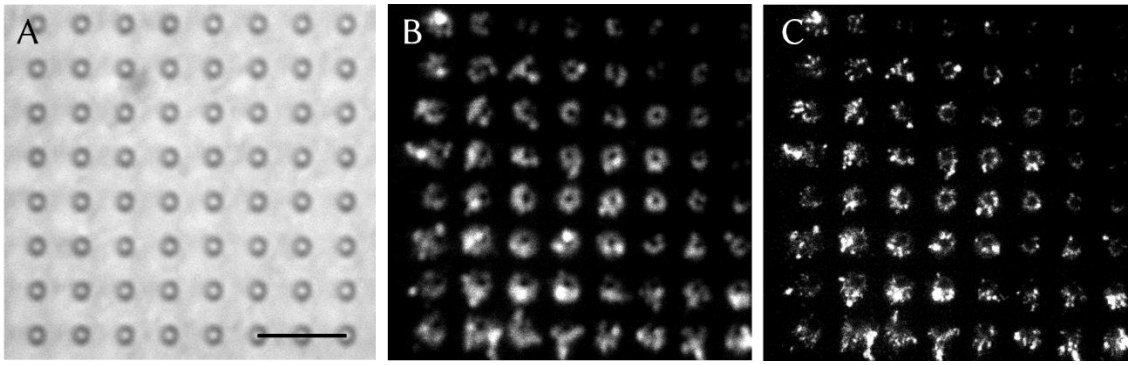

Figure 4-15 Microscopic images of immobilized antibodies. All images were taken from the same lower left corner of a nanoelectrode array. Antibodies from abberior labeled with STAR RED were used. (A) Bright field image. 100x objective (NA = 1.40). Scale bar: 5 µm. (B) Confocal microscopy image. 100x objective (NA = 1.45), pinhole: 64 µm, excitation laser: 640 nm (10%), line accumulation: 1. (C) STED image. Depletion laser: 775 nm (20%), line accumulation: 1.

Due to the STED microscopy high resolution images of the immobilized antibodies with a resolution of about 100 nm were acquired directly without the need to deconvolve the images. Figure 4-15 displays the lower left corner of a nanoelectrode array. Looking at the entire array, a

gradient similar to that of the X-31 from chapter 4.3.1 occurs. The same applies to the spatial distribution on the individual electrode level. Here, too, the immobilization clearly is focused at the electrode edge. Due to fluid flow coming from beneath as well as from the left there is a pronounced accumulation of the viral material on the bottom left side of the electrodes. The permanent sticking to the electrodes facilitates chip handling for the upcoming experiments.

4.4.2.2 R18 – staining, purification, ELISA

As demonstrated in chapter 4.4.1.1 labeling of the X-31 surface proteins is one of the causes that prevents the anti-H3 antibodies to recognize their epitope. Consequently, the viral material had not been labeled for the on-chip studies from chapter 4.4.1. Instead, the on-chip antibody-antigen interaction was monitored via a fluorescently labeled secondary antibody. When it comes to the second approach of the on-chip immunoassay the antibodies should now serve as a bio-receptor and bind and detect viruses from the sample. Binding should be measured directly. Again, the antibodies were not stained for this, but the viruses had to be. Therefore, octadecyl rhodamine B (R18), a lipophilic dye that non-covalently stains the viral membrane, was chosen. Its long, lipophilic alkyl tail comprising 18 C-atoms integrates into the membrane while the fluorophore remains at the virus surface. If R18 is present at high concentrations its fluorescence gets quenched. A property that is, among others, used for kinetics of membrane fusion between viruses and their host cells [180, 181]. Therefore, R18 concentration had to be chosen carefully to optimize fluorescence output.

In order to remove the unbound dye several purification methods were applied to a virus-free 1 µM R18 solution in PBS: (I) ultrafiltration spin columns, (II) centrifugation and (III) gel filtration. (I) When it comes to the ultrafiltration ideally the free dye should pass the filter and collect as the filtrate, while the concentrate should be dye-free. As illustrated in Figure 4-16A that did not work. The R18 remained in the concentrate. Due to its hydrophobic character the dye seems to form micelles with a diameter too large for the filter. Under the given conditions this is not a suitable technique. (II) The second approach was to remove the free dye by centrifugation. Ideally, the viral sample should collect as a pellet and the free dye remains in the supernatant due to the different densities of both. Here, the centrifugation of the virus-free R18 solution for 50 min at 16.000 g resulted in the migration of the dye into the pellet, while the supernatant became dye-free (Figure 4-16B). Thus, under these settings a separation is not possible. (III) Last but not least, a separation

by gel filtration was successfully carried out. As depicted in Figure 4-16C the free dye was removed by gel filtration, thus the fluorescent objects in Figure 4-16C.2 are R18-stained virus particles.

In the end, with optimal conditions all methods have the potential of being successful. An ultrafiltration filter with a bigger MWCO or different centrifugation settings (centrifugal force and time) might have led to a successful purification. This was not pursued further due to the effective purification by gel filtration.

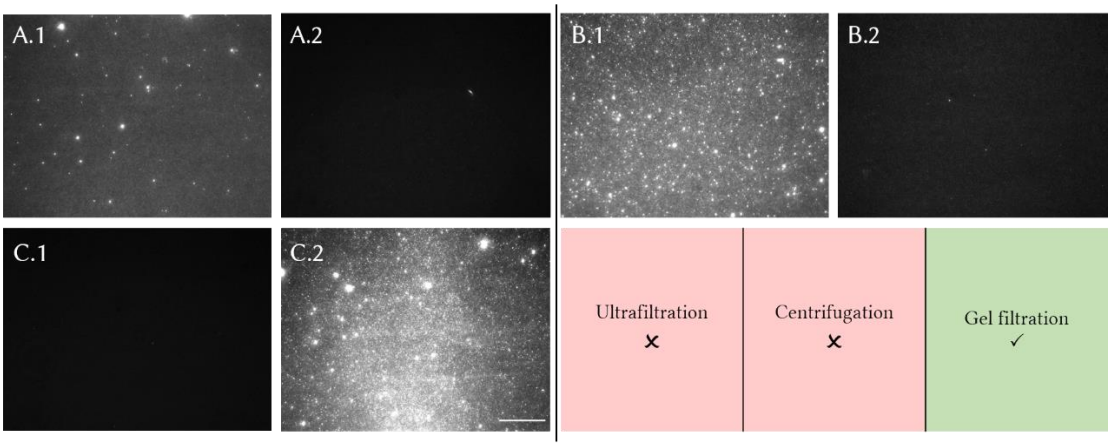

Figure 4-16 Removal of unbound R18 dye. Three different purification methods were tested to remove the free R18 dye. (A) Ultrafiltration: R18 remained in the concentrate (A.1) and did not collect in the filtrate (A.2). (B) Centrifugation: under the given settings R18 unfortunately collected as a pellet (B.1) and did not remain in the supernatant (B.2). (C) Gel filtration: the R18 dye was successfully retained, resulting in an R18-free filtrate (C.1). C.2 shows the filtrate of an R18-dyed X-31 sample. Cy3 filter, 40x objective, exposure time: 500 ms, all fluorescence images with the same contrast settings, scale bar: 50 µm.

The impact of the R18 staining on the interaction between anti-H3 and X-31 was examined by ELISA. Therefore, wells were coated with a freshly stained X-31 sample as well as with a sample stained a week before. As a reference served a freshly prepared, untreated, unstained X-31 sample diluted in PBS. The staining led to an absorption reduction of the ELISA signal of about 40% as compared the reference value. A week old stained sample further reduced the interaction leading to a loss of about 75% as compared to the reference. In summary, the antibody still recognizes its epitope after the R18 staining, but for on-chip experiments the staining should be done immediately before the experiment.

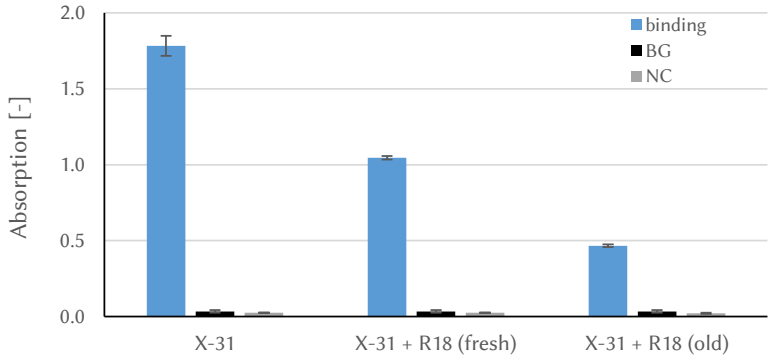

Figure 4-17 Influence of R18 on the antibody-antigen interaction - ELISA. The influence of the R18 staining on the interaction between anti-H3 and X-31 was examined by ELISA. Therefore, a freshly stained sample (X-31 + R18 fresh) and a one week old stained sample (X-31 + R18 old) were analyzed and compared to the reference (X-31).

4.4.2.3 Electrode chip passivation

The chip passivation has already been described and analyzed in chapter 4.4.1.2. There, it was necessary to prevent the non-specific binding of antibodies to the electrode chip. This series of experiments had to be repeated to determine the best blocking solution which prevents the non-specific binding of R18 labeled X-31 to the chip surface.

Again, chips were passivated with different blocking solutions: 3% BSA, 2% MP, 1% PEG600, 1% PEG20k. Subsequently, those chips were exposed to an R18 labeled X-31 solution that was diluted in the same blocking solution. Fluorescence intensity of nonspecific sticking X-31 was measured by fluorescence microscopy with a 60x objective (NA = 0.7), a Cy3 filter, a 550 nm LED as illumination source at 100% intensity and an exposure time of 2 s. The fluorescence intensity of a 1.75 μm^2 SiO_2 area and of 49 electrodes were measured as described in chapter 4.4.1.2. BG-corrected values are plotted in Figure 4-18A.

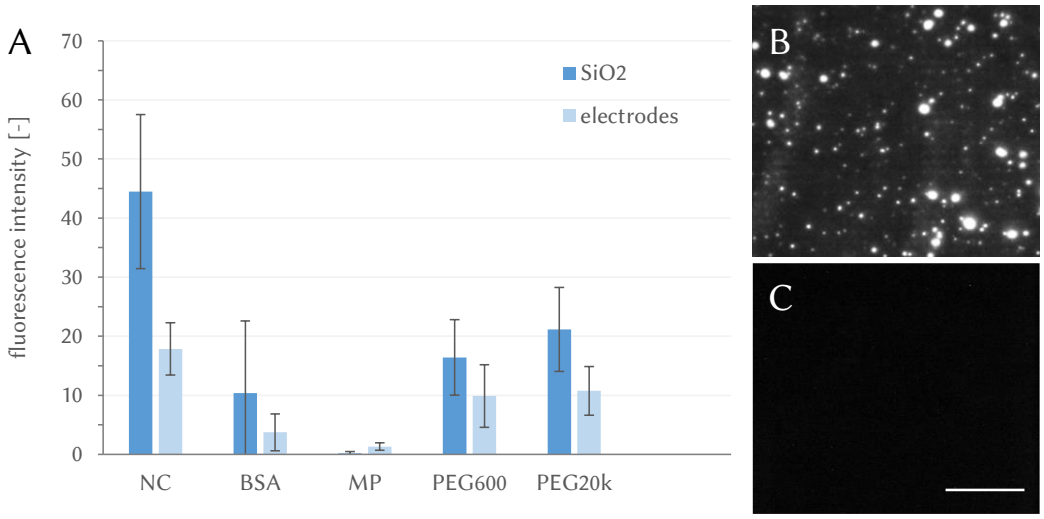

Figure 4-18 Chip passivation to prevent nonspecific binding of R18 labeled influenza virus material. (A) Different blocking solutions were tested: 3% BSA, 2% MP, 1% PEG600 and 1% PEG20k. The NC was a non-passivated chip. All values are BG-corrected. (B) and (C) are fluorescence images of the NC and a chip passivated with 2% MP, respectively. 60x objective (NA = 0.7), Cy3 filter, 550 nm LED, exposure time: 2 s, all fluorescence images have same contrast settings. NC: negative control; MP: milk powder. Scale bar: 20 µm.

Again, all blocking solutions decrease the BG signal by preventing, at least parts of, the R18 labeled X-31 from sticking to the surface. When comparing the fluorescence images of the NC from Figure 4-13B and Figure 4-18B, it is evident that the secondary antibody produces a more uniform BG signal than the non-vortexed R18 labeled X-31. The latter aggregates in different sizes, which explains the high standard deviations compared to Figure 4-13A. With a reduction of approximately 77%, even the 3% BSA passivated chip still shows a significant BG signal. Since the non-specific sticking of R18 labeled X-31 appears in spots, such a non-specific sticking of R18 labeled X-31 can be misinterpreted as a positive signal. Therefore, it is even more important to keep the BG as low as possible. As a result, 2% MP was chosen as the blocking solution for the on-chip immunoassay experiments with X-31 as the analyte.

4.4.2.4 On-chip experiments

As before, a potential on-chip immunoassay was tested. This time the arrangement of X-31 and anti-H3 was inverted: Anti-H3 was permanently immobilized onto the nanoelectrodes serving as the bio-receptor while X-31 was used as the analyte.

The preliminary experiments showed that the antibody permanently sticks to the electrode edge, similar to the immobilization of X-31. To measure the interaction between anti-H3 and X-31 the viral sample was stained with R18. Based on ELISA results the staining of X-31 was always done immediately before the on-chip experiment. A fresh dilution of anti-H3 was prepared in ultrapure water just before each experiment. The antibodies were immobilized at 15 kHz and a voltage of 5.3, 3.5 or 1.8 V_{rms} for 10 min on separate chips. Based on the passivation studies (4.4.2.3) the chip was passivated with 2% MP, and blocking as well as dilution of X-31 were performed with 2% MP as well. Finally, the functionalized chips were incubated with X-31 (details written in 3.12.4).

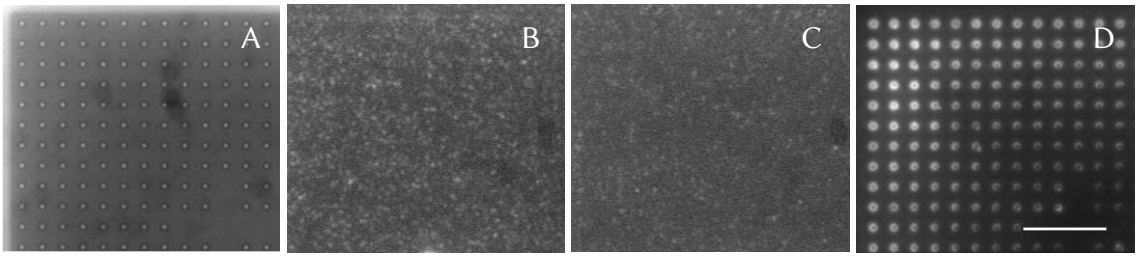

Figure 4-19 On-chip immunoassay – approach 2. (A) Bright field image of the upper left corner of an electrode array. (B) The same area after non-labeled anti-H3 was immobilized at 15 kHz and 5.3 V_{rms} for 10 min and incubation with R18 labeled X-31 was done. The image is representative also for the chips that were functionalized at 3.5 and 1.8 V_{rms}. (C) NC: Instead of immobilizing anti-H3 by ACEK the chip was just incubated with the antibody sample. (D) The same area after incubation with a secondary antibody to prove the presence of immobilized anti-H3. Fluorescence images (B, C): 100x objective (NA = 1.40); Cy3 filter; exposure time: 5 s; LED: 550 nm. Fluorescence image (D): 100x objective (NA = 1.40); WIBA filter; exposure time: 5 s; LED: 490 nm. Image A and B have the same contrast settings. Scale bar: 10 µm.

The functionalization of individual chips by either 5.3, 3.5 or 1.8 V_{rms} was done to lead to a decreasing temperature development as well as decreasing forces by ACEK effects to might reach more gentle settings for antibody immobilization. If the temperature is too high or the ACEK forces are too strong this might cause antibodies to denature. Unfortunately, for all three voltages no binding of anti-H3 to X-31 was measurable. Here, Figure 4-19B shows the upper left corner of a

functionalized (5.3 V_{rms}) electrode array after X-31 incubation. It is representative for all three voltages. The existence of immobilized anti-H3 was proven by incubating all chips with a secondary antibody binding to anti-H3 (Figure 4-19D).

Altogether, the feasibility of an on-chip immunoassay with anti-H3 as the bio-receptor and X-31 as the analyte could not been demonstrated. Several causes are possible for this. Reasons for the missing antigen-antibody interaction might arise from the denaturation of the antibody due to too strong heat development at the electrodes, too strong ACEK forces acting on the antibodies or the contact with the metal surface. Furthermore, antibodies might have been wrongly orientated with their paratope facing the electrodes. A detailed discussion will be given in 4.4.3.

4.4.3 Discussion

In the course of the work most sources of uncertainty could be eliminated which allowed to successfully bind the anti-H3 antibody to immobilized X-31 influenza virions. As a consequence of minimized vortexing, most virus particles were not immobilized as singles but in aggregates. A successful result for approach 2 could not be achieved despite testing various electrode voltages. Binding could be measured in the ELISA that was missing on the chip. Reasons for this are manifold.

There is a relatively small number of studies investigating the effect of electric fields on the protein structure [113–117]. Basically, two interaction mechanisms are discussed: forces created by electric field stress (I) and frictional forces causing proteins to unfold (II). (I) Budi *et al.* studied the conformation change of insulin Chain-B by molecular dynamic simulations with either an oscillating electric field at 2.45 GHz or static fields, both ranging from 10^7 V/m to 10^9 V/m [116]. They came to realize that both variations had an influence on the protein conformation. However, as compared to the static case the oscillating fields were more disruptive causing severe disruption of the secondary structures at $5*10^8$ V/m and above [116]. Another study based on molecular dynamic simulations was performed by della Valle *et al.* to calculate the effects of electric fields of 10^8-$7*10^8$ V/m on the conformation of the enzyme superoxide dismutase (SOD-1). They demonstrated, with increasing field strength, first an influence on the active site, to partially denatured proteins, to a complete unfolded state at the strongest electric field strength [114]. Furthermore, Zhao and Yang performed an experimental determination by circular dichroism analysis and micro-Raman spectroscopy [115]. They subjected lysozyme in solution to a pulsed electric field of $3.5*10^6$ V/m. They observed a conformational change in the secondary structure as well as in the disulfide bonds leading to destabilization of the protein and a decrease in activity. However, pulse duration was 2.5 µs, which corresponds to a frequency of 400 kHz, which is much higher than our sinusoidal-field frequency of 15 kHz [115]. (II) Further studies focus on the structural change due to frictional forces. In their study, Bekard and Dunstan demonstrated that BSA and Lysozyme were unfolded when exposed to an oscillating electric field with field strengths from 78 V/m to 500 V/m with a frequency of 10 or 500 Hz [117]. However, they explain that even forces, created by the strongest electric field of 500 V/m, are five orders of magnitude too small to break the inter-chain bonding forces, here especially the H-bonding in α-helices and β-sheets. This means, based on their studies, field strengths of about $5*10^7$ V/m are needed to break the H-bonds.

They argue, that denaturation originates in the frictional energy dissipation [117]. With a calculated field strength of $1.1*10^6$ V/m for the antibody immobilization at the cylindrical nanoelectrodes at 5.3 V_{rms} the present study is well below this threshold. Thus, the movement to the electrodes, as well as the fluid streaming above the electrodes creates friction that might induce an unfolding of the antibodies.

There is only one publication investigating the conformational change of antibodies in electric fields [113]. Antibodies were immobilized on an electrode surface by coupling it to an interlayer made of His-tagged protein A, thus creating a uniform orientation with the paratope facing the sample's volume. They demonstrated a change in conformation by electrostatically pushing and pulling the antibody's recognition site towards or from the electrode surface. This modulated the antibody's affinity. Thus, a positive potential of 100 mV pushed the recognition site towards the solution volume, increasing the capture efficiency. While a negative potential of -100 mV pulled the recognition site towards the electrodes. The arising steric hindrance decreased the capture efficiency. An irreversible structural change leading to the inactivation of antibodies due to an electric field has not been reported.

However, due to the lack of comparability of the presented studies with the present thesis, including different frequencies, different measurement setups, different proteins, the literature can only be used as a guidance. The electric field might have an influence on the antibodies either by frictional forces or by electric field stress, but the extent remains unclear.

The activity of different enzymes after ACEK immobilization was studied by Prüfer *et al.* [71, 108]. Horseradish peroxidase [108], glucose oxidase [71] or choline oxidase (unpublished) were immobilized on titanium nitride rings with a diameter of 500 nm, a width of 20 nm at 10 kHz and 7 V_{rms}. Activity measurements of the immobilized enzymes resulted in large differences. While the horseradish peroxidase showed an activity of up to 45% this was dropped to 1.3% for the glucose oxidase and no activity was detectable for the choline oxidase. Demonstrating that even with the same electrode setup and electric field settings different proteins are affected differently. They argue that the causes might be due to conformational changes of the enzymes due to the electric field, the interactions with the electrodes or different amounts of immobilized enzymes.

In their study Otto *et al.* claimed to have reached the successful immobilization of anti-RPE (R-phycoerythrin) antibodies while keeping its functionality [106]. Therefore, they used electrodes

of similar type as the ones used in the present thesis: tungsten nanoelectrodes, cylindrical shaped with a diameter of 900 nm. The non-labeled anti-RPE was immobilized at 100 kHz, 18 V_{rms} for 20 min. A subsequent incubation with R-phycoerythrin (RPE) lead to a localized fluorescence at the electrodes, which was argued to be the proof of the preserved activity of the immobilized antibodies. In a control with just an RPE incubation without antibodies and without an electric field no fluorescence change at the electrodes was measured, showing that RPE does not bind non-specifically to the electrodes. However, it was not demonstrated that the interaction between RPE and anti-RPE after the immobilization was really specific. The immobilized anti-RPE might have lost its conformation and thus its binding activity. Hence, it might be possible that the fluorescence signal was due to non-specific binding of RPE to the coated electrodes, and not the result of a specific antigen-antibody interaction. Thus, the interpretation by Otto *et al.* should be reconsidered.

Furthermore, applying an electric field causes heat generation at the electrodes. If the temperature is too high it can cause an unfolding of the antibodies. The temperature development during an applied electric field was studied by Otto *et al.* [106]. To this end, they filled the sample chamber of a nanoelectrode chip with a 1 mM solution of rhodamine B, a temperature sensitive dye. A rise in temperature resulted in a loss of fluorescence intensity. They applied electric fields of 100 kHz and 500 kHz and voltages between 14 and 21 V_{rms} for up to 15 min. They measured a 3.5-fold decrease of fluorescence intensity from 500 kHz to 100 kHz and a 1.8-fold decrease from 21 V_{rms} to 14 V_{rms} (at 100 kHz). Thus, the lower the frequency and the applied voltage, the smaller the temperature rise. For a frequency of 100 kHz and an applied voltage of 14 V_{rms} a temperature increase of 10°C was measured. In this thesis a 6.5-fold lower frequency and at least 2.5-fold lower voltage was applied for the immobilization of antibodies. Therefore, an even lower temperature rise at the electrodes is expected, too small to cause denaturation.

One more reason for the non-measurable antibody-antigen interaction might be the orientation of the immobilized antibodies. A uniform orientation of the antibody with their paratope facing into the volume, thus being accessible for the antigen, can lead to an enhanced capture efficiency compared to immunoassays with randomly orientated antibodies like ELISA. Such an orientation without an electric field can be achieved, for example, by surface modification and site-specific antibody modification [182] or charged surfaces [183]. It was demonstrated that antibodies can be orientated in electric fields with their longitudinal axis parallel to the electric

field [6, 184, 185]. Transferring this to the cylindrical nanoelectrodes, the antibodies should be oriented perpendicular to the electrode surface. However, it remains unclear whether the active site of the antibodies faces into the volume ("tail-on") or to the electrode surface ("head-on"). The non-existing binding signal might be a hint for the unwanted orientation towards the surface.

Additional aspects to be considered, that might have a negative influence on the antibody stability, include interactions with the tungsten electrode and storage in water during ACEK immobilization. Above that, publications dealing with the influence of electric fields on proteins usually consider the strength $|\vec{E}|$ of the electric field, but not its gradient. Since the latter is very high at the electrode edge this might have a hitherto unknown impact on the antibody structure. Furthermore, the affinity between X-31 and anti-H3 might be insufficient, resulting in X-31 binding to the antibodies but being rinsed away in the subsequent washing step, before fluorescence measurement of the chip. Moreover, the load density of antibodies at the electrodes might be too high, leading to steric hindrance among the antibodies. Nonetheless, the existing gradient of immobilized antibody concentration should allow for an optimal density, theoretically enabling antibody-antigen interactions starting from an inner row. However, this observation has not been made thus far.

Due to its different structure and size the presented forces and effects have a different impact on the viral material. As a consequence of the spherical symmetry and of the overall coverage with hemagglutinin there can be no misorientation in the electric field. Regardless of the virus particles' orientation at the electrodes, parts of the surface proteins will always face into the volume, allowing accessibility for the anti-H3 antibody. Unlike the case of antibodies, temperature changes occurring at the electrode or the interactions at metallic contact are not so critical. Although viral surface proteins in contact with the electrodes might be denaturized, the spherical shape of the virus particle itself creates a separation between the electrodes and other surface proteins, protecting these from denaturation, be it by temperature, surface interaction or the electric field itself.

When it comes to the ACEK immobilization of antibodies some of these negative influences could be reduced by decreasing the applied voltage from 5.3 to 3.5 to 1.8 V_{rms}. By reducing the voltage heat production is reduced as well as the strength of the fluid motion above the electrodes, forces acting on the antibodies are lessened. However, even with the lowest voltage of 1.8 V_{rms}, the immobilization is still not gentle enough or a different cause has to be considered. Thus, the

immobilization of antibodies to the nanoelectrodes by ACEK effects still requires optimization in terms of stability and activity.

5 Summary and outlook

In the present thesis, ACEK forces, like DEP and ACEO, have been demonstrated as a simple and fast method to immobilize influenza viruses or anti-influenza antibodies. It is a promising alternative to the established challenging and complex methods for the surface modification of biosensors. The submicron size of the virus particles and antibodies poses a significant challenge compared to the already established manipulation of cells.

At first a closer look has been taken at the temporal development of the immobilization of the influenza viruses being about 100 nm in size. Attraction of the viral material when applying the AC electric field (20 kHz, 3.5 V_{rms}) happens within seconds. It has been demonstrated that the temporal development of the accumulation at the nanoelectrodes shows an exponential correlation, a saturation curve, corresponding to equation (4). The emerging saturation does not have its origin in the sample depletion but in the maximum capacity of material that can accumulate on an electrode. This capacity is determined, among others, by the degree of the electric field gradient. Furthermore, the point in time at which the saturation occurs and the degree of it are location-dependent. This results in an inhomogeneous distribution of the immobilized material. A gradient exists with decreasing concentration from the outer row towards the inner ones. The complex interplay of different forces that lead to this gradient have been illustrated in detail. On the one hand, the reduced competition with neighboring electrodes and the overall stronger electric field gradient at the edge of the electrode array explain the stronger accumulation at the outermost row. On the other hand, polarizable particle in an AC electric field are exposed to a variety of forces, not just DEP, the force that draws the viruses to the electrode edges. Thus, ACEO and electrothermal fluid flow create a vortex shaped fluid motion above the electrode array. This motion creates a viscous drag on the viral material. Consequently, the electrodes are provided with more material from the sample volume, while the drag force competes with the DEP force. The behavior of fluid flow depends on factors such as the applied voltage, frequency, conductivity, permittivity, and electrode design. Therefore, a pure DEP immobilization cannot be assumed, but an interplay of different forces. Forces whose influence increases as the object size decreases. The benefit of this fluid motion has been illustrated as well as different ways to get to the bottom of the cause of these side effects or ways to reduce them.

One of the outstanding features of the presented experimental setup is the permanent immobilization without the requiring any prior chemical modification of the surface or the

bio-receptor. Although the DEP-induced accumulation usually is reversible, this study has successfully demonstrated the permanent immobilization of viral materials onto the nanoelectrodes. Consequently, it becomes possible to subsequently handling the functionalized chips without the electrical setup. Further experiments have been introduced that will be necessary in order to better understand the interactions between the electrode surface and the immobilized sample.

Fluorescence microscopy and image processing by deconvolution have been combined to overcome parts of the limitation of the optical resolution. Thus, the individual distribution of the permanent immobilized viral material on each electrode could be elucidated. The sum of this individual distribution reveals a major accumulation of viral material at the electrode edge, the site with the strongest electric field gradient $\nabla|E|^2$. Parts of the viral material are carried to the electrode surface by ACEO.

Thus, the use of ACEK forces is a simple and fast method to permanently functionalize the surface of electrodes with submicrometer sized objects. A large number of possible applications have been illustrated. Experimentally, the suitability of the immobilization technique has been tested for a potential affinity-based biosensor with either influenza as the bio-receptor or the analyte.

For these on-chip immunoassays a series of preliminary tests have been carried out. Through indirect ELISA and indirect FLISA a few sources of disturbance for the interaction between the influenza virus and the anti-H3 antibody could be identified and minimized or eliminated. E.g., the labeling of viral proteins by a succinimidyl-ester of DY-634 prevents the antigen-antibody interaction. Optimization of the protocol could have resulted in successful staining while retaining the binding ability, but was not pursued further. Instead, the staining was omitted completely (approach 1) or replaced by membrane staining with R18 (approach 2). Furthermore, based on the ELISA results, the vortexing of the viral material and the storage in ultrapure water, either of the influenza virus sample or the antibody, has been kept as short as possible as it destroys or diminishes the antigen-antibody bond.

Different blocking solutions have been tested to minimize the non-specific binding to the surface of the chip. To prevent the primary and secondary antibody from randomly sticking best results have been achieved with 3% BSA. To prevent the non-specific binding of the R18-labeled influenza virus the best choice was 2% MP.

When it comes to the on-chip immunoassay experiments the feasibility with influenza (X-31) as the bio-receptor has been demonstrated (approach 1). Non-labeled X-31 has been immobilized by ACEK effects. The subsequent incubation with the anti-H3 antibody and, for visualization, secondary antibody was successful. A binding-interaction on-chip was measureable. The uneven signal distribution is based on the uneven immobilization of the X-31 and the minimized vortexing. The negative controls demonstrate that the signal is not due to unspecific adsorption but due to specific interaction between X-31 and anti-H3.

For approach 2 the arrangement has been changed. Here, the anti-H3 antibody served as the bio-receptor. Beforehand, the spatial distribution of the antibodies immobilized by ACEK on the nanoelectrodes was observed using a STED microscope. Thanks to the high resolution of the STED of around 100 nm, no deconvolution was necessary for the evaluation. The distribution was similar to that of the immobilized viruses: the majority of the permanently immobilized antibodies are located at the electrode edge, a gradient with decreasing concentration runs from the outer to the inner ones. Unfortunately, no binding of the X-31 virus to the immobilized anti-H3 antibody has been detected. A decrease of the immobilization voltage from 5.3 to 1.8 V_{rms}, and thus applying more gentle settings, did not change the result. A secondary antibody subsequently proved the existence of immobilized anti-H3 antibody at the nanoelectrodes.

Reasons for the missing activity of the immobilized antibodies can be manifold. There is not much literature about the influence of the electric field onto the conformation and activity of proteins [113–117]. Here a differentiation can be made between conformational change due to the electric field stress or due to internal frictional forces. A large part of the results is based on molecular dynamics simulations [114, 116] and not experimental studies [113, 115, 117]. The knowledge about the influence of the electric field onto the conformation and activity of antibodies is even scarcer [106, 113]. There is one study demonstrating the conformational change of immobilized antibodies in an electric field while keeping its activity [113]. However, the voltages applied to those immobilized antibodies were very small (100 mV) and the antibodies were not immobilized by ACEK forces but bound to a protein A-modified surface. On the other hand, Otto *et al.* have immobilized anti-RPE antibodies under harsher conditions (100 kHz, 18 V_{rms} for 20 min) than the anti-H3 antibodies immobilized (15 kHz, 1.8 to 5.3 V_{rms} for 10 min) in the present thesis [106]. Still, a localized fluorescence at the electrodes was measured, which was argued to be the proof of the preserved activity of these antibodies. Due to missing controls that

verify the specificity of this binding these results should be taken with care. Thus a conformational change of the anti H3-antibodies from the present study due to the electric field and thus losing its activity is plausible. To avoid this loss of activity, settings should be optimized for gentler immobilization, settings that mitigate the electric field stress or the frictional forces, such as lower voltage and different frequencies. Another option is not to immobilize the antibodies directly by ACEK to the nanoelectrodes, but rather use an intermediate layer. The substance, of which the intermediate layer is made, must be robust against the influence of the electric field as it is created by the AC electrokinetic immobilization. Such a substance could be protein A or G as it binds the Fc region of antibodies. Thus, the antibodies would not be exposed to the electric field, there would be no direct contact to the metallic surface, they could remain in buffer and would be getting aligned with the active side protruding into the sample volume. On the other hand, the stability of protein A and G towards the influence due to an electric field has not been determined yet and the creation of such an intermediate layer would mean an additional step in the chip preparation.

Furthermore, it was shown earlier that molecules are getting aligned in the electric field [6]. If there is an unfavorable orientation of the immobilized antibodies, this can diminish or cancel the activity. By means of antibody modification, e.g. coupling with another protein, the induced dipole could be changed in such a way that a preferred alignment in the electric field is reached. Other illustrated aspects to be considered are the interaction with the tungsten surface, the storage in water and the electric field gradient. An unfolding due to an excessive temperature increase at the electrodes can be excluded based on the literature that illustrates a maximum temperature increase of 10 K [56, 106]. Due to their size and spherical symmetry, some of these influences have less or no impact on the virus material or the viral surface proteins.

From the AC electrokinetic point of view the analyte samples used in the present thesis present ideal conditions as they comprise just the analyte in ultrapure water. Patient's sample are complex as they usually are blood or saliva samples. Thus, a sample preparation might be needed. Here, again ACEK forces can come into play. Thus, Cai *et al.* have demonstrated the isolation of different pathogens from whole human blood samples by DEP [186]. Therefore, the blood sample was diluted to a conductivity of about 150 µS/cm and was added to IDEs integrated into a microfluidic system. By applying an electric field of 20 V_{pp} at 200 MHz the pathogens were attracted to the IDEs by pDEP and the blood cells were repelled by nDEP and flushed to the outlet. When it comes to the influenza diagnostics blood or saliva samples are analyzed as well. So such a sample

preparation might be possible with the presented nanoelectrode setup when combined with microfluidics. A suitable range of frequencies and voltages must be determined beforehand so that the analyte (virus or antibodies) can be separated from the rest of the sample, is getting into close proximity to the bio-receptor and is immobilized on the electrodes only temporary.

Furthermore, in common immunoassays the receptor interacts with the analyte in its spatial proximity. A supply of more analyte material is based on diffusion and Brownian motion. This slows down the process because long incubation times are needed, hampering a rapid detection. Appling an AC electric field during analyte incubation breaks the diffusion limitation (either by dielectrophoretic attraction or by fluid flow) and reduces the assay time and can increase the sensitivity [34, 187].

So far, only qualitative statements are possible. In future development steps, the feasibility of a quantitative measurement should be examined. In this context, the system should be characterized in terms of its detection limit, sensitivity and specificity.

It is possible to further simplify the presented setup and to achieve a faster detection. The optical readout by fluorescence microscopy is complex, expensive and slow. This can be optimized by changing to an electrical readout. The change in the impedance of the system is a measure of the binding interaction between bio-receptor and analyte. This change can be measured directly via the change in impedance or indirectly via the change in the resonant frequency [188, 189]. The change to an electrical read-out eliminates the labeling (I) and some of the incubation steps (II). (I) For an optical readout the analyte must be stained either directly or indirectly. Both cases were represented in approaches 1 and 2 of this work. While the antibodies were made visible using a secondary antibody (approach 1), the viruses were stained directly with R18 (approach 2). (II) As the immobilization of viruses or antibodies is done within seconds to few minutes the subsequent incubations steps lasted up to 1 h each. An electrical readout allows for a label-free detection e.g. based on the presented impedance measurement. Thus, less preparation steps and incubation steps are needed. Direct measurement of the antigen-antibody interaction is possible and response times of only 30 s have been demonstrated [34].

The number of arrays can be scaled up as well as the number of different analytes (pathogens or antibodies) that can be measured with such a chip. Together with a microfluidic system and an electrical read-out, this nanoelectrode chip can be combined into a lab-on-a-chip (LOC) system

that works quickly, inexpensively and in a space-saving manner. Such a system would be portable and compatible with point-of-care (POC) diagnostics to reach places that are difficult to reach or places with poor laboratory/medical facilities. These POCs would be convenient to perform and would not require especially skilled personnel.

All in all, the simple and fast modification of the surface of nanoelectrodes with submicrometer sized objects like X-31 or anti-H3 antibodies has been demonstrated exploiting ACEK effects. No sophisticated and time-consuming procedures are needed, as is usual for common surface modification methods like SAM. For the presented modification method, the bio-receptor does not have to be chemically modified either. The permanent immobilization allows for a subsequent handling of the nanoelectrode-chip without the electrical setup. Due to the directed attraction to the electrodes, as well as the fluid motion that carries more material from the volume to the vicinity of the electrodes, working with small volumes and at low concentrations is feasible. This is what makes this method also attractive for rare and expensive samples, regarding the receptor as well as the analyte. While the detection of antibodies by the immobilized viral material was successful, the detection of viruses was not. The latter is probably due to the lost activity of the immobilized antibodies or its wrong orientation. Further studies on the maintenance of activity and orientation must follow. Once functionalized, the chips are easy to handle and - combined with microfluidics and an electrical read-out - have the potential for a rapid, portable and inexpensive POC device that is the starting point for various applications in the diagnostics and therapy of influenza as well as of various other pathogens.

References

1 World Health Organization. *WHO launches new global influenza strategy*. https://www.who.int/news-room/detail/11-03-2019-who-launches-new-global-influenza-strategy (accessed June 9th 2023).

2 Lessler J, Reich NG, Brookmeyer R, Perl TM, Nelson KE, Cummings DAT. *Incubation periods of acute respiratory viral infections: a systematic review*. The Lancet. Infectious diseases. 2009, 9 (5), 291–300. doi: 10.1016/S1473-3099(09)70069-6.

3 Lehnert R, Pletz M, Reuss A, Schaberg T. *Antiviral Medications in Seasonal and Pandemic Influenza*. Deutsches Arzteblatt international. 2016, 113 (47), 799–807. doi: 10.3238/arztebl.2016.0799.

4 Robert Koch-Institut. 2013. *Monitoring des Managements von Ausbrüchen durch respiratorische Erreger in Pflegeeinrichtungen: Checkliste für die Gesundheitsämter (GÄ) und/oder Pflegeeinrichtungen*. https://www.rki.de/DE/Content/InfAZ/I/Influenza/IPV/Checkliste_Respiratorischer_Ausbruch.html (23rd June 2023).

5 Merckx J, Wali R, Schiller I, Caya C, Gore GC, Chartrand C, Dendukuri N, Papenburg J. *Diagnostic Accuracy of Novel and Traditional Rapid Tests for Influenza Infection Compared With Reverse Transcriptase Polymerase Chain Reaction: A Systematic Review and Meta-analysis*. Annals of internal medicine. 2017, 167 (6), 394–409. doi: 10.7326/M17-0848.

6 Laux E-M, Knigge X, Bier FF, Wenger C, Hölzel R. *Aligned Immobilization of Proteins Using AC Electric Fields*. Small (Weinheim an der Bergstrasse, Germany). 2016, 12 (11), 1514–1520. doi: 10.1002/smll.201503052.

7 Te Velthuis AJW and Fodor E. *Influenza virus RNA polymerase: insights into the mechanisms of viral RNA synthesis*. Nature reviews. Microbiology. 2016, 14 (8), 479–493. doi: 10.1038/nrmicro.2016.87.

8 CDC. *Types of Influenza Viruses*. https://www.cdc.gov/flu/about/viruses/types.htm (accessed June 8th 2023).

9 Harris A, Cardone G, Winkler DC, Heymann JB, Brecher M, White JM, Steven AC. *Influenza virus pleiomorphy characterized by cryoelectron tomography*. Proceedings of the National Academy of Sciences of the United States of America. 2006, 103 (50), 19123–19127. doi: 10.1073/pnas.0607614103.

10 Oxford JS, Corcoran T, Hugentobler AL. *Quantitative analysis of the protein composition of influenza A and B viruses using high resolution SDS polyacrylamide gels*. Journal of biological standardization. 1981, 9 (4), 483–491. doi: 10.1016/S0092-1157(81)80041-8.

11 Stanke S, Wenger C, Bier FF, Hölzel R. *AC electrokinetic immobilization of influenza virus*. ELECTROPHORESIS. 2022, 43 (12), 1309–1321. doi: 10.1002/elps.202100324.

12 Bragstad K, Nielsen LP, Fomsgaard A. *The evolution of human influenza A viruses from 1999 to 2006: a complete genome study*. Virology journal. 2008, 5, 40. doi: 10.1186/1743-422X-5-40.

13 Scholtissek C. *Source for influenza pandemics*. European journal of epidemiology. 1994, 10 (4), 455–458. doi: 10.1007/BF01719674.

14 Saunders-Hastings PR and Krewski D. *Reviewing the History of Pandemic Influenza: Understanding Patterns of Emergence and Transmission*. Pathogens (Basel, Switzerland). 2016, 5 (4). doi: 10.3390/pathogens5040066.

15 World Health Organization. 2017. *Pandemic Influenza Risk Management: A WHO guide to inform and harmonize national and international pandemic preparedness and response*. https://apps.who.int/iris/handle/10665/259893 (accessed June 9th 2023), page 26.

16 Robert Koch-Institut. AGI -Studiengruppe. 2020. *Influenza-Monatsbericht: Kalenderwochen 37 bis 39 (5.9. bis 25.9.2020)*. https://influenza.rki.de/Wochenberichte/2019_2020/2020-39.pdf (accessed June 9th 2023), page 5.

17 Robert Koch-Institut. AGI -Studiengruppe. 2021. *Influenza-Wochenbericht: Kalenderwoche 20 (15.5. bis 21.5.2021)*. https://influenza.rki.de/Wochenberichte/2020_2021/2021-20.pdf (accessed June 9th 2023), page 6.

18 Robert Koch-Institut. AGI -Studiengruppe. 2022. *ARE-Wochenbericht: Kalenderwoche 39 (26.9. bis 2.10.2022)*. https://influenza.rki.de/Wochenberichte/2021_2022/2022-39.pdf (accessed June 9th 2023), page 5.

19 Robert Koch-Institut. AGI -Studiengruppe. 2023. *ARE-Wochenbericht: Kalenderwoche 21 (22.5. bis 28.5.2023)*. https://influenza.rki.de/Wochenberichte/2022_2023/2023-21.pdf (accessed June 9th 2023), page 5.

20 Killingley B and Nguyen-Van-Tam J. *Routes of influenza transmission*. Influenza and other respiratory viruses. 2013, 7 Suppl 2 (Suppl 2), 42–51. doi: 10.1111/irv.12080.

21 Jilani TN, Jamil RT, Siddiqui AH. *H1N1 Influenza*, StatPearls Publishing, Treasure Island (FL). 2018. PMID: 30020613 (Last Update: 25 October 2022).

22 Świerczyńska M, Mirowska-Guzel DM, Pindelska E. *Antiviral Drugs in Influenza*. International journal of environmental research and public health. 2022, 19 (5). doi: 10.3390/ijerph19053018.

23 European Medicines Agency. *Xofluza: baloxavir marboxil*. https://www.ema.europa.eu/en/medicines/human/EPAR/xofluza (accessed June 11th 2023).

24 Leland DS and Ginocchio CC. *Role of cell culture for virus detection in the age of technology*. Clinical microbiology reviews. 2007, 20 (1), 49–78. doi: 10.1128/cmr.00002-06.

25 Johnston SL and Siegel CS. *A comparison of direct immunofluorescence, shell vial culture, and conventional cell culture for the rapid detection of influenza A and B*. Diagnostic microbiology and infectious disease. 1991, 14 (2), 131–134. doi: 10.1016/0732-8893(91)90047-J.

26 Kemeny DM. *ELISA: Anwendung des Enzyme Linked Immunosorbent Assay im biologisch/ medizinischen Labor*, Gustav Fischer Verlag, Stuttgart. 1994. ISBN: 3-437-11493-X, p 24ff.

27 Leirs K, Tewari Kumar P, Decrop D, Pérez-Ruiz E, Leblebici P, van Kelst B, Compernolle G, Meeuws H, van Wesenbeeck L, Lagatie O, Stuyver L, Gils A, Lammertyn J, Spasic D. *Bioassay Development for Ultrasensitive Detection of Influenza A Nucleoprotein Using Digital ELISA*. Analytical chemistry. 2016, 88 (17), 8450–8458. doi: 10.1021/acs.analchem.6b00502.

28 Boer GF de, Back W, Osterhaus AD. *An ELISA for detection of antibodies against influenza A nucleoprotein in humans and various animal species*. Archives of Virology. 1990, 115 (1-2), 47–61. doi: 10.1007/BF01310622.

29 Rajendran M, Nachbagauer R, Ermler ME, Bunduc P, Amanat F, Izikson R, Cox M, Palese P, Eichelberger M, Krammer F. *Analysis of Anti-Influenza Virus Neuraminidase Antibodies in Children, Adults, and the Elderly by ELISA and Enzyme Inhibition: Evidence for Original Antigenic Sin*. mBio. 2017, 8 (2). doi: 10.1128/mbio.02281-16.

30 Courtney SJ, Stromberg ZR, Kubicek-Sutherland JZ. *Nucleic Acid-Based Sensing Techniques for Diagnostics and Surveillance of Influenza*. Biosensors. 2021, 11 (2). doi: 10.3390/bios11020047.

31 Rogers KR. *Principles of affinity-based biosensors*. Molecular biotechnology. 2000, 14 (2), 109–129. doi: 10.1385/MB:14:2:109.

32 Jarocka U, Sawicka R, Góra-Sochacka A, Sirko A, Zagórski-Ostoja W, Radecki J, Radecka H. *Electrochemical immunosensor for detection of antibodies against influenza A virus H5N1 in hen serum*. Biosensors & bioelectronics. 2014, 55, 301–306. doi: 10.1016/j.bios.2013.12.030.

33 Horiguchi Y, Goda T, Matsumoto A, Takeuchi H, Yamaoka S, Miyahara Y. *Direct and label-free influenza virus detection based on multisite binding to sialic acid receptors*. Biosensors & bioelectronics. 2017, 92, 234–240. doi: 10.1016/j.bios.2017.02.023.

34 Cheng C, Cui H, Wu J, Eda S. *A PCR-free point-of-care capacitive immunoassay for influenza A virus*. Microchim Acta. 2017, 184 (6), 1649–1657. doi: 10.1007/s00604-017-2140-4.

35 Oh J, Hart R, Capurro J, Noh HM. *Comprehensive analysis of particle motion under non-uniform AC electric fields in a microchannel*. Lab on a chip. 2009, 9 (1), 62–78. doi: 10.1039/B801594E.

36 Kaltenbach P and Meldau H. *Physik und Funktechnik für Seefahrer*, Fried.Vieweg & Sohn, Braunschweig. 1936. ISBN: 978-3864440687, p 46-48.

37 Theodore L. *Nanotechnology: Basic Calculations for Engineers and Scientists*, Wiley & Sons, Hoboken. 2006. ISBN: 978-0-471-75199-1, p 171-173.

38 Brown R. *XXVII. A brief account of microscopical observations made in the months of June, July and August 1827, on the particles contained in the pollen of plants; and on the general existence of active molecules in organic and inorganic bodies*. The Philosophical Magazine. 1828, 4 (21), 161–173. doi: 10.1080/14786442808674769.

39 Pohl HA. *The motion and precipitation of suspensoids in divergent electric fields*. Journal of Applied Physics. 1951, 22 (7), 869–871. doi: 10.1063/1.1700065.

40 Pohl HA and Hawk I. *Separation of living and dead cells by dielectrophoresis*. Science. 1966, 152 (3722), 647–649. doi: 10.1126/science.152.3722.647-a.

41 Morgan H and Green NG. *AC electrokinetics: Colloids and nanoparticles*, Research Studies Press, Baldock. 2003. ISBN: 0-86380-255-9.

42 Hughes MP. *Nanoelectromechanics in Engineering and Biology*, CRC Press, Boca Raton. 2003. ISBN: 0-8493-1183-7.

43 Pethig R. *Dielectric and Electronic Properties of Biological Materials*, John Wiley & Sons, Chichester. 1979. ISBN: 0-471-99728-5.

44 Pohl AH. *Dielectrophoresis: The behavior of neutral matter in nonuniform electric fields*, Cambridge University Press, Cambridge. 1978. ISBN: 0-521-21657-5, p 6-10.

45 Ramos A, Morgan H, Green NG, Castellanos A. *Ac electrokinetics: a review of forces in microelectrode structures*. Journal of Physics D: Applied Physics. 1998, 31 (18), 2338–2353. doi: 10.1088/0022-3727/31/18/021.

46 Green NG, Ramos A, Morgan H. *Ac electrokinetics: a survey of sub-micrometre particle dynamics*. Journal of Physics D: Applied Physics. 2000, 33 (6), 632–641. doi: 10.1088/0022-3727/33/6/308.

47 Stern O. *Zur Theorie der elektrolytischen Doppelschicht*. Zeitschrift für Elektrochemie. 1924, 1924 (30), 508–516. doi: 10.1002/bbpc.192400182.

48 Schwan HP. *Linear and nonlinear electrode polarization and biological materials*. Annals of biomedical engineering. 1992, 20 (3), 269–288. doi: 10.1007/BF02368531.

49 Ishai PB, Talary MS, Caduff A, Levy E, Feldman Y. *Electrode polarization in dielectric measurements: a review*. Meas. Sci. Technol. 2013, 24 (10), 102001. doi: 10.1088/0957-0233/24/10/102001.

50 Green NG, Ramos A, Gonzalez A, Morgan H, Castellanos A. *Fluid flow induced by nonuniform ac electric fields in electrolytes on microelectrodes. I. Experimental measurements*. Physical review. E, Statistical physics, plasmas, fluids, and related interdisciplinary topics. 2000, 61 (4 Pt B), 4011–4018. doi: 10.1103/physreve.61.4011.

51 Green NG, Ramos A, González A, Morgan H, Castellanos A. *Fluid flow induced by nonuniform ac electric fields in electrolytes on microelectrodes. III. Observation of streamlines and numerical simulation*. Physical review. E, Statistical, nonlinear, and soft matter physics. 2002, 66 (2), 026305-1 to 026305-11. doi: 10.1103/PhysRevE.66.026305.

52 Stanke S, Bier FF, Hölzel R. *Fluid streaming above interdigitated electrodes in dielectrophoresis experiments*. ELECTROPHORESIS. 2011, 32 (18), 2448–2455. doi: 10.1002/elps.201100096.

53 Garcia-Sanchez P, Ramos A, Green NG, Morgan H. *Experiments on AC electrokinetic pumping of liquids using arrays of microelectrodes*. IEEE Trans. Dielect. Electr. Insul. 2006, 13 (3), 670–677. doi: 10.1109/TDEI.2006.1657983.

54 Hoettges KF, McDonnell MB, Hughes MP. *Use of combined dielectrophoretic/electrohydrodynamic forces for biosensor enhancement*. Journal of Physics D: Applied Physics. 2003, 36 (20), L101-L104. doi: 10.1088/0022-3727/36/20/L01.

55 Wong PK, Chen C-Y, Wang T-H, Ho C-M. *An AC electroosmotic processor for biomolecules*, in *TRANSDUCERS '03. 12th International Conference on Solid-State Sensors, Actuators and Microsystems. Digest of Technical Papers (Cat. No.03TH8664)*. IEEE International Solid-State Sensors and Actuators Conference, 8-12 June 2003, Boston, MA, USA. IEEE. 2003. doi: 10.1109/SENSOR.2003.1215243, pp. 20–23.

56 Yuan Q, Yang K, Wu J. *Optimization of planar interdigitated microelectrode array for biofluid transport by AC electrothermal effect*. Microfluidics and Nanofluidics. 2014, 16 (1-2), 167–178. doi: 10.1007/s10404-013-1231-8.

57 Castellanos A, Ramos A, González A, Green NG, Morgan H. *Electrohydrodynamics and dielectrophoresis in microsystems: scaling laws*. Journal of Physics D: Applied Physics. 2003, 36 (20), 2584–2597. doi: 10.1088/0022-3727/36/20/023.

58 Wu J, Lian M, Yang K. *Micropumping of biofluids by alternating current electrothermal effects*. Appl. Phys. Lett. 2007, 90 (23), 234103. doi: 10.1063/1.2746413.

59 Feldman HC, Sigurdson M, Meinhart CD. *AC electrothermal enhancement of heterogeneous assays in microfluidics*. Lab on a chip. 2007, 7 (11), 1553–1559. doi: 10.1039/b706745c.

60 Gao J, Riahi R, Sin MLY, Zhang S, Wong PK. *Electrokinetic focusing and separation of mammalian cells in conductive biological fluids*. The Analyst. 2012, 137 (22), 5215–5221. doi: 10.1039/c2an35707k.

61 Mahabadi S, Labeed FH, Hughes MP. *Dielectrophoretic analysis of treated cancer cells for rapid assessment of treatment efficacy*. ELECTROPHORESIS. 2018, 39 (8), 1104–1110. doi: 10.1002/elps.201700488.

62 Mansoorifar A, Koklu A, Ma S, Raj GV, Beskok A. *Electrical Impedance Measurements of Biological Cells in Response to External Stimuli*. Analytical chemistry. 2018, 90 (7), 4320–4327. doi: 10.1021/acs.analchem.7b05392.

63 Moon H-S, Kwon K, Kim S-I, Han H, Sohn J, Lee S, Jung H-I. *Continuous separation of breast cancer cells from blood samples using multi-orifice flow fractionation (MOFF) and dielectrophoresis (DEP)*. Lab on a chip. 2011, 11 (6), 1118–1125. doi: 10.1039/c0lc00345j.

64 Song H, Rosano JM, Wang Y, Garson CJ, Prabhakarpandian B, Pant K, Klarmann GJ, Perantoni A, Alvarez LM, Lai E. *Continuous-flow sorting of stem cells and differentiation products based on dielectrophoresis*. Lab on a chip. 2015, 15 (5), 1320–1328. doi: 10.1039/c4lc01253d.

65 Hamada R, Suehiro J, Nakano M, Kikutani T, Konishi K. *Development of rapid oral bacteria detection apparatus based on dielectrophoretic impedance measurement method*. IET nanobiotechnology. 2011, 5 (2), 25–31. doi: 10.1049/iet-nbt.2010.0011.

66 Hoettges KF, Henslee EA, Serrano RMT, Jabr RI, Abdallat RG, Beale AD, Waheed A, Camelliti P, Fry CH, Daan R van der Veen., Labeed FH, Hughes MP. *Ten-Second*

Electrophysiology: Evaluation of the 3DEP Platform for high-speed, high-accuracy cell analysis. Scientific reports. 2019, 9 (19153), 1–13. doi: 10.1038/s41598-019-55579-9.

67 Gupta V, Jafferji I, Garza M, Melnikova VO, Hasegawa DK, Pethig R, Davis DW. *ApoStream, a new dielectrophoretic device for antibody independent isolation and recovery of viable cancer cells from blood*. Biomicrofluidics. 2012, 6 (2), 024133-1 to 024133-14. doi: 10.1063/1.4731647.

68 Di Trapani M, Manaresi N, Medoro G. *DEPArray system: An automatic image-based sorter for isolation of pure circulating tumor cells*. Cytometry. Part A : the journal of the International Society for Analytical Cytology. 2018, 93 (12), 1260–1266. doi: 10.1002/cyto.a.23687.

69 Washizu M, Suzuki S, Kurosawa O, Nishizaka T, Shinohara T. *Molecular dielectrophoresis of biopolymers*. IEEE Transactions on Industry Applications. 1994, 30 (4), 835–843. doi: 10.1109/28.297897.

70 Hölzel R, Calander N, Chiragwandi Z, Willander M, Bier FF. *Trapping single molecules by dielectrophoresis*. Physical review letters. 2005, 95 (12), 128102-1 to 128102-4. doi: 10.1103/PhysRevLett.95.128102.

71 Prüfer M, Stanke S, Bier FF, Hölzel R. *Catalytic activity of glucose oxidase after dielectrophoretic immobilization on nanoelectrodes*. ELECTROPHORESIS. 2023. doi: 10.1002/elps.202300010.

72 Hölzel R and Bier FF. *Dielectrophoretic manipulation of DNA*. IEE proceedings. Nanobiotechnology. 2003, 150 (2), 47–53. doi: 10.1049/ip-nbt:20031006.

73 Hyun C, Kaur H, McNabb DS, Li J. *Dielectrophoretic stretching of DNA tethered to a fiber tip*. Nanotechnology. 2015, 26 (12), 125501. doi: 10.1088/0957-4484/26/12/125501.

74 Manouchehri S, Ibsen S, Wright J, Rassenti L, Ghia EM, Widhopf GF, Kipps TJ, Heller MJ. *Dielectrophoretic recovery of DNA from plasma for the identification of chronic lymphocytic leukemia point mutations*. International journal of hematologic oncology. 2016, 5 (1), 27–35. doi: 10.2217/ijh-2015-0009.

75 Laux E-M, Wenger C, Bier FF, Hölzel R. *AC electrokinetic immobilization of organic dye molecules*. Analytical and bioanalytical chemistry. 2020, 412 (16), 3859–3870. doi: 10.1007/s00216-020-02480-4.

76 Luo J, Abdallah BG, Wolken GG, Arriaga EA, Ros A. *Insulator-based dielectrophoresis of mitochondria*. Biomicrofluidics. 2014, 8 (2), 021801-1 to 021801-11. doi: 10.1063/1.4866852.

77 Moschallski M, Hausmann M, Posch A, Paulus A, Kunz N, Duong TT, Angres B, Fuchsberger K, Steuer H, Stoll D, Werner S, Hagmeyer B, Stelzle M. *MicroPrep: chip-based dielectrophoretic purification of mitochondria*. ELECTROPHORESIS. 2010, 31 (15), 2655–2663. doi: 10.1002/elps.201000097.

78 Ting IP, Jolley K, Beasley CA, Pohl HA. *Dielectrophoresis of chloroplasts*. Biochimica et Biophysica Acta (BBA) - Bioenergetics. 1971, 234 (3), 324–329. doi: 10.1016/0005-2728(71)90198-8.

79 Ibsen S, Sonnenberg A, Schutt C, Mukthavaram R, Yeh Y, Ortac I, Manouchehri S, Kesari S, Esener S, Heller MJ. *Recovery of Drug Delivery Nanoparticles from Human Plasma Using an Electrokinetic Platform Technology*. Small (Weinheim an der Bergstrasse, Germany). 2015, 11 (38), 5088–5096. doi: 10.1002/smll.201500892.

80 Serafetinides AA, Makropoulou M, Spyratou E. *Optical tweezers and cell biomechanics in macro- and nano-scale*. Seventeenth International School on Quantum Electronics: Laser, 15th March, Nessebar, Bulgaria. SPIE. 2013. doi: 10.1117/12.2013349, p. 877014.

81 Gustafson KT, Huynh KT, Heineck D, Bueno J, Modestino A, Kim S, Gower A, Armstrong R, Schutt CE, Ibsen SD. *Automated fluorescence quantification of extracellular vesicles collected from blood plasma using dielectrophoresis*. Lab on a chip. 2021, 21 (7), 1318–1332. doi: 10.1039/d0lc00940g.

82 Ibsen SD, Wright J, Lewis JM, Kim S, Ko S-Y, Ong J, Manouchehri S, Vyas A, Akers J, Chen CC, Carter BS, Esener SC, Heller MJ. *Rapid Isolation and Detection of Exosomes and Associated Biomarkers from Plasma*. ACS nano. 2017, 11 (7), 6641–6651. doi: 10.1021/acsnano.7b00549.

83 Nakano M, Ding Z, Suehiro J. *Dielectrophoresis and dielectrophoretic impedance detection of adenovirus and rotavirus*. Japanese Journal of Applied Physics. 2016, 55 (1), 017001-1 to 017001-6. doi: 10.7567/JJAP.55.017001.

84 Ermolina I, Milner J, Morgan H. *Dielectrophoretic investigation of plant virus particles: Cow Pea Mosaic Virus and Tobacco Mosaic Virus*. ELECTROPHORESIS. 2006, 27 (20), 3939–3948. doi: 10.1002/elps.200500928.

85 Grom F, Kentsch J, Müller T, Schnelle T, Stelzle M. *Accumulation and trapping of hepatitis A virus particles by electrohydrodynamic flow and dielectrophoresis*. ELECTROPHORESIS. 2006, 27 (7), 1386–1393. doi: 10.1002/elps.200500416.

86 Hughes MP, Morgan H, Rixon FJ. *Measuring the dielectric properties of herpes simplex virus type 1 virions with dielectrophoresis*. Biochimica et Biophysica Acta (BBA) - General Subjects. 2002, 1571 (1), 1–8. doi: 10.1016/s0304-4165(02)00161-7.

87 Morgan H, Hughes MP, Green NG. *Separation of Submicron Bioparticles by Dielectrophoresis*. Biophysical Journal. 1999, 77 (1), 516–525. doi: 10.1016/S0006-3495(99)76908-0.

88 Hughes MP, Morgan H, Rixon FJ, Burt JPH, Pethig R. *Manipulation of herpes simplex virus type 1 by dielectrophoresis*. Biochimica et Biophysica Acta (BBA) - General Subjects. 1998, 1425 (1), 119–126. doi: 10.1016/S0304-4165(98)00058-0.

89 Gimsa J. *New light-scattering and field-trapping methods access the internal electric structure of submicron particles, like influenza viruses*. Annals of the New York Academy of Sciences. 1999, 873 (1), 287–298. doi: 10.1111/j.1749-6632.1999.tb09476.x.

90 Hübner Y, Hoettges KF, McDonnell MB, Carter MJ, Hughes MP. *Applications of dielectrophoretic/electro-hydrodynamic "zipper" electrodes for detection of biological nanoparticles*. International Journal of Nanomedicine. 2007, 2 (3), p 427–431.

91 Maruyama H, Kotani K, Masuda T, Honda A, Takahata T, Arai F. *Nanomanipulation of single influenza virus using dielectrophoretic concentration and optical tweezers for single virus infection to a specific cell on a microfluidic chip*. Microfluidics and Nanofluidics. 2011, 10 (5), 1109–1117. doi: 10.1007/s10404-010-0739-4.

92 Masuda T, Maruyama H, Honda A, Arai F. *Virus enrichment for single virus infection by using 3D insulator based dielectrophoresis*. PLoS ONE. 2014, 9 (6), 1-9. doi: 10.1371/journal.pone.0094083.

93 Nakano M, Obara R, Ding Z, Suehiro J. *Detection of norovirus and rotavirus by dielectrophoretic impedance measurement*. 2013 Seventh International Conference on Sensing Technology, 3-5th Dec, Wellington, New Zealand. IEEE. 2013. doi: 10.1109/ICSensT.2013.6727678, p 374–378.

94 Müller T, Fiedler S, Schnelle T, Ludwig K, Jung H, Fuhr G. *High frequency electric fields for trapping of viruses*. Biotechnology Techniques. 1996, 10 (4), 221–226. doi: 10.1007/BF00184018.

95 Schnelle T, Müller T, Fiedler S, Shirley SG, Ludwig K, Herrmann A, Fuhr G, Wagner B, Zimmermann U. *Trapping of viruses in high-frequency electric field cages*. Die Naturwissenschaften. 1996, 83 (4), 172–176. doi: 10.1007/BF01143058.

96 Ding J, Lawrence RM, Jones PV, Hogue BG, Hayes MA. *Concentration of Sindbis virus with optimized gradient insulator-based dielectrophoresis*. The Analyst. 2016, 141 (6), 1997–2008. doi: 10.1039/c5an02430g.

97 Morgan H and Green NG. *Dielectrophoretic manipulation of rod-shaped viral particles*. Journal of Electrostatics. 1997, 42 (3), 279–293. doi: 10.1016/S0304-3886(97)00159-9.

98 Green NG, Morgan H, Milner JJ. *Manipulation and trapping of sub-micron bioparticles using dielectrophoresis*. Journal of Biochemical and Biophysical Methods. 1997, 35 (2), 89–102. doi: 10.1016/s0165-022x(97)00033-x.

99 Chuang C-H, Du Y-C, Wu T-F, Chen C-H, Lee D-H, Chen S-M, Huang T-C, Wu H-P, Shaikh MO. *Immunosensor for the ultrasensitive and quantitative detection of bladder cancer in point of care testing*. Biosensors & bioelectronics. 2016, 84, 126–132. doi: 10.1016/j.bios.2015.12.103.

100 Iswardy E, Tsai T-C, Cheng I-F, Ho T-C, Perng GC, Chang H-C. *A bead-based immunofluorescence-assay on a microfluidic dielectrophoresis platform for rapid dengue virus detection*. Biosensors & bioelectronics. 2017, 95, 174–180. doi: 10.1016/j.bios.2017.04.011.

101 Sharma A, Han C-H, Jang J. *Rapid electrical immunoassay of the cardiac biomarker troponin I through dielectrophoretic concentration using imbedded electrodes*. Biosensors & bioelectronics. 2016, 82, 78–84. doi: 10.1016/j.bios.2016.03.056.

102 Singh R, Sharma A, Hong S, Jang J. *Electrical immunosensor based on dielectrophoretically-deposited carbon nanotubes for detection of influenza virus H1N1*. The Analyst. 2014, 139 (21), 5415–5421. doi: 10.1039/c4an01335b.

103 Zeng J, Duarte PA, Ma Y, Savchenko O, Shoute L, Khaniani Y, Babiuk S, Zhuo R, Abdelrasoul GN, Charlton C, Kanji JN, Babiuk L, Edward C, Chen J. *An impedimetric biosensor for COVID-19 serology test and modification of sensor performance via dielectrophoresis force*. Biosensors & bioelectronics. 2022, 213, 114476. doi: 10.1016/j.bios.2022.114476.

104 Li S, Ren Y, Cui H, Yuan Q, Wu J, Eda S, Jiang H. *Alternating current electrokinetics enhanced in situ capacitive immunoassay*. ELECTROPHORESIS. 2015, 36 (3), 471–474. doi: 10.1002/elps.201400284.

105 Han C-H, Woo SY, Bhardwaj J, Sharma A, Jang J. *Rapid and selective concentration of bacteria, viruses, and proteins using alternating current signal superimposition on two coplanar electrodes*. Scientific reports. 2018, 8 (1), 14942. doi: 10.1038/s41598-018-33329-7.

106 Otto S, Kaletta U, Bier FF, Wenger C, Hölzel R. *Dielectrophoretic immobilisation of antibodies on microelectrode arrays*. Lab on a chip. 2014, 14 (5), 998–1004. doi: 10.1039/c3lc51190a.

107 Yamamoto T and Fujii T. *Active immobilization of biomolecules on a hybrid three-dimensional nanoelectrode by dielectrophoresis for single-biomolecule study*. Nanotechnology. 2007, 18 (49), 495503 1-7. doi: 10.1088/0957-4484/18/49/495503.

108 Prüfer M, Wenger C, Bier FF, Laux E-M, Hölzel R. *Activity of AC electrokinetically immobilized horseradish peroxidase*. ELECTROPHORESIS. 2022, 43 (18-19), 1920–1933. doi: 10.1002/elps.202200073.

109 Laux E-M, Knigge X, Bier FF, Wenger C, Hölzel R. *Dielectrophoretic immobilization of proteins: Quantification by atomic force microscopy*. ELECTROPHORESIS. 2015, 36 (17), 2094–2101. doi: 10.1002/elps.201500108.

110 Knigge X, Wenger C, Bier FF, Hölzel R. *Dielectrophoretic immobilisation of nanoparticles as isolated singles in regular arrays*. Journal of Physics D: Applied Physics. 2018, 51 (65308), 1–11. doi: 10.1088/1361-6463/aaa528.

111 Laux E-M, Kaletta UC, Bier FF, Wenger C, Hölzel R. *Functionality of dielectrophoretically immobilized enzyme molecules*. ELECTROPHORESIS. 2014, 35 (4), 459–466. doi: 10.1002/elps.201300447.

112 Guido I, Jaeger MS, Duschl C. *Dielectrophoretic stretching of cells allows for characterization of their mechanical properties*. European biophysics journal : EBJ. 2011, 40 (3), 281–288. doi: 10.1007/s00249-010-0646-3.

113 Ghisellini P, Caiazzo M, Alessandrini A, Eggenhöffner R, Vassalli M, Facci P. *Direct electrical control of IgG conformation and functional activity at surfaces*. Scientific reports. 2016, 6, 37779. doi: 10.1038/srep37779.

114 Della Valle E, Marracino P, Pakhomova O, Liberti M, Apollonio F. *Nanosecond pulsed electric signals can affect electrostatic environment of proteins below the threshold of conformational effects: The case study of SOD1 with a molecular simulation study*. PLoS ONE. 2019, 14 (8), e0221685. doi: 10.1371/journal.pone.0221685.

115 Zhao W and Yang R. *Experimental study on conformational changes of lysozyme in solution induced by pulsed electric field and thermal stresses*. The journal of physical chemistry. B. 2010, 114 (1), 503–510. doi: 10.1021/jp9081189.

116 Budi A, Legge FS, Treutlein H, Yarovsky I. *Electric field effects on insulin chain-B conformation*. The journal of physical chemistry. B. 2005, 109 (47), 22641–22648. doi: 10.1021/jp052742q.

117 Bekard I and Dunstan DE. *Electric field induced changes in protein conformation*. Soft matter. 2014, 10 (3), 431–437. doi: 10.1039/c3sm52653d.

118 Laux E-M. *Electric field-assisted immobilization and alignment of biomolecules*. Universität Potsdam. Dissertation. 2016, urn:nbn:de:kobv:517-opus4-90271, 120 pp.

119 Lee KH, Youn JW, Kim HJ, Seong BL. *Identification and characterization of mutations in the high growth vaccine strain of influenza virus*. Archives of Virology. 2001, 146 (2), 369–377. doi: 10.1007/s007050170181.

120 Baez M, Palese P, Kilbourne ED. *Gene composition of high-yielding influenza vaccine strains obtained by recombination*. Journal of Infectious Diseases. 1980, 141 (3), 362–365. doi: 10.1093/infdis/141.3.362.

121 Roberts JJ and Warwick GP. *The reaction of β-propiolactone with guanosine, deoxyguanylic acid and RNA*. Biochemical Pharmacology. 1963, 12 (12), 1441–1442. doi: 10.1016/0006-2952(63)90216-8.

122 Yu S, Wei Y, Liang H, Ji W, Chang Z, Xie S, Wang Y, Li W, Liu Y, Wu H, Li J, Wang H, Yang X. *Comparison of Physical and Biochemical Characterizations of SARS-CoV-2 Inactivated by Different Treatments*. Viruses. 2022, 14 (9), 1–13. doi: 10.3390/v14091938.

123 LoGrippo GA. *Investigation of the use of beta-propiolactone in virus inactivation*. Annals of the New York Academy of Sciences. 1960, 83 (4), 578–594. doi: 10.1111/j.1749-6632.1960.tb40931.x.

124 She YM, Cheng K, Farnsworth A, Li X, Cyr TD. *Surface modifications of influenza proteins upon virus inactivation by β-propiolactone*. Proteomics. 2013, 13 (23-24), 3537–3547. doi: 10.1002/pmic.201300096.

125 Bonnafous P, Nicolaï MC, Taveau JC, Chevalier M, Barrière F, Medina J, Le Bihan O, Adam O, Ronzon F, Lambert O. *Treatment of influenza virus with Beta-propiolactone alters viral membrane fusion*. Biochimica et Biophysica Acta - Biomembranes. 2014, 1838 (1B), 355–363. doi: 10.1016/j.bbamem.2013.09.021.

126 UniProtKB. *Polymerase acidic protein - Influenza A virus (strain A/X-31 H3N2)*. https://www.uniprot.org/uniprotkb/Q9IQ47/entry (accessed February 8th 2023).

127 UniProtKB. *Polymerase basic protein 2 - Influenza A virus (strain A/X-31 H3N2)*. https://www.uniprot.org/uniprotkb/Q9IQ45/entry (accessed February 8th 2023).

128 UniProtKB. *RNA-directed RNA polymerase catalytic subunit - Influenza A virus (strain A/X-31 H3N2)*. https://www.uniprot.org/uniprotkb/Q9IQ46/entry (accessed February 8th 2023).

129 Shaw ML, Stone KL, Colangelo CM, Gulcicek EE, Palese P. *Cellular proteins in influenza virus particles*. PLoS Pathogens. 2008, 4 (6), 1–13. doi: 10.1371/journal.ppat.1000085.

130 UniProtKB. *Hemagglutinin - Influenza A virus (strain A/X-31 H3N2)*. https://www.uniprot.org/uniprotkb/P03438/entry (accessed February 8th 2023).

131 Wu CY, Yeh YC, Yang YC, Chou C, Liu MT, Wu HS, Chan JT, Hsiao PW. *Mammalian expression of virus-like particles for advanced mimicry of authentic influenza virus*. PLoS ONE. 2010, 5 (3), 1–17. doi: 10.1371/journal.pone.0009784.

132 Böttcher C, Ludwig K, Herrmann A, van Heel M, Stark H. *Structure of influenza haemagglutinin at neutral and at fusogenic pH by electron cryo-microscopy*. FEBS Letters. 1999, 463 (3), 255–259. doi: 10.1016/S0014-5793(99)01475-1.

133 Skehel JJ and Waterfield MD. *Studies on the primary structure of the influenza virus hemagglutinin*. Proceedings of the National Academy of Sciences of the United States of America. 1975, 72 (1), 93–97. doi: 10.1073/pnas.72.1.93.

134 Zhirnov OP, Ikizler MR, Wright PF. *Cleavage of Influenza A Virus Hemagglutinin in Human Respiratory Epithelium Is Cell Associated and Sensitive to Exogenous Antiproteases*. Journal of Virology. 2002, 76 (17), 8682–8689. doi: 10.1128/jvi.76.17.8682-8689.2002.

135 UniProtKB. *Nucleoprotein - Influenza A virus (strain A/X-31 H3N2)*. https://www.uniprot.org/uniprotkb/Q0PDM5/entry (accessed February 8th 2023).

136 UniProtKB. *Neuraminidase - Influenza A virus (strain A/X-31 H3N2)*. https://www.uniprot.org/uniprotkb/Q0PDM4/entry (accessed February 8th 2023).

137 Ward CW and Dopheide TAA. *Size and chemical composition of influenza virus hemagglutinin chains*. FEBS Letters. 1976, 65 (3), 365–368. doi: 10.1016/0014-5793(76)80148-2.

138 UniProtKB. *Matrix protein 1 - Influenza A virus (strain A/X-31 H3N2)*. https://www.uniprot.org/uniprotkb/Q9IQ48/entry (accessed February 8th 2023).

139 Shtykova EV, Baratova LA, Fedorova NV, Radyukhin VA, Ksenofontov AL, Volkov VV, Shishkov AV, Dolgov AA, Shilova LA, Batishchev OV, Jeffries CM, Svergun DI. *Structural*

analysis of influenza a virus matrix protein M1 and Its self-assemblies at low pH. PLoS ONE. 2013, 8 (12), 1–10. doi: 10.1371/journal.pone.0082431.

140 UniProtKB. *Matrix protein 2 - Influenza A virus (strain A/X-31 H3N2)*. https://www.uniprot.org/uniprotkb/Q9IQ49/entry (accessed February 8th 2023).

141 Pinto LH, Holsinger LJ, Lamb RA. *Influenza virus M2 protein has ion channel activity*. Cell. 1992, 69 (3), 517–528. doi: 10.1016/0092-8674(92)90452-I.

142 Holsinger LJ, Nichani D, Pinto LH, Lamb RA. *Influenza A virus M2 ion channel protein: a structure-function analysis*. Journal of Virology. 1994, 68 (3), 1551–1563. doi: 10.1128/jvi.68.3.1551-1563.1994.

143 Noda T. *Native morphology of influenza virions*. Frontiers in Microbiology. 2012, 2 (269), 1–5. doi: 10.3389/fmicb.2011.00269.

144 Knigge X. *Einzelmolekül-Manipulation mittels Nano-Elektroden und Dielektrophorese*. Universität Potsdam. Dissertation. 2020. doi: 10.25932/PUBLISHUP-44313, 151 pp.

145 Wang Y, Du F, Baune M, Thöming J. *Dielectrophoresis in aqueous suspension: impact of electrode configuration*. Microfluidics and Nanofluidics. 2014, 17 (3), 499–507. doi: 10.1007/s10404-013-1320-8.

146 Heida T, Wagenaar JBM, Rutten WLC, Marani E. *Investigating membrane breakdown of neuronal cells exposed to nonuniform electric fields by finite-element modeling and experiments*. IEEE transactions on bio-medical engineering. 2002, 49 (10), 1195–1203. doi: 10.1109/TBME.2002.803503.

147 Ramos A, Morgan H, Green NG, Castellanos A. *AC Electric-Field-Induced Fluid Flow in Microelectrodes*. Journal of colloid and interface science. 1999, 217 (2), 420–422. doi: 10.1006/jcis.1999.6346.

148 Green NG, Ramos A, González A, Castellanos A, Morgan H. *Electrothermally induced fluid flow on microelectrodes*. Journal of Electrostatics. 2001, 53 (2), 71–87. doi: 10.1016/S0304-3886(01)00132-2.

149 Chen DF and Du H. *Simulation studies on electrothermal fluid flow induced in a dielectrophoretic microelectrode system*. Journal of Micromechanics and Microengineering. 2006, 16 (11), 2411–2419. doi: 10.1088/0960-1317/16/11/023.

150 Green NG, Ramos A, González A, Castellanos A, Morgan H. *Electric field induced fluid flow on microelectrodes: the effect of illumination*. Journal of Physics D: Applied Physics. 2000, 33 (2), L13-L17. doi: 10.1088/0022-3727/33/2/102.

151 Stokes GG. *On the Effect of the Internal Friction of Fluids on the Motion of Pendulums*. Trans. Camb. Phil. Soc. 1851, 9, 8–106.

152 Yang H, Jiang H, Ramos A, García-Sánchez P. *AC electrokinetic pumping on symmetric electrode arrays*. Microfluidics and Nanofluidics. 2009, 7 (6), 767–772. doi: 10.1007/s10404-009-0434-5.

153 Ouyang M, Mohan R, Lu Y, Liu T, Mach KE, Sin MLY, McComb M, Joshi J, Gau V, Wong PK, Liao JC. *An AC electrokinetics facilitated biosensor cassette for rapid pathogen identification*. The Analyst. 2013, 138 (13), 3660–3666. doi: 10.1039/c3an00259d.

154 Draz MS, Uning K, Dupouy D, Gijs MAM. *Efficient AC electrothermal flow (ACET) on-chip for enhanced immunoassays*. Lab on a chip. 2023, 23 (6), 1637–1648. doi: 10.1039/d2lc01147f.

155 Williams SJ. *Enhanced electrothermal pumping with thin film resistive heaters*. ELECTROPHORESIS. 2013, 34 (9-10), 1400–1408. doi: 10.1002/elps.201200377.

156 Friedrich A, Habl G, Sauer M, Wolfrum J, Hoheisel J, Marmé N, Knemeyer J-P. *New hairpin-structured DNA probes: alternatives to classical molecular beacons*. Proc. of SPIE. 2007. doi: 10.1117/12.700346, 64440M.

157 Marmé N, Friedrich A, Denapaite D, Hakenbeck R, Knemeyer J-P. *Single nucleotide polymorphism analysis using different colored dye dimer probes*. Chemical Physics Letters. 2006, 428 (4-6), 440–445. doi: 10.1016/j.cplett.2006.07.064.

158 Hölzel R and Pethig R. *Protein Dielectrophoresis: I. Status of Experiments and an Empirical Theory*. Micromachines. 2020, 11 (5), 1–22. doi: 10.3390/mi11050533.

159 Hayes MA. *Dielectrophoresis of proteins: experimental data and evolving theory*. Analytical and bioanalytical chemistry. 2020, 412 (16), 3801–3811. doi: 10.1007/s00216-020-02623-7.

160 Sibarita J-B. *Deconvolution microscopy*. Advances in biochemical engineering/biotechnology. 2005, 95, 201–243. doi: 10.1007/b102215.

161 Aescht E, Büchl-Zimmermann S, Burmester A, Dänhardt-Pfeiffer S, Desel C, Hamers C, Jach G, Kässens M, Makovitzky J, Mulisch M, Nixdorf-Bergweiler B, Pütz D, Riedelsheimer B, van den Boom F, Wegerhoff R, Welsch U. *Romeis Mikroskopische Technik*, Spektrum Akademischer Verlag, Heidelberg. 2010. ISBN: 978-3-8274-1676-6, p 478.

162 Femino AM, Fay FS, Fogarty K, Singer RH. *Visualization of single RNA transcripts in situ*. Science. 1998, 280 (5363), 585–590. doi: 10.1126/science.280.5363.585.

163 Landmann L. *Deconvolution improves colocalization analysis of multiple fluorochromes in 3D confocal data sets more than filtering techniques*. Journal of microscopy. 2002, 208 (2), 134–147. doi: 10.1046/j.1365-2818.2002.01068.x.

164 Karpova TS, McNally JG, Moltz SL, Cooper JA. *Assembly and function of the actin cytoskeleton of yeast: relationships between cables and patches*. The Journal of cell biology. 1998, 142 (6), 1501–1517. doi: 10.1083/jcb.142.6.1501.

165 Sage D, Donati L, Soulez F, Fortun D, Schmit G, Seitz A, Guiet R, Vonesch C, Unser M. *DeconvolutionLab2: An open-source software for deconvolution microscopy*. Methods (San Diego, Calif.). 2017, 115, 28–41. doi: 10.1016/j.ymeth.2016.12.015.

166 Pribyl, M., Snita, D., Marek, M. *Multiphysical Modeling of DC and AC Electroosmosis in Micro- and Nanosystems*, IntechOpen, Rijeka. 2008. ISBN: 978-3-902613-25-7, p 501-507.

167 Bazant, M.Z. and Dongqing, L. *Encyclopedia of Microfluidics and Nanofluidics, Part I: AC Electro-osmotic flow*, Springer, Berlin, Heidelberg, New York. 2008. ISBN: 978-3-642-27758-0, p 8-14.

168 Leyton-Puig D, Kedziora KM, Isogai T, van den Broek B, Jalink K, Innocenti M. *PFA fixation enables artifact-free super-resolution imaging of the actin cytoskeleton and associated proteins*. Biology open. 2016, 5 (7), 1001–1009. doi: 10.1242/bio.019570.

169 Jacquemet G, Carisey AF, Hamidi H, Henriques R, Leterrier C. *The cell biologist's guide to super-resolution microscopy*. Journal of cell science. 2020, 133 (11). doi: 10.1242/jcs.240713.

170 Liu KN and Boxer SG. *Single-virus content-mixing assay reveals cholesterol-enhanced influenza membrane fusion efficiency*. Biophysical Journal. 2021, 120 (21), 4832–4841. doi: 10.1016/j.bpj.2021.09.023.

171 Delaveris CS, Webster ER, Banik SM, Boxer SG, Bertozzi CR. *Membrane-tethered mucin-like polypeptides sterically inhibit binding and slow fusion kinetics of influenza A virus*. Proceedings of the National Academy of Sciences of the United States of America. 2020, 117 (23), 12643–12650. doi: 10.1073/pnas.1921962117.

172 Rawle RJ, Webster ER, Jelen M, Kasson PM, Boxer SG. *pH Dependence of Zika Membrane Fusion Kinetics Reveals an Off-Pathway State*. ACS central science. 2018, 4 (11), 1503–1510. doi: 10.1021/acscentsci.8b00494.

173 Le Ru EC, Blackie E, Meyer M, Etchegoin PG. *Surface Enhanced Raman Scattering Enhancement Factors: A Comprehensive Study*. J. Phys. Chem. C. 2007, 111 (37), 13794–13803. doi: 10.1021/jp0687908.

174 Saviñon-Flores F, Méndez E, López-Castaños M, Carabarin-Lima A, López-Castaños KA, González-Fuentes MA, Méndez-Albores A. *A Review on SERS-Based Detection of Human Virus Infections: Influenza and Coronavirus*. Biosensors. 2021, 11 (3). doi: 10.3390/bios11030066.

175 Laux, E.-M., Docoslis, A., Wenger, C., Bier, F.F., Hölzel, R. *Combination of dielectrophoresis and SERS for bacteria detection and characterization*. 19th IUPAB Congress/11th EBSA Congress. 2017, 16-20 Jul, Edinburgh, Scotland. Springer, New York, USA, 46, S331. doi: 10.1007/s00249-017-1218-6.

176 Dies H, Raveendran J, Escobedo C, Docoslis A. *In situ assembly of active surface-enhanced Raman scattering substrates via electric field-guided growth of dendritic nanoparticle structures*. Nanoscale. 2017, 9 (23), 7847–7857. doi: 10.1039/c7nr01743j.

177 Hell SW. *Toward fluorescence nanoscopy*. Nature biotechnology. 2003, 21 (11), 1347–1355. doi: 10.1038/nbt895.

178 Hell SW and Kroug M. *Ground-state-depletion fluorscence microscopy: A concept for breaking the diffraction resolution limit*. Appl. Phys. B. 1995, 60 (5), 495–497. doi: 10.1007/BF01081333.

179 Wurm CA, Kolmakov K, Göttfert F, Ta H, Bossi M, Schill H, Berning S, Jakobs S, Donnert G, Belov VN, Hell SW. *Novel red fluorophores with superior performance in STED microscopy*. Opt Nanoscopy. 2012, 1 (1), 7. doi: 10.1186/2192-2853-1-7.

180 Costello DA, Lee DW, Drewes J, Vasquez KA, Kisler K, Wiesner U, Pollack L, Whittaker GR, Daniel S. *Influenza virus-membrane fusion triggered by proton uncaging for single particle studies of fusion kinetics*. Analytical chemistry. 2012, 84 (20), 8480–8489. doi: 10.1021/ac3006473.

181 Hoekstra D, Boer T de, Klappe K, Wilschut J. *Fluorescence method for measuring the kinetics of fusion between biological membranes*. Biochemistry. 1984, 23 (24), 5675–5681. doi: 10.1021/bi00319a002.

182 Peluso P, Wilson DS, Do D, Tran H, Venkatasubbaiah M, Quincy D, Heidecker B, Poindexter K, Tolani N, Phelan M, Witte K, Jung LS, Wagner P, Nock S. *Optimizing antibody immobilization strategies for the construction of protein microarrays*. Analytical biochemistry. 2003, 312 (2), 113–124. doi: 10.1016/S0003-2697(02)00442-6.

183 Chen S, Liu L, Zhou J, Jiang S. *Controlling Antibody Orientation on Charged Self-Assembled Monolayers*. Langmuir. 2003, 19 (7), 2859–2864. doi: 10.1021/la026498v.

184 Emaminejad S, Javanmard M, Gupta C, Chang S, Davis RW, Howe RT. *Tunable control of antibody immobilization using electric field*. Proceedings of the National Academy of Sciences of the United States of America. 2015, 112 (7), 1995–1999. doi: 10.1073/pnas.1424592112.

185 Kim HJ, Park D, Park Y, Kim D-H, Kim J. *Electric-Field-Mediated In-Sensor Alignment of Antibody's Orientation to Enhance the Antibody-Antigen Binding for Ultrahigh Sensitivity Sensors*. Nano letters. 2022, 22 (16), 6537–6544. doi: 10.1021/acs.nanolett.2c01584.

186 Cai D, Xiao M, Xu P, Xu Y-C, Du W. *An integrated microfluidic device utilizing dielectrophoresis and multiplex array PCR for point-of-care detection of pathogens*. Lab on a chip. 2014, 14 (20), 3917–3924. doi: 10.1039/C4LC00669K.

187 Suehiro J, Ohtsubo A, Hatano T, Hara M. *Selective detection of bacteria by a dielectrophoretic impedance measurement method using an antibody-immobilized electrode chip*. Sensors and Actuators B: Chemical. 2006, 119 (1), 319–326. doi: 10.1016/j.snb.2005.12.027.

188 Ettehad HM, Yadav RK, Guha S, Wenger C. *Towards CMOS Integrated Microfluidics Using Dielectrophoretic Immobilization*. Biosensors. 2019, 9 (2), 1–17. doi: 10.3390/bios9020077.

189 Guha S, Schmalz K, Wenger C, Herzel F. *Self-calibrating highly sensitive dynamic capacitance sensor: towards rapid sensing and counting of particles in laminar flow systems*. The Analyst. 2015, 140 (9), 3262–3272. doi: 10.1039/c5an00187k.

Appendix

A – Self-written macro for summation projection

```
if (isOpen("ROI Manager")) {
      selectWindow("ROI Manager");
      run("Close");

file = File.openDialog("Select the text file to read");
allText = File.openAsString(file);
text = split(allText, "\n");
hdr = split(text[0]);

iX = 0;
iY = 1;

d = getNumber("Durchmesser der Elektroden (Pixel): ", d);
w = getNumber("Breite der ROIs ", w);
h = getNumber("Hoehe der ROIs ", h);

for (i = 1; i < (text.length); i++){
    line = split(text[i]);
    makePoint(parseInt(line[iX]), parseInt(line[iY]));
    run("Specify...", "width=&w height=&h iX=&iX iY=&iY");
    roiManager("Add");
 }

Dialog.create("Move Selections");
dx = w/2-d/2;
dy = h/2-d/2;
Dialog.addNumber("X Displacement:", dx);
Dialog.addNumber("Y Displacement:", dy);
n = roiManager("count");
if (n==0)
      exit("The ROI Manager is empty");
    for (i=0; i<n; i++) {
          roiManager("select", i);
          getSelectionBounds(x, y, w, h);
          setSelectionLocation(x-dx, y-dy);
          roiManager("update")
}

dir = getDirectory("Speicherort der Bilderserie");

for (i=0; i<n; i++) {
          roiManager("select", i);
          run("Copy");
          run("Internal Clipboard");
          saveAs("Tiff", dir + i+1);
          close();
}
```

Acknowledgement

I would like to express my sincere gratitude to my first and second supervisors, Prof. Dr. Frank F. Bier from the University of Potsdam and PD Dr. Ralph Hölzel from the Fraunhofer IZI-BB, for their invaluable guidance, support, and encouragement throughout my doctorate journey. I am grateful for those plenty in-depth discussion we had about this project. Gathering of ideas was always a fruitful conversation. Your profound expertise, unwavering commitment, and constructive feedback were instrumental in shaping my research and helping me overcome the many challenges I faced, not only in terms of science. I've had the opportunity to work in a friendly and open environment, which I am aware is not a given.

I would like to extend my thanks to my whole group at Fraunhofer IZI-BB: PD Dr. Ralph Hölzel, Dr. Eva-Maria Laux, Dr. Xenia Knigge, Dr. Marlen Kruse and Mareike Prüfer, for creating a warm and friendly atmosphere, talking about science, books and movies and having a friendly ear for problems and worries. I am astound about the focused and in-depth discussions we have when talking about our research and gathering of ideas. I'm impressed how we keep pushing the limits of our instruments and, through our collaboration and the right questions, we work to break through those limits.

My sincere thanks go to Victor Kietzmann, a master's student whom I had the pleasure of supervising during his industrial internship and master's thesis. His intelligence, curiosity, and creativity have been a great asset to our team. Through our conversations, Victor has helped me to reflect on my research. We had many engaging discussions, not just about science, and I always appreciated his unique perspective and thoughtful questions. I really enjoyed working with you.

I want to thank PD Dr. Thorsten Wolff and Dr. Sandra Sänger from the Robert Koch-Institute in Berlin for kindly providing us with X-31 samples.

I am thankful for the cooperation with the IHP in Frankfurt/Oder and here especially with Prof. Dr. Christian Wenger. Your provision of electrode chips was critical to our research, and our collaboration and exchanges about the progress of the projects were insightful. I have learned a lot from our discussions, especially about microelectronics.

Special thanks go to Jörg Schenk and Dr. Frank Sellrie from Hybrotec GmbH for their invaluable help with ELISA and for patiently answering my many questions. Your guidance,

expertise, and support were important for the progress of my work. I am truly grateful for your time and effort and all you taught me about ELISA and antibodies.

Furthermore, I want to thank Kira Lenz and her supervisor Dr. Nenad Gajovic-Eichelmann for the X-31 preparations on their gold-coated glass substrate covered with an electropolymer, which have been great samples for my REM measurements.

I would like to extend my thanks to abberior instruments GmbH and especially Sandra Kostrowski for making it possible to work on a STED-microscope for some weeks. Thank you for your support and sharing you knowledge with us. Thanks to your guidance we found a way to measure our rather special samples and the images are impressive.

I would like to acknowledge the financial support provided by the *Studienstiftung des deutschen Volkes*. Without their generous funding, this research would not have been possible. Here, I would also like to thank Dr. Peter Antes and Prof. Dr. Carsten Beta for accompanying my work as my advisor (Referent) and liaison lecturer (Vertrauenzdozent).

I would like to thank all doctoral candidates I met helping me putting events into perspective. We know how challenging this journey is. Do not let anyone make you feel like you are not worthy. Try to see it from a positive point of view: It is a chance to learn! And we have learned a lot during our doctorate, and sometimes even about science.

Last but not least, I would like to express my sincere gratitude to my family and friends for their unwavering support throughout the duration of my thesis. Your encouragement, patience, and belief in me was a driving force. To Maxi Frederike Hempel, thank you for patiently listening every day to my wild and crazy stories. I am grateful for the hours of honest conversation we have every day. Thank you for helping me putting things into perspective. Thank you for helping me boost my self-esteem. Thank you for the amazing humor we have together. Your love and support gave me the strength to push through many challenges and to complete this important milestone.

Statutory declaration

I hereby certify that I have prepared this dissertation independently, using only the referred sources and support. Drawings and illustrations have been created by myself or are provided with its reference. Furthermore, I affirm that I have not submitted the present thesis to any other university.

Potsdam, 5 December 2023

_____

Sandra Stanke